University of California
Santa Barbara

The Design and Fabrication of Snap-Release Integrated Optomechanical Circuits

A dissertation submitted in partial satisfaction
of the requirements for the degree

Doctor of Philosophy
in
Physics

by

Eric Christopher Langman

Committee in charge:

Professor Dirk Bouwmeester, Chair
Professor David Weld
Professor Wim van Dam

September 2018

The Dissertation of Eric Christopher Langman is approved.

Professor David Weld

Professor Wim van Dam

Professor Dirk Bouwmeester, Committee Chair

February 2018

The Design and Fabrication of

Snap-Release Integrated Optomechanical Circuits

by

Eric Christopher Langman

This page intentionally left blank.

Acknowledgements

First and foremost, I want to enthusiastically thank Dirk Bouwmeester and Wolfgang Löffler for their continued support through the extended duration of this project. I also want to thank all of my labmates who were present throughout this process, especially my officemates Matt Weaver and John Frey for being there to bounce ideas off whenever needed. Additionally, I would like to thank the various members of the John Bowers group, particularly Jon Peters, Eric Stanton, Nicolas Volet, Lin Chang, and Sudharsanan Srinivasan, for their help at the start of this project.

With equal enthusiasm I want to thank all of the members of the UCSB Nanofabrication Facility ("The Cleanroom") who advised me along the way. From teaching me how to use the machines, to teaching me how to fix the machines, to explaining to me why I should be using a different machine, this project could and would not have been completed without your continued support. In particular I would like to acknowledge Bill Mitchell, Brian Thibeault, Don Freeborn, Tony Bosch, and Demis John, whom were in charge of the machines and processes that I dependent upon the most. Returning my texts at midnight on Saturdays is something I will never forget.

Finally, I would like to thank my parents and younger brother for being there to support me from well before the beginning of this project. Mathematically, for ever 1 year of this endeavor, you all have had to deal with me for 3 additional years. You have always been there to push me to explore the world in my own way, from learning base 5 arithmetic at the age of 9 for absolutely no reason, to starting original scientific research in high school. And you were always there to cushion me when that exploration ran awry. There is no substitution for the unconditional support you provided me.

This page intentionally left blank.

Curriculum Vitæ

Eric Christopher Langman

Education

2018	Ph.D. Physics, University of California, Santa Barbara
2014	M.A. Physics, University of California, Santa Barbara
2010	B.S. Physics, Harvey Mudd College

Publications

3. H. Snijders, J. A. Frey, J. Norman, M. P. Bakker, E. C. Langman, A. Gossard, J. E. Bowers, M. P. van Exter, D. Bouwmeester, and W. Lffler, *Purification of a single-photon nonlinearity, Nature Communications* **7** (aug, 2016) 12578.

2. J. Gao, M. R. Vissers, M. O. Sandberg, F. C. S. da Silva, S. W. Nam, D. P. Pappas, D. S. Wisbey, E. C. Langman, S. R. Meeker, B. A. Mazin, H. G. Leduc, J. Zmuidzinas, and K. D. Irwin, *A titanium-nitride near-infrared kinetic inductance photon-counting detector and its anomalous electrodynamics, Applied Physics Letters* **101** (oct, 2012) 142602.

1. B. A. Mazin, B. Bumble, S. R. Meeker, K. OBrien, S. McHugh, and E. Langman, *A superconducting focal plane array for ultraviolet, optical, and near-infrared astrophysics, Optics Express* **20** (jan, 2011) 1503, [arXiv:1112.0004].

This page intentionally left blank.

Abstract

The Design and Fabrication of

Snap-Release Integrated Optomechanical Circuits

by

Eric Christopher Langman

A fully-integrated optomechanical system is fabricated from a single layer of 400 nm thick stoichiometric LPCVD Si_3N_4. Optomechanical coupling is demonstrated between single-mode optical ring resonators and nanomechanical resonators released using our novel 'snap-release' mechanism. This mechanism utilizes the high tensile stress of LPCVD Si_3N_4 to realize sub-50 nm distances between optical ring resonators and the released 'snap-release' nanobeams (SRNBs). In this dissertation we present the design, fabrication, and characterization of this new optomechanical system.

This page intentionally left blank.

Contents

Curriculum Vitae **vii**

Abstract **ix**

List of Figures **xv**

List of Tables **xxi**

Introduction **1**

1 Cavity Optomechanics **7**
1.1 Theory of Cavity Optomechanics 10
1.1.1 Optical Finesse and fQ Product 11
1.1.2 Hamiltonian Formalism 12
1.1.2.1 Radiation Pressure Force 15
1.1.2.2 Linearized Optomechanical Hamiltonian 15
1.1.3 Sideband Generation 16
1.1.4 Sideband Cooling 18
1.1.5 Quantum Entanglement 21
1.2 Free-Space Optomechanical Systems 23
1.3 Integrated Optomechanics 25
1.3.1 Optical Ring Resonators 26
1.3.1.1 Input-Output Theory 27
1.3.1.2 Resonance and Loss 30
1.3.2 Adding an Optomechanical Interaction 33

2 Experimental Design and Simulation **37**
2.1 Photonic Simulations 41
2.1.1 Optical Mode Simulations 42
2.1.2 Waveguide Width 44
2.1.3 Bending Loss 45
2.1.4 Thickness of Thermal SiO_2 Base Layer 46

2.1.5 Full Ring Simulation (OMNISIM) 48
2.2 Mechanical Calculations and Simulations 51
2.2.1 Properties of Si_3N_4 Nanobeams with Tensile Stress 52
2.2.1.1 General Solution to Euler-Bernouli Equation 53
2.2.1.2 Low-Stress Solutions 55
2.2.1.3 High-Stress Solutions 57
2.2.1.4 Tensile Stress in LPCVD Si_3N_4 'Snap-Release' Nanobeams 64
2.2.1.5 Finite Element Method (FEM) Simulations in COMSOL 68
2.2.1.6 Effective Mass 72
2.2.1.7 Thermal Motion 74
2.2.2 Damping Mechanisms 76
2.2.2.1 Mechanical Damping 76
2.2.2.2 Air Damping 84
2.3 Optomechanical Coupling 87
2.3.1 Simulations 88
2.3.1.1 Mode Polarization 90
2.3.1.2 Nanobeam Width 91
2.3.1.3 Ring Radius 92
2.3.1.4 Ring Waveguide Width 93
2.3.2 Estimation of Frequency Shift 94

3 Characterization and Optimization of the Fabrication Process 97
3.1 Process Overview 100
3.2 Mask Design and Layout 107
3.3 Chromium Hard Mask and Vertical ICP Etching 111
3.3.1 High Resolution Deep Ultraviolet (DUV) Lithography 112
3.3.2 Ultra-High Resolution Electron Beam Lithography 114
3.3.3 Chromium Dry-Etching 114
3.3.3.1 Purge Gas Selection 114
3.3.3.2 Etch Loading Issues Induced by Carrier Wafer Interaction 115
3.3.3.3 Formation of Notches Along Edge of Chromium Mask . 116
3.3.3.4 Chromium ICP Etch with Cl_2/O_2 119
3.3.4 Vertical Etching of Si_3N_4 120
3.4 SiO_2 Cladding Deposition and Liftoff 122
3.5 Release of Mechanical Structures with Vapor HF Dry Etching 124
3.6 Dicing and Facet Polishing 126

4 Anodic Wafer Bonding 127
4.1 Bonding Chemistry and Procedure 128
4.2 Material Selection 132
4.3 Method of Deposition 134
4.4 Results 135

4.4.1 Aluminum . . . 136
4.4.2 Tantalum . . . 137
4.4.3 Tungsten . . . 140

5 Device Characterization and Preliminary Results 141
5.1 Optical Setup . . . 142
5.2 Ring Resonators . . . 144
5.2.1 Optical Quality Factors . . . 144
5.3 Snap-Release Nanobeams . . . 147
5.4 Detection of Optomechanical Coupling . . . 153
5.4.1 Atmospheric Measurements . . . 153
5.4.2 Vacuum Measurements . . . 156

Conclusion 161

A Organization of ThickRings_v2 Mask 163
A.1 Primary Devices: Columns A,B,C,D,E . . . 163
A.2 Extra Devices: Columns 6 . . . 165

Bibliography 167

This page intentionally left blank.

List of Figures

1.1 Fabry-Perot cavity with moveable mirror attached to a harmonic oscillator. 10
1.2 Optomechanical spectra demonstrating sideband characteristics. Each black line is the sum of a fundamental cavity resonance, along with the two sidebands. 17
1.3 SEM images of early generation 'mirror on a spring' designs for optomechanical systems. 23
1.4 Current trampoline resonators include added mass and extra stages of isolation to improve performance. 24
1.5 Mapping of amplitude and field definitions for characterizing properties of double-bused ring resonators. 27
1.6 Predicted internal quality factors of ring resonators as a function of propagation loss (db/cm). 32
1.7 Simulated predictions of optical finesse as a function of ring radius. . . . 32
1.8 Schematic of an integrated optomechanical system, coupling a nanobeam to an optical ring resonator both fabricated from the same layer of Si_3N_4. 33

2.1 Optical mode simulations obtained using FMM mode solver in FIMMWAVE. Each waveguide is 1200 nm wide, with varying height, and composed of Si_3N_4 surrounded by SiO_2 42
2.2 FIMMWAVE simulations of bent waveguides representative of optical ring resonators. A PML is necessary on the right side of the waveguide to avoid boundary reflections from the mode distortion to that side; they also allow for direct measurement of bending loss. 43
2.3 Effective index n_{eff} for Si_3N_4 waveguides of varying widths. Caculations are performed using the FFM mode solver, with PMLs placed on both sides of the simulation space. 44
2.4 Comparison of simulated bending loss for the modes of 400 nm × 800 nm Si_3N_4 waveguides, obtained using the FMM mode solver in FIMMWAVE 45
2.5 Simulated absorption loss for a 800 nm wide Si_3N_4 waveguide, as a function of thickness of the SiO_2 layer between the Si substrate and Si_3N_4. . . . 46

2.6 Simulation of a full ring resonator geometry in OMNISIM, near resonance. The amplitude of calculated H_y fields, shown here, are good for visually discerning ring absorption for TE modes. 48
2.7 Sample simulations obtained using OMNISIM, after an initial FDTD simulation of the geometry. 49
2.8 Results demonstrating the effect of changing the coupling split on both the optical $\mathcal{Q}$ and resonance frequency. The latter is due to a change in the phase of the coupler. All simulations were for a ring of radius 16 µm, with a width of 800 nm. Data is plotted below. 50
2.9 Plot of the simulated $\mathcal{Q}$ as a function of the separation between waveguide and ring resonator. The data matches the fit to an exponential very well, with the exception of the data point at 450 nm. 50
2.10 Comparison between fundamental mode shapes of low-stress nanobeams and nanostrings. 56
2.11 FEM simulations compared to the standard 1D nanostring approximation and the first-order corrected equations. 60
2.12 Comparison of mode shapes obtained for clamping regions using FEM simulations and analytic models. 61
2.13 Comparison between FEM simulations and the first-order corrected eigenmode given by Eq. 2.40. See Fig. 2.14 below for residual plot. 63
2.14 Residual Plot for Fig. 2.13. We see that the analytic equation agrees within 0.05% everywhere along the graph, maxmimally near the clamping region. The simulations appeared to produce a small, yet non-zero, slope at the clamping point. 63
2.15 Geometric breakdown of the release of a 'snap-release' nanobeam. 65
2.16 COMSOL simulations comparing the fundamental mode profiles of (a) zero-stress nanobeam to a (b) high-stress nanobeam. Dimensions for both are $w = 0.1\,\mu\text{m}$, $h = 0.4\,\mu\text{m}$, $L = 20\,\mu\text{m}$. In (c), the mode shapes are compared to the mode shape equations for low and high stress nanobeams. 68
2.17 Simulation setup and results of SR nanobeams using COMSOL. 69
2.18 SRNB Simulations for the fundamental mode ($j = 1$). 70
2.19 SRNB Simulations for the 2nd mode ($j = 2$). 71
2.20 SRNB Simulations for the 3rd mode ($j = 3$). 71
2.21 COMSOL evaluation of $u_1(x)$ and its derivatives. The derivatives are obtained using Mathematica's interpolation function. 79
2.22 Predicted pressure dependency on observed nanomechanical $\mathcal{Q}$-factors, for both analytic approximations and numerical estimates obtained using FEM simulations. 86
2.23 Geometry and sample results of simulations used to determine shift in effective index of optical modes 88

2.24 Change in effective index for varying optomechanical split. The integral of each curve represent N(x), and the change between those integrals as a function of optomechanical split is $\frac{\partial}{\partial x}N(x)$. 89
2.25 Calculated Integrated Index Shift curves of the TE and TM modes of a 800 nm wide single-mode optical ring resonator with a radius of 50 µm, optomechanically coupled to a nanobeam of width 100 nm. 90
2.26 Calculated Integrated Index Shift curves for the TE mode of a 800 nm wide single-mode optical ring resonator with a radius of 50 µm, optomechanically coupled to nanobeams of varying widths. 91
2.27 Calculated Integrated Index Shift curves for the TE modes of 800 nm wide single-mode optical ring resonators of varying radii, optomechanically coupled to a 100 nm wide nanobeam. 92
2.28 Calculated Integrated Index Shift curves between a 100 nm wide nanobeam and 50 µm radii optical ring resonators of varying widths. 93

3.1 Topological representation of our device design. Light is coupled into the input waveguide (lower left) from a lensed single-mode fiber. Resonant light is absorbed by the ring and exits from the drop port (upper left). This light is usually then collected by a multi-mode lensed fiber (not shown). 98
3.2 SEM image showing an individual optomechanical device from one of our samples. The ring resonator and 'snap-release' geometries are clearly visible. 99
3.3 Basic layers prior to lithography processes. 100
3.4 The 60 nm chromium layer is etched using multiple techniques to yield a final mask which that yields thin mechanical oscillators released in close proximity to optical ring resonators. 101
3.5 ICP etching of the Si_3N_4 layer using chromium as a hard mask leads to near vertical sidewalls. The chromium can be removed afterwards using dry or wet options. 102
3.6 SiO_2 cladding is deposited on the Si_3N_4 waveguides located outside of the device regions, using RF-sputtering combined with a lift-off process. This both protects them and reduces loss in these waveguide regions. 103
3.7 A lift-off process is used to deposit a wafer-bonding compatible layer around the outer edges of the samples. 104
3.8 Removal of SiO_2 beneath the mechanical structures yields tall bridge-like structures. The fundamental mode of oscillation for such structures is in the wafer-plane, to and away from the optical ring resonator. The waferbonding layers protect the SiO_2 cladding from the vapor HF process, preserving surface uniformity in those critical regions. 105
3.9 Final packaging processes of the sample. 106

3.10 Schematic of ASML mask *ThickRings_v2*, designed for fabrication of bridges released on the outside of our ring resonators. The device region, located in the center, consists of a 6 × 6 array of sets of 12 rings (each boxed in plum). Three global EBL alignment marks are on each side of the device region. Laser etch-depth monitoring pads can be found on each corner. Test regions, containing structures for etch and mechanical release characterization, can be found along both sides. 107
3.11 Layout and images of a single set of 12 rings. The device region of our ASML mask is made up of a 6×6 array of such sets. 108
3.12 SEM Images of significant aspects of the ASML mask. 110
3.13 Vertical Etch profiles of Cr etch process. 111
3.14 SEM Image of sidewall roughness following vertical etch of Si_3N_4 layer. . 112
3.15 Comparison of photoresist sidewall roughness, with and without a thermal reflow. 113
3.16 Notches along the outer edge of the chromium mask are correlated with sidewall roughness near the position of the notches. 116
3.17 SEM image of sidewalls obtained using our optimized chromium etch process. 118
3.18 SEM Image of sidewall roughness following vertical etch of Si_3N_4 layer. . 119
3.19 SEM images of the cladding deposition on 400 nm waveguides. Vapor HF is used to reveal the structure within the layers. 122
3.20 An octagon-shaped patch of photoresist shields the ring resonators during the SiO_2 sputtering process. 123
3.21 Layer thickness for 2 different height/tilt configurations on Sputter 3, for 3 hour deposition time. 123
3.22 Stiction can be avoided with a vapor HF etch instead of a standard wet release, making 'snap-release' nanobeams possible using the SiO_2 as a sacrificial layer. 124
3.23 Facet polishing is critical in reducing insertion loss when coupling light into and out of the optical waveguides. The images here are for non-wafer bonded samples, to be used with the vacuum setup described in Section 5.4.2. 126

4.1 **(Step 1)** The borosilicate glass is placed on top of the sample, then loaded into the vacuum bonder. 129
4.2 **(Step 2)** The system is pumped down to 2×10^{-6} mbar, and heated to 400 °C. At 400 °C, the Na_2O dissociates into Na^+ and O^{2-} ions. 129
4.3 **(Step 3)** A negative voltage is placed across the device. This drives the Na^+ ions to the cathode and the O^{2-} toward the conductive material that is shorted to the anode. 130
4.4 **(Step 4)** Covalent Si-O bonds form at the interface between the α-Si and the Borofloat glass. 130

4.5 **(Step 5)** The sample is allowed to cool and return to atomspheric conditions, to be diced and polished. As the seal is known to be strong and hermetic, the device regions do not return to atmospheric pressure. . . . 131
4.6 Electron Beam Chemical Vapor Deposition (EBCVD) is normally very unidirectional. However, by rotating the sample around one of its planar axes, we are able to coat the front, back, and multiples sides with a single deposition. The sample is clamped by an alligator clip attached to a chuck, which is rotated by a motor connected to electrodes inside the EBCVD vacuum chamber. 134
4.7 By design, the sputter machines deposit at an angle. For low angles of deposition, the sputtering process deposits enough material on its sides for the dielectric layers to be shorted. 134
4.8 Microscope images from a failed anodic bond attempt. Dark regions correspond to successful bonding. 135
4.9 Although aluminum passes the pull test, it very clearly fails the eye test. The difference in CTE between aluminum and the other materials ultimately resulting in the aluminum layer 'bursting' out from the α-Si material above it. 136
4.10 Although the SiN/tantanlum/SiN/Si stack demonstrated a successful anodic bond, adhesion of the layers resulted in a failure of the process. Postmortem analysis revealed separation between the Ta layer and the bottom RF-sputtered SiN layer. However, the adhesion between the top SiN layer on the Ta was good. 138
4.11 Plot of current vs. time during the anodic bonding process for a W conductive layer. Although it does not match the ideal form observed with tantalum in Fig. 4.10, the strong and continuous pull of current is indicative of a successful bond. 140

5.1 Diagram of the optical setup 142
5.2 Images of sidewall roughness taken around the time of sample Loss Test 4A (LT4A), whose measured optical quality factors are given in the tables below. 145
5.3 Subset of the original SRNB tests, comparing successful (a) and failed (b) releases. Patterns were entirely defined by E-beam lithography 147
5.4 Demonstration of the release of a 'snap-release' nanobeam to yield a nanomechanical resonator in close proximity to an optical ring resonator. 148
5.5 Optomechanical coupling splits on the order of 50 nm were obtained using our SRNB fabrication process. 149
5.6 The thinnest SRNBs obtained were on the order of 60 nm wide. 149
5.7 SEM image of a 16 µm radius optical ring resonator with a 20 µm long SRNB. 150

5.8 SEM image of a 24 µm radius optical ring resonator with a 40 µm long SRNB. 151
5.9 SEM image of one of the shorter SRNBs coupled to a relatively large optical ring resonator ($R = 40\,\mu m$). 152
5.10 Raw optomechanical signals from the Zurich HF2LI for OB5-D5i and OB5-D6i, respectively 153
5.11 OB5-D6i optomechanical signal taken at atmospheric pressure. Fit to a Cauchy Distribution gives $\mathcal{Q}_m = 15.9 \pm 2.6$ 154
5.12 SEM image of an SRNB from OB5-D5 array, giving an approximate width of 75 nm. 154
5.13 Image of the optical setup at Leiden University. It is functionally equivalent to Fig. 5.1, but high magnification lens are used to focus the laser source light onto the input facet, as well as collimate light from the drop port onto the photodiode. 156
5.14 Measurement of the optomechanical interaction as a function of pressure, obtained using the vacuum setup shown on the previous page. This data is collected on device OB19B-D6e (fabricated April 26, 2018). 157
5.15 Measured $\mathcal{Q}$ values as a function of gauge pressure. Fitting the data to Eq. 5.1 estimates the mechancal quality factor to be $\mathcal{Q}_{mech} = 39300 \pm 500$, with the predicted $\mathcal{Q}_m$ at atmosphere to be $\mathcal{Q}_{atm} = 14.4 \pm 0.9$. 158

List of Tables

1.1 Parameters of optomechanical systems defined throughout this chapter . 9

2.1 Values of α_j for low-stress, doubly-clamped beams 56
2.2 Calculation Parameters of Sample SRNB 94

3.1 Chromium Etch Multi-Recipe: Remove resist, then clean (failed) 117
3.2 Chromium Etch Multi-Recipe: DUV Lithography 117
3.3 Chromium Etch Multi-Recipe: Electron Beam Lithography 118
3.4 Optimized Chromium Etch 119
3.5 Si_3N_4 Vertical Etch (CHF_3-based) 121
3.6 Si_3N_4 Vertical Etch (no CHF_3) 121

4.1 CTE for Relevant Materials 133
4.2 Ta Layer Stack 137
4.3 Proposed tantalum stack for wafer bonding 139

5.1 Loss Test 4A R16 145
5.2 Loss Test 4A R25 145
5.3 Loss Test 4A R50 145
5.4 Loss Test 10A R16 146
5.5 Outside Bridge 15, width = 800 nm 146
5.6 SRNB Parameters, and Measured 154
5.7 Comparison of measured frequencies to model values 155

This page intentionally left blank.

Introduction

The intersection of quantum mechanics and general relativity is a unique point of interest for every physicist of the last 100 years. Both frameworks have endured success after success as their predictions have been confirmed with every relevant experiment conducted in the last century, without exception. Nevertheless, the two theories seem incompatible with each other, each producing nonsensical predictions when extrapolating beyond the general confines of each respective theory. It is for this reason that the fabrication and optimization of macroscopic systems exhibiting quantum mechanical effects is invaluable for testing and expanding our understanding of the laws of nature. With such systems, it is expected to be systematically possible to probe interactions between masses, and therefore gravity itself, in the transition regime between quantum and classical mechanics.

The purpose of the research presented in this thesis is to develop such systems through on-chip integration of nanoscale mechanical resonators into optical circuits. A unique feature of these devices is the so-called 'snap-release' mechanism demonstrated in Figure I, by which tensile stress is released to bring the beam closer to an optical ring resonator than is possible using standard electron-beam lithography and subsequent dry etching. Although the technology presented here is too undeveloped for implementation of quantum control protocols and the probing of gravity-quantum interactions, these preliminary results warrant optimism for the eventual optical cooling of the devices near the side-

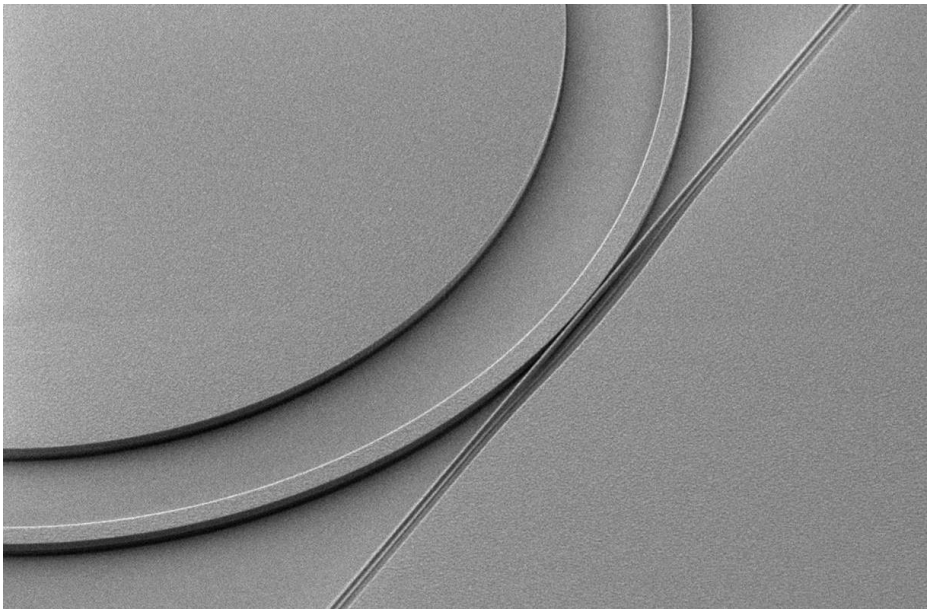

Figure I A nanomechanical oscillator within 100 nm of an optical ring resonator, obtained using a 'snap-release' mechanism.

band resolved regime. The 'snap-release' mechanism on its own could prove valuable to alternative optical cavity geometries.

A Personal Motivation

Before diving into the technical aspects of the design and fabrication of optomechanical devices, let us step aside and examine a potential point of intersection between quantum mechanics and gravity that interests us: the interpretation of quantum mechanics itself. In particular, there is much debate over how to interpret the so-called *collapse* of the wave function, when a physical system in a superposition of several eigenstates of an observable appears to reduce to a single eigenstate. There exist a number of contending theories, each presenting a unique view of the underlying mechanics of quantum mechanics.

The Copenhagen Interpretation is, by far, the most commonly taught interpretation

of quantum mechanics, and in some ways is considered the default interpretation. The Copenhagen Interpretation stipulates that the collapse is forced by the act of measurement itself. Referencing the infamous Schrodinger's Cat, the act of opening the box disturbs the system inside it, causing the cat to end up in either the *alive* or *dead* state, no longer both. It seems, in fact, the curiosity of the observer kills the cat 50% of the time.[1]

An interpretation of quantum mechanics that is potentially experimentally distinguishable from the Copenhagen Interpretation was developed by Roger Penrose in the late 90s [1, 2]. The appropriately named Penrose Interpretation predicts that the incompatibility of eigenstates with different spacetime metrics leads to an inevitable collapse of the superposition into one of the component eigenstates. The source of this incompatibility inherently comes from the time-evolution of a quantum state being given by

$$|\psi(t)\rangle = e^{-iHt/\hbar}\,|\psi(0)\rangle \tag{0.1}$$

If we consider a system initially in a superposition of states $|\psi\rangle$ and $|\chi\rangle$, we can include the gravitational information of each state as follows:

$$|\psi(0)\rangle = \alpha\,|\phi\rangle\,|G_\phi\rangle + \beta\,|\chi\rangle\,|G_\chi\rangle \tag{0.2}$$

where $|G_\phi\rangle$ and $|G_\chi\rangle$ are the gravitational states of $|\phi\rangle$ and $|\chi\rangle$. Penrose argues that the very idea of time propagation of such a state through a time-translation operator is ill-defined when considering an inherent mismatch of t between $|G_\phi\rangle$ and $|G_\chi\rangle$. This leads to the *Penrose Postulate*:

[1] Refined arguments might point toward the walls or air molecules of the box as the observer, but that is a different topic altogether.

Let f and f' be the acceleration 3-vectors of the free-fall motion in the two space-times, also thought of as the gravitational force per unit mass. At each point, the scalar $(f - f')^2$ is a measure of *spacetime incompatibility*. For a macroscopic object of arbitrary shape (a lump), the integral over the mass distribution:

$$\Delta = \int d^3x (f - f')^2 \tag{0.3}$$

is a measure of the incompatibility of the lump to be in a superposition of states at $\vec{x}$ and $\vec{x}'$. Through writing the force as the gradient of a potential, $f = -\nabla\Phi$ and using Poisson's formula, $\nabla^2\Phi = 4\pi G\rho$, we end up with:

$$\Delta = 4\pi G \int d^3x \int d^3y \frac{\big(\rho(x) - \rho(x')\big)\big(\rho(y) - \rho(y')\big)}{|x - y|} \tag{0.4}$$

which is comparable to the self-energy in classical electrodynamics [3]. We take the quantity

$$E_\Delta = \frac{1}{4\pi G} \int d^3x (f - f')^2 \tag{0.5}$$

to be the gravitational self-energy of a lump of mass to be at two different positions in spacetime. This leads to gravitational-induced decoherence between on the scale of $\tau \sim \hbar/E_\Delta$.

As far as Schrodinger's Cat is concerned with this postulate, this implies that opening the box is not necessary for the cat's fate to be decided. The difference in body position between the dead and alive states forces the wave function to collapse prior to observation.

To test the Penrose Postulate is theoretically easy. All you need to do is place macroscopic objects of various masses and volumes in quantum superpositions that involve gradients in gravitational force, and measure the timescales at which they are no longer able to maintain quantum superpositions [4]. Experimentally, this is very challenging [5].

Cavity Optomechanics

Cavity Optomechanics is a growing field of physics motivated by probing theories such as the Penrose Postulate. Using interferometric techniques to 'trap' light temporarily with a test mass, the measurable interaction between that light and the mass is strongly enhanced. By performing measurements on the light, we are then able to obtain information about its interaction with the mass. In 2003, Marshall, Simon, Penrose, and Bouwmeester [6] proposed a cavity optomechanics experiment in which a mirror, consisting of approximately 10^{14} atoms, is placed in a quantum superposition using an interferometer. The behavior of the system as function of the mirror mass then acts as a probe of mass-dependent quantum effects. Since then, the Dirk Bouwmeester Group at UC Santa Barbara has actively pursued the design, fabrication, and characterization of new devices capable of probing the quantum effects of macroscopic objects.

Rather than improve or optimize a previously existing design, for the focus of my dissertation I designed and developed a new one. Current optomechanical systems are typically assembled in a piece-by-piece approach, adding complications along every step of the experiment, and severely limiting the scalability of the systems. I designed and fabricated a novel optomechanical system which is fully integrated onto a single wafer, and thus needs minimal overhead compared to the initial fabrication of the devices. By hand, it takes less than a minute to switch between adjacent optomechanical systems, with 432 systems being fabricated during a single processing run. The design allows for modification of the optomechanical system between processing runs, while still using the same stepper lithography masks.

Contents of Thesis

As this is the first generation of a novel type of integrated optomechanical devices, many complications have been encountered and eventually overcame. The format and styling of this thesis is aimed at a complete understanding of the design and processing, with the intention to provide a detailed exposition of the technical aspects of the devices for future generations of researchers working on this project.

Chapter 1: The underlying theory of optomechanical systems is explored. We look at standard figures of merit, the linearized optomechanical Hamiltonian, and the resulting quantum protocols for optical cooling and the generation of entangled states. After a brief review of current optomechanical systems, we propose a new integrated optomechanical design in which the entire system is fabricated from a single layer of high-stress Si_3N_4.

Chapter 2: Relevant calculations and simulations are presented for each element of the proposed optomechanical system, starting with independent simulations of optical ring resonators and 'snap-release' nanomechanical resonators. Afterwards, we predict the optomechanical response of our design from simulation results.

Chapter 3: We present the fabrication procedure and optimization of high quality optical ring resonators and 'snap-release' nanomechanical resonators.

Chapter 4: A novel method of wafer bonding is explored which should lead to hermetically sealed optomechanical samples at vacuum pressures below 10^{-5} mbar.

Chapter 5: We present the characterization results of the optical quality factors of our ring resonators and the measured optomechanical response of system at room temperature and pressure.

Chapter 1

Cavity Optomechanics

The manipulation of physical systems using the radiation pressure of light has enjoyed a rich history dating back to the beginning of experimental physics itself. In 1619, it was Johannes Kepler who first postulated the ability for light to transfer momentum to physical objects, correctly predicting why comets have a tail pointing away from the sun [7]. After experimental verification of the radiation pressure force in 1901 [8], it was used to transfer the angular momentum of photons to a macroscopic object in 1936 [9]. Since then, radiation pressure has been employed in a number of important techniques and experiments, from optical tweezers[10] to the recent detection of gravitational waves from binary blackhole and neutron star systems at LIGO [11, 12].

Optical cavities prove to be an invaluable asset in the implementation of interactions mediated by radiation pressure. Light on resonance with a cavity gets 'trapped' by its boundary conditions and consequently interacts with the same points in space hundreds, thousands, or even millions of times before escaping. This naturally leads to an enhancement of any interaction between the light and anything in the cavity. In fact, it was only by utilizing this enhancement that LIGO was able to detect gravitational waves despite it's arms being *only* 4 km long. Otherwise, each arm would have necessarily been on

the order of $c/150\,\mathrm{Hz} \approx 2000\,\mathrm{km}$ long to be able to resolve the spacetime fluctuations of a system rotating at 75 times per second. Any systems which take advantage of this cavity-enhancement belong to the branch of physics known as *cavity optomechanics*.

This chapter introduces the fundamental theory of cavity optomechanical systems and the motivation and basis of our new design. First, we explore the canonical optomechanical system and associated experimental figures of merit. The optomechanical Hamiltonian and relevant quantum control protocols are then covered. We look at the current design and progress of the 'trampoline resonator' design developed by the Bouwmeester Group of UC Santa Barbara. After discussion of drawbacks of such free-space options, we introduce the design for a new photonic integrated optomechanical system.

Table 1.1: Parameters of optomechanical systems defined throughout this chapter

Symbol	Definition
ω_L	frequency of input laser
ω_{cav}	frequency of optical cavity
Ω_m	frequency of mechanical oscillator
κ_{ex}	cavity intensity decay rate associated with input coupling
κ_{int}	cavity intensity decay rate from internal loss
κ	total cavity intensity decay rate $\kappa = \kappa_{ex} + \kappa_{int}$
Γ_m	mechanical damping rate
$\mathcal{Q}_{cav}$	quality factor of optical cavity
$\mathcal{Q}_m$	quality factor of mechanical element
G	frequency shift of the cavity per unit displacement of the mechanical oscillator: $G = \frac{\partial}{\partial x}\omega_{cav}(x)$
$\Delta\omega_{FSR}$	free-spectral range of the optical cavity (Eq. 1.2)
$\mathcal{F}$	The finesse of the cavity (Eq. 1.5)
fQ	the fQ product of the mechanical oscillator: $fQ = f_m\mathcal{Q}_m$ (Eq. 1.8)
x_{ZPF}	zero-point fluctions of the mechanical oscillator (Eq. 1.15)
α	average coherent amplitude of light in a resonant cavity $\alpha = \langle\hat{a}\rangle$
g_0	optomechanical single-photon coupling strength (Eq. 1.17)
g	cavity-enhanced single-photon coupling $g = g_0\alpha$ (Eq. 1.28)

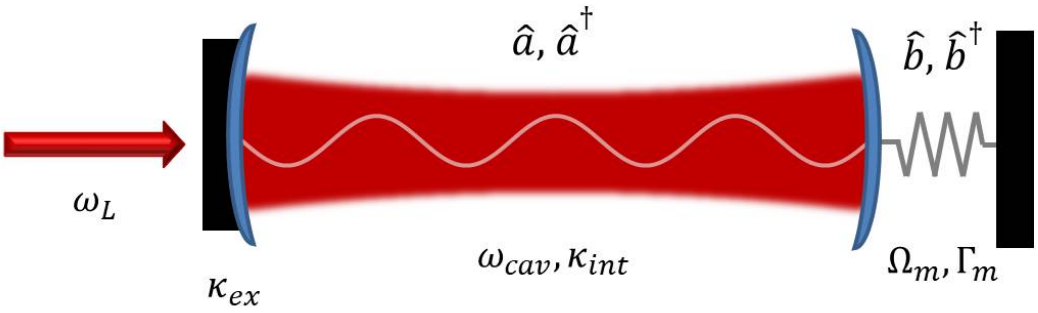

Figure 1.1: Fabry-Perot cavity with moveable mirror attached to a harmonic oscillator.

1.1 Theory of Cavity Optomechanics

The canonical cavity optomechanical system is a Fabry-Perot cavity with one of its mirrors fixed and the other attached to a mechanical oscillator, depicted in Fig. 1.1. For a cavity of length L, resonances are found when the laser frequency ω_L satisfies the condition

$$\omega_L = m \cdot 2\pi \frac{c/n}{2L} \tag{1.1}$$

where n is the index of refraction of the cavity medium (typically air or vacuum), and m is any integer. The frequency separation between two resonances is known as the free spectral range (FSR) of the system, and is given by:

$$\Delta\omega_{FSR} = 2\pi \frac{c/n}{2L} \tag{1.2}$$

An alternative equation for the FSR, defined in terms of wavelength instead of frequency, is given by:

$$\Delta\lambda_{FSR} = \frac{\lambda_L^2}{2nL} \tag{1.3}$$

where λ_L refers to the wavelength of the laser.

1.1.1 Optical Finesse and fQ Product

To represent losses in the optical cavity, we define the cavity intensity decay rates κ_{int} and κ_{ex}, corresponding to coupling into/out of the cavity and to internal propagation loss within the cavity, respectively. The total cavity intensity decay rate is thus simply $\kappa = \kappa_{ex} + \kappa_{int}$. We can then define two figures of merit for the goodness of a cavity, the optical quality factor $\mathcal{Q}_{opt}$ and the optical finesse $\mathcal{F}$. The quality factor is the average number of oscillations a photon undergoes before scattering out of the system:

$$\mathcal{Q}_{opt} = \frac{\omega_L}{\kappa} \tag{1.4}$$

The finesse corresponds to the average number of 'round-trips' the photon makes in a cavity before scattering out, and is given by

$$\mathcal{F} = \frac{\lambda_L/n}{2L}\mathcal{Q}_{opt} = 2\pi\frac{1}{\kappa}\frac{c/n}{2L} \tag{1.5}$$

The finesse is generally considered the critical figure of merit of the optical component of an optomechanical system, as it corresponds to the average number of interactions a photon makes with the movable mirror. A higher finesse directly corresponds with a stronger enhancement of the optomechanical interaction relative to loss.

The mechanical component of the system has similarly defined parameters, a mechanical frequency Ω_m and mechanical loss Γ_m. The mechanical quality factor is given by:

$$\mathcal{Q}_m = \frac{\Omega_m}{\Gamma_m} \tag{1.6}$$

For cavity optomechanics, the critical physical property of the mechanical component of the system is its ability to remain isolated from the thermal environment around it. This determines how long the oscillator is able to remain in its quantum ground state. Most

applications of optomechanics require that the mechanical system exchange less than a single thermal phonon with the environment per mechanical oscillation [13, 14]. If less than 1 phonon of energy $\hbar\Omega_m$ is lost per oscillation, this leads to the condition:

$$\mathcal{Q}_m > 2\pi \frac{k_B T}{\hbar \Omega_m} \tag{1.7}$$

noting that another definition of the Q-factor is 2π times the ratio of energy stored in the resonator to energy lost per oscillation. Using the linear mechanical frequency instead of the angular one, we substitute $\Omega_m = 2\pi f_m$ and rearrange Eq. 1.7 to get the condition:

$$f_m \mathcal{Q}_m > \frac{k_B T}{\hbar} \tag{1.8}$$

The right side of this equation is determined by temperature of the surrounding environment, which is independently determined by our experimental ability to cool the sample down to the lowest temperatures possible. The left side of the equation is appropriately named the fQ product (or sometimes Qf product), and is considered the critical figure of merit for the mechanical component of an optomechanical system.

Both the finesse of the optical cavity and the fQ product of the mechanical resonator give insight into the two components, independently. However, to gain insight on how these two systems work together, we must go into the Hamiltonian formalism of optomechanics.

1.1.2 Hamiltonian Formalism

Let us derive the optomechanical Hamiltonian for the system shown in Fig. 1.1. Excitations in the intracavity optical field $(\hat{a}, \hat{a}^\dagger)$ are coupled to phonon excitations of the mechanical oscillator $(\hat{b}, \hat{b}^\dagger)$ through the position of the mirror. To show this, we start

with the expected Hamiltonian for the setup in Fig. 1.1, which at first glance appears to be uncoupled:

$$\hat{H} = \hbar\omega_{cav}\hat{a}^\dagger\hat{a} + \hbar\Omega_m\hat{b}^\dagger\hat{b} \tag{1.9}$$

However, since ω_{cav} is dependent on the position of the moveable mirror x, we are able to introduce coupling through a first-order Taylor expansion:

$$\omega_{cav}(x) \approx \omega_{cav} + \hat{x}\frac{\partial}{\partial x}\omega_{cav}(x) \tag{1.10}$$

$$\approx \omega_{cav} - \hat{x}\,G \tag{1.11}$$

where $G = -\frac{\partial}{\partial x}\omega_{cav}(x)$ is the optical frequency shift per displacement. For a standard optical cavity, we find

$$G = -\frac{\partial}{\partial x}\left[\omega_{cav}\left(1+\frac{x}{L}\right)^{-1}\right] \tag{1.12}$$

$$\approx -\frac{\partial}{\partial x}\left[\omega_{cav}\left(1-\frac{x}{L}\right)\right] = \frac{\omega_{cav}}{L} \tag{1.13}$$

As for $\hat{x}$, we rewrite it in terms of the phonon annihilation and creation operators:

$$\hat{x} = \sqrt{\frac{\hbar}{2m_{eff}\Omega_m}}(\hat{b}+\hat{b}^\dagger) = x_{zpf}(\hat{b}+\hat{b}^\dagger) \tag{1.14}$$

where x_{zpf} is the zero-point fluctuation amplitude of the harmonic oscillator. It is found by taking the square-root of the expectation value of the displacement squared:

$$x_{ZPF} = \langle\hat{x}^2\rangle^{1/2} = \langle 0|\hat{x}^2|0\rangle^{1/2} = \sqrt{\frac{\hbar}{2m_{eff}\Omega_m}} \tag{1.15}$$

where m_{eff} is the effective mass of the mechanical oscillator. Putting this all together gives:

$$\omega_{cav}(x) \approx \omega_{cav}\Big(1 + \frac{x_{zpf}}{L}(\hat{b} + \hat{b}^\dagger)\Big) \tag{1.16}$$

Substituting this into Eq. 1.9 yields

$$\hat{H} \rightarrow \hat{H} - \hbar\omega_{cav}\frac{x_{zpf}}{L}\hat{a}^\dagger\hat{a}(\hat{b} + \hat{b}^\dagger) \tag{1.17}$$

This additional term is our interaction Hamiltonian:

$$H_{int} = -\hbar g_0 \hat{a}^\dagger\hat{a}(\hat{b} + \hat{b}^\dagger) \tag{1.18}$$

where $g_0 = \omega_{cav}\frac{x_{zpf}}{L}$ is the single-photon optomechanical coupling parameter.

Let us establish a strong optical field in the cavity using a laser, such that fluctuations in the optical field are considered small. This leads to the substitution $\hat{a} \rightarrow \alpha + \hat{a}$, where $\alpha = \langle\alpha\rangle$ is the average coherent amplitude of the optical field in the cavity. This changes our interaction Hamiltonian to:

$$\begin{aligned} H_{int} &= -\hbar g_0(\alpha + \hat{a})^\dagger(\alpha + \hat{a})(\hat{b}^\dagger + \hat{b}) && (1.19)\\ &= -\hbar g_0\alpha^2(\hat{b}^\dagger + \hat{b}) - \hbar g_0\hat{a}^\dagger\hat{a}(\hat{b}^\dagger + \hat{b}) - \hbar g_0\alpha(\hat{a}^\dagger + \hat{a})(\hat{b}^\dagger + \hat{b}) && (1.20)\end{aligned}$$

We can eliminate the middle term, which is quadratic in smallness (no α). Breaking up the remaining H_{int} into zeroth and first-orders of the fluctuation amplitudes $\hat{a}^\dagger, \hat{a}$ yields:

$$\begin{aligned} H_{int} &= H_0 + H_1 && (1.21)\\ H_0 &= -\hbar g_0\alpha^2(\hat{b}^\dagger + \hat{b}) && (1.22)\\ H_1 &= -\hbar g_0\alpha(\hat{a}^\dagger + \hat{a})(\hat{b}^\dagger + \hat{b}) && (1.23)\end{aligned}$$

1.1.2.1 Radiation Pressure Force

The zeroth-order interaction term:

$$H_0 = -\hbar g_0 |\alpha|^2 (\hat{b} + \hat{b}^\dagger) \tag{1.24}$$

$$= -\hbar g_0 |\alpha|^2 \frac{\hat{x}}{x_{zpf}} \tag{1.25}$$

corresponds to the so-called radiation-pressure force

$$F_{\hat{x}} = -\frac{d}{d\hat{x}} H_0 = \hbar \frac{g_0}{x_{zpf}} |\alpha|^2 \tag{1.26}$$

of the optical field on the mechanical oscillator. As is the case with a classical harmonic oscillator under a displacing force, we can eliminate the effect by shifting the origin of our coordinate system to the new equilibrium position.

1.1.2.2 Linearized Optomechanical Hamiltonian

The most important physics of the interaction Hamiltonian is found in terms that are linear in order of the fluctuation amplitudes $(\hat{a}^\dagger, \hat{a})$. These are collected in the term:

$$H_1 = -\hbar g_0 \alpha (\hat{a}^\dagger + \hat{a})(\hat{b}^\dagger + \hat{b}) \tag{1.27}$$

$$= -\hbar g (\hat{a}^\dagger \hat{b} + \hat{a}\hat{b} + \hat{a}^\dagger \hat{b}^\dagger + \hat{a}\hat{b}^\dagger)$$

$$= -\hbar g (\hat{a}^\dagger \hat{b} + \hat{a}^\dagger \hat{b}^\dagger) + h.c. \tag{1.28}$$

where $g = g_0 \alpha$ is the cavity-enhanced coupling between the optical field and the mechanical oscillator. This is known as the linearized optomechanical Hamiltonian.

1.1.3 Sideband Generation

The two terms in Eq. 1.28 correspond to different interactions involving the exchange of energy between the optical cavity and the mechanical oscillator. Preferential selection of the different terms is possible through modulation of the laser frequency with respect to resonant frequency of the cavity. By considering the time dependence of the field operators:

$$\hat{a}(t) = \hat{a}(0)e^{-i\omega_{cav}t} \tag{1.29}$$

$$\hat{b}(t) = \hat{b}(0)e^{-i\Omega_m t} \tag{1.30}$$

we are able to see how to selectively excite the different terms. For example, by driving the Hamiltonian with the laser frequency

$$\omega_L = \omega_{cav} - \Omega_m \tag{1.31}$$

we pick out the term $\hat{a}^\dagger\hat{b}$ which had a time-dependent phase vector of $e^{i(\omega_{cav}-\Omega_m)t}$. The other terms are removed by the rotating wave approximation. The $\hat{a}^\dagger\hat{b}$ term corresponds to the creation of a photon in the optical cavity and the removal of a phonon from the mechanical resonator.

Similarly, by driving the interaction Hamiltonian with:

$$\omega_L = \omega_{cav} + \Omega_m \tag{1.32}$$

the $\hat{a}^\dagger\hat{b}^\dagger$ term is excited, which corresponds to the creation of a phonon in the optical cavity and the addition of a phonon to the mechanical resonator.

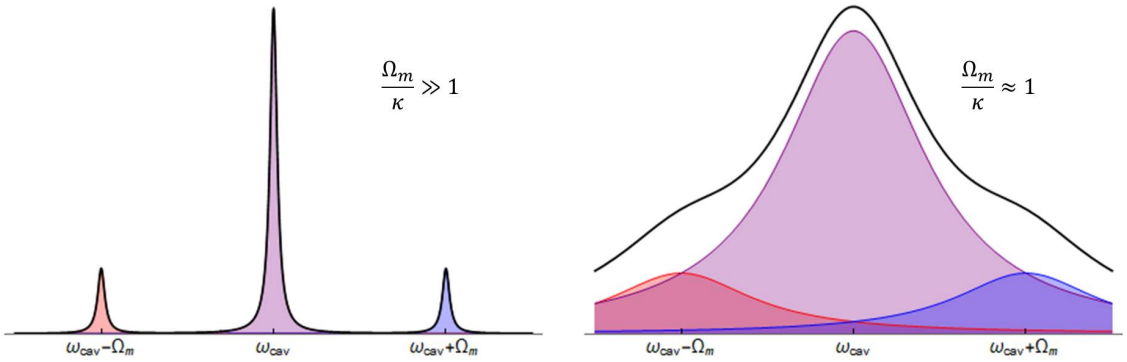

(a) Sideband resolved systems allow for clear excitation of the red-detuned, blue-detuned, or fundamental optical modes.

(b) When not sideband resolved, each resonance cannot be isolated from the others.

Figure 1.2: Optomechanical spectra demonstrating sideband characteristics. Each black line is the sum of a fundamental cavity resonance, along with the two sidebands.

Now, let us consider the absorption spectrum of the optical ring resonator. Without the optomechanical interaction, the absorption spectrum of the ring was a set of Lorentzians at the different resonant frequencies of the optical cavity. However, with the addition of the excitation of the $\hat{a}^\dagger\hat{b}$ and the $\hat{a}^\dagger\hat{b}^\dagger$ terms, additional resonances are created on either side of each ω_{cav}, detuned by $\pm\Omega_m$. These resonances are referred to as sidebands, and are the mechanism by which we are able to manipulate the mechanical oscillator through the cavity field.

For manipulation of the mechanical oscillator, it is desirable for each resonance to to be well isolated from the other resonances. In particular, overlapping of the red-detuned and blue-detuned resonances is especially undesriable as it implies a nontrivial probability of adding energy to the mechanical oscillator while attempting to remove it, and vice versa. When the sidebands are well isolated, we say that the system is sideband resolved. Mathematically, this condition is set by a high ratio of Ω_m to κ, the width of the optical resonance, as demonstrated in Fig. 1.2.

1.1.4 Sideband Cooling

As discussed in the previous section, by driving the Hamiltonian with $\omega_L = \omega_{cav} - \Omega_m$ we resonate the $\hat{a}^\dagger \hat{b}$ term that represents the creation of a photon in the optical field and the removal of a phonon from the mechanical nanobeam. Through continuous excitation of this interaction, energy will be removed from the mechanical resonator for every photon that is scattered into the optical cavity, thus lowering its temperature. This stimulated interaction, referred to as sideband cooling, is an invaluable technique for optomechanical systems. In particular, it is useful for cooling the mechanical resonator toward its quantum mechanical ground state when cryogenic cooling methods are insufficient.

We are interested in the minimum number of phonons in the resonator we can obtain using this technique for a given optomechanical system. Let A^+ and A^- be the transition rates for gaining and losing a phonon, respectively. And let Γ^+ and Γ^- be the occupation rates of phonons entering and leaving the resonator. The transition rates and occupation rates are related through Bose enhancement factors:

$$\Gamma^+ = (n+1)A^+ \tag{1.33}$$

$$\Gamma^- = nA^- \tag{1.34}$$

which will reach equilibrium when the phonon number reaches:

$$nA^- = (n+1)A^+ \tag{1.35}$$

$$\rightarrow n = \left(\frac{A^-}{A^+} - 1\right)^{-1} \tag{1.36}$$

If the phonon transitions are being driven by the interaction Hamiltonian terms through a monochromic laser, then we know the transition amplitudes are going to be proportional

to the cavity absorption spectra, given by the Lorentzians:

$$A^+ \propto \frac{\kappa/2}{(\kappa/2)^2 + (\omega_L - (\omega_{cav} + \Omega_m))^2} \tag{1.37}$$

$$A^- \propto \frac{\kappa/2}{(\kappa/2)^2 + (\omega_L - (\omega_{cav} - \Omega_m))^2} \tag{1.38}$$

Since A^+ and A^- will have the same proportionality constant, the ratio of the transition rates is given by:

$$\frac{A^-}{A^+} = \frac{(\kappa/2)^2 + (\omega_L - \omega_{cav} - \Omega_m)^2}{(\kappa/2)^2 + (\omega_L - \omega_{cav} + \Omega_m)^2} \tag{1.39}$$

This allows us to solve for the equilibrium phonon number for general ω_L:

$$n = \left(\frac{(\kappa/2)^2 + (\omega_L - \omega_{cav} - \Omega_m)^2}{(\kappa/2)^2 + (\omega_L - \omega_{cav} + \Omega_m)^2} - 1 \right)^{-1} \tag{1.40}$$

$$= \frac{(\kappa/2)^2 + (\omega_L - \omega_{cav} + \Omega_m)^2}{(\omega_L - \omega_{cav} - \Omega_m)^2 - (\omega_L - \omega_{cav} + \Omega_m)^2} \tag{1.41}$$

Now, let us look at the phonon count if we drive the system on the red-detuned sideband with $\omega_L = \omega_{cav} - \Omega_m$:

$$n = \left(\frac{\kappa}{4\Omega_m} \right)^2 = \left(\frac{1}{\mathcal{Q}_{opt}} \frac{\omega_{cav}}{4\Omega_m} \right)^2 \tag{1.42}$$

This suggests the optical and mechanical qualities of the system will not prevent us from reaching the ground state if we are in the sideband-resolved regime $\frac{\Omega_m}{\kappa} \gg 1$. However, if we are in the regime where $\frac{\Omega_m}{\kappa}$ is on the order of unity, then so will be the phonon number. Additionally, the optimal ω_L is not on top of the red-detuned sideband resonance. Let us further red-detune our laser frequency with $\omega_L = \omega_{cav} - \Omega_m - \delta\omega$, giving us:

$$n = \frac{(\kappa/2)^2 + (\delta\omega)^2}{(2\Omega_m + \delta\omega)^2 - (\delta\omega)^2} \tag{1.43}$$

Extremizing this equation leads to:

$$n_{min} = \frac{1}{2}\left(\left(1 + \frac{\kappa^2}{4\Omega_m^2}\right)^{1/2} - 1\right) \tag{1.44}$$

with

$$\begin{aligned} \delta\omega &= \sqrt{(\kappa/2)^2 + \Omega_m^2} - \Omega_m & (1.45)\\ &= \Omega_m\left(\left(1 + \frac{\kappa^2}{4\Omega_m^2}\right)^{1/2} - 1\right) & (1.46) \end{aligned}$$

We see that Eq. 1.44 matches Eq. 1.42 in the $\frac{\Omega_m}{\kappa} \gg 1$ limit, suggesting that driving the system on top of the red-detuned sideband is near optimal when operating in the sideband resolved regime. In the unresolved-sideband regime regime, when $\frac{\Omega_m}{\kappa} \ll 1$, we find:

$$n_{min} = \frac{\kappa}{4\Omega_m} \gg 1 \tag{1.47}$$

which implies an n_{min} well above the ground state.

Rearranging Eq. 1.44 gives us:

$$\left(\frac{\kappa/2}{\Omega_m}\right)^2 = 4\, n_{min}(n_{min} + 1) \tag{1.48}$$

With the substitution $\kappa = \omega_{cav}/\mathcal{Q}_{opt}$, this leads to:

$$\mathcal{Q}_{opt} = \frac{1}{4\sqrt{n_{min}(n_{min} + 1)}}\frac{\omega_{cav}}{\Omega_m} \tag{1.49}$$

which is an equation for the lower bound on the optical quality factor necessary to obtain n_{min} phonons.

To determine the lower limit on $\mathcal{Q}_{opt}$ necessary to realize ground state cooling, let us

calculate when $n_{min} = \frac{1}{2}$. For this value, we would expect the mechanical oscillator to be in the ground state approximately half of the time. From Eq. 1.49 we get:

$$\mathcal{Q}_{opt} = \frac{1}{2\sqrt{3}} \frac{\omega_L}{\Omega_m} \tag{1.50}$$

For $\lambda_L = 1\,\mu\text{m}$ light (≈ 300 THz) and a 20 MHz mechanical oscillator, this corresponds to an optical Q-factor of $\approx 4.3 \times 10^6$ as a lower bound to cool to the quantum ground state using sideband cooling (if thermal effects are ignored).

Of course, it is necessary to include the thermal environment when considering such system. However, the significance of the thermal environment is predominantly determined by the temperature of that external environment and the degree to which the optomechanical system is coupled to it. Since these effects are determined by experimental conditions, it is beyond the scope of this thesis. For in depth information on that topic with respect to our group, see the thesis of F. M. Buters. [**?**].

1.1.5 Quantum Entanglement

On the other side, the blue-detuned sideband is useful for the generation of entangled states between the optical cavity and the mechanical resonator. By driving the $\hat{a}^\dagger \hat{b}^\dagger$ resonance, we stimulate the downconversion of a photon with frequency $\omega_L = \omega_{cav} + \Omega_m$ to a photon with energy $\hbar\omega_{cav}$ and a phonon with energy $\hbar\Omega_m$. This opens the door for entanglement between multiple mechanical resonators using the ring cavity as intermediary.

Consider two mechanical resonators $\hat{b_1}, \omega_1$ and $\hat{b_2}, \omega_2$, both coupled to the same optical cavity with ω_{cav}. The mechanical resonances are being driven by two distinct lasers ω_{L1} and ω_{L2}. A fairly simple protocol can be followed to first get resonator 1 in its first-excited state and resonator 2 in its ground state, then drive a mixing of the energy between the

two resonator leading to an entangled state. The basic premise is as follows [15]:

1. Both mechanical resonators are cooled to their quantum ground state using the side-band cooling technique discussed in Section 1.1.4. This is most simply done with two long laser pulses of $\omega_{L1} = \omega_{cav} - \omega_1$ and $\omega_{L2} = \omega_{cav} - \omega_2$. This leads to the initial state:

$$|\psi\rangle = |0\rangle_1|0\rangle_2 \tag{1.51}$$

2. A short pulse of $\omega_{L1} = \omega_{cav} + \omega_1$ drives the $\hat{a}^\dagger\hat{b}_1^\dagger$ side band, exciting resonator 1 to its first excited state:

$$|\psi\rangle = |1\rangle_1|0\rangle_2 \tag{1.52}$$

3. Two red-detuned pulses are sent into the cavity, not directly on the sidebands yet still satisfying $\omega_{L2} - \omega_{L1} = \omega_2 - \omega_1$. This creates a beat in the optical field at $\omega_2 - \omega_1$, creating an effective spring constant between the two mechanical resonators [16]. Thus, using the optical cavity as an intermediary, the two mechanical resonators interact and state transfer occurs between them. This leads to the entangled state:

$$|\psi\rangle = \alpha|0\rangle_1|1\rangle_2 + \beta|1\rangle_1|0\rangle_2 \tag{1.53}$$

4. A 'readout' pulse of $\omega_{L1} = \omega_{cav} - \omega_1$ probes the optical cavity [17]. The $\hat{a}^\dagger\hat{b_1}$ interaction is impossible if resonator 1 is in its ground state. As such, the average readout power is determined by the average occupancy of resonator 1.

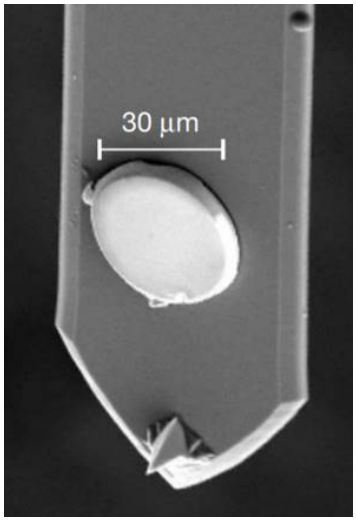

(a) First generation. Mirror mounted on AFM cantilever. (Kleckner, 2006)[18]

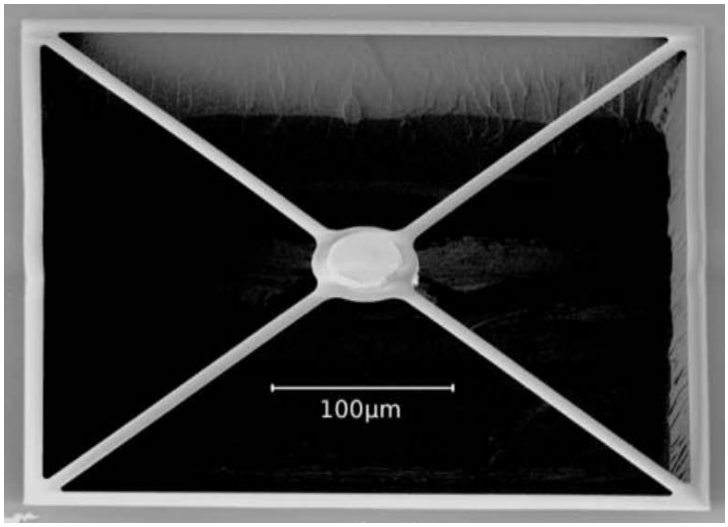

(b) Second generation - Trampoline Resonators. DBR deposited fabricated on Si_3N_4 membrane, with the bottom of the wafer etched out. (Kleckner, 2011)[19]

Figure 1.3: SEM images of early generation 'mirror on a spring' designs for optomechanical systems.

1.2 Free-Space Optomechanical Systems

Many approaches have been taken to the design and construction of systems capable of demonstrating optomechanical coupling. One simple, yet effective, strategy is to replicate the 'movable mirror' geometry studied in the previous section, depicted in Fig. 1.1 on page 10. The critical detail of such designs is figuring out how to realize a mirror on a mechanical oscillator. The first attempt of this strategy by the Bouwmeester Group at UCSB took this quite literally, gluing a mirror on the underside of a commercial cantilever designed for atomic force microscopy, shown in Fig. 1.3a. Using the sideband cooling concepts described in Section 1.1.4, the fundamental mode temperature of the cantilever was successfully cooled to 135 ± 15 mK from room temperature [18].

The next generation of devices improved the overall synergy of the system by fabricating both the mechanical oscillator and the mirror from a stack of layers on single wafer. A SiO_2/Ta_2O_5 mirror is etched in the center of a Si_3N_4 'trampoline' resonator, as

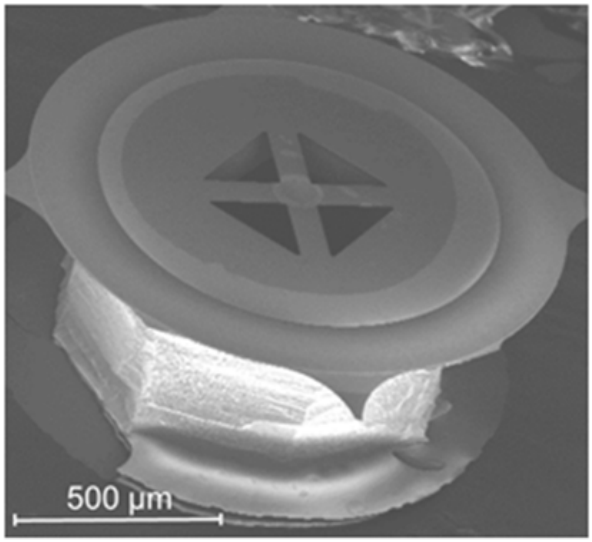

(a) Current fabrication processes involve leaving large masses on the underside of the samples to add weight.

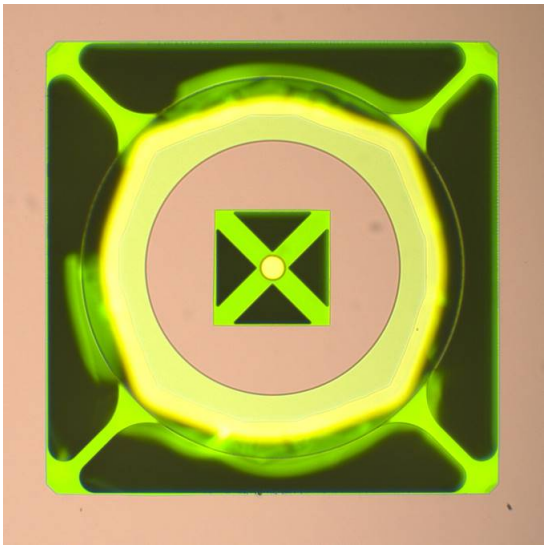

(b) A trampoline inside of a trampoline, which isolates the inner mirror from mechanical wafer modes.

Figure 1.4: Current trampoline resonators include added mass and extra stages of isolation to improve performance.

shown in Fig. 1.3b. The entire bottom side of the wafer is removed using wet and dry etch processes, allowing for the collection of light from the backside of the resonator.

The trampoline resonator design was further improved by Brian Pepper (Ph.D 2014) and Matthew Weaver (Ph.D. 2018) through various modifications of the etch geometries, and added features which increase isolation of the optomechanical system from the environment. For example, as seen in Fig. 1.4, the trampoline resonators were nested within larger trampoline resonators which served to shield the inner resonator from wafer modes that were allowing cross-talk between resonators fabricated on the same sample [20].

Beyond our group at UC Santa Barbara, a wide variety of free-space designs exist which incorporate the optomechanical interaction by having an optical cavity resonance be dependent on the position of a mechanical oscillator. For a thorough review of modern optomechanical designs, see the recent review by Aspelmeyer et al. (2014)[5].

1.3 Integrated Optomechanics

Although many successful optomechanical systems have been developed around the world, most of them suffer from complicated optical setups necessary to align and stabilize them. Most optomechanical systems are an assembly of high-quality devices constructed independently and brought together under very controlled conditions. These systems are isolated from environmental elements in vacuum chambers and cryogenically cooled down to milliKelvin temperatures, all while necessarily maintaining alignment of the component parts. As each system is cooled toward cryogenic temperatures, thermal contraction of the constituent materials modifies the alignment. Laser locking techniques are used to prevent total misalignment, but this results in heating of the system and ultimately sets a lower limit on the attainable environmental temperature.[1]

Such issues would be greatly reduced with a fully integrated platform, where the entire optomechanical system is fabricated on a single wafer. The individual components, fabricated in alignment, would remain aligned as the system is cooled to cryogenic temperatures, even as the layers contract and the sample bends. Additionally, such designs can be faster and cheaper to produce, and scalable as well. This expands the realm of potential applications for optomechanical systems, and even opens to the door towards industrialization.

To fabricate a fully integrated cavity optomechanical system, one must couple optical waveguides to a resonant structure, and have the resonance of that structure be dependent upon the position of a nanomechanical resonator. Such conditions are met by having a nanomechanical resonator in close proximity to an optical ring resonator. Exploring this system and evaluating its optomechanical coupling are covered in the remainder of this chapter.

[1] For a full treatment of experimental complications, see the thesis of F. M. Buters [**?**].

1.3.1 Optical Ring Resonators

Optical ring resonators are a natural choice for the basis of a photonic integrated system with optomechanical coupling. Ring resonators functionally work on the same principles that govern Fabry-Perot Interferometers, and follow analogous equations. The fundamental difference is that rings resonate when the optical field satisfies periodic boundary conditions around the ring, rather than Dirichlet boundary conditions at the coupling regions (mirrors). To see this, we will look at the input-output theory for our particular geometry in Section 1.3.1.1.

The behavior and functionality of ring resonators is typically determined by the number of waveguides coupled the ring. When only a single waveguide is coupled to it, the ring resonator filters its resonance frequencies from the waveguide spectrum. The light effectively gets trapped in the ring by constructive interference, and is eventually lost to scattering. When a second waveguide is coupled to a ring resonator, the light absorbed by the ring is not necessarily lost as in the previous case. Instead, the light can couple into the 2nd waveguide, where it can be collected for direct measurement or sent to another photonic element in some greater system. In either case, the photon will have information about the ring resonator imprinted on its quantum state, magnified by the number of times it traveled around the ring. For this reason, our design employs ring resonators coupled to two waveguides, sometimes referred to as a 'double-bused' ring resonator, depicted in Fig. 1.5 on the next page.

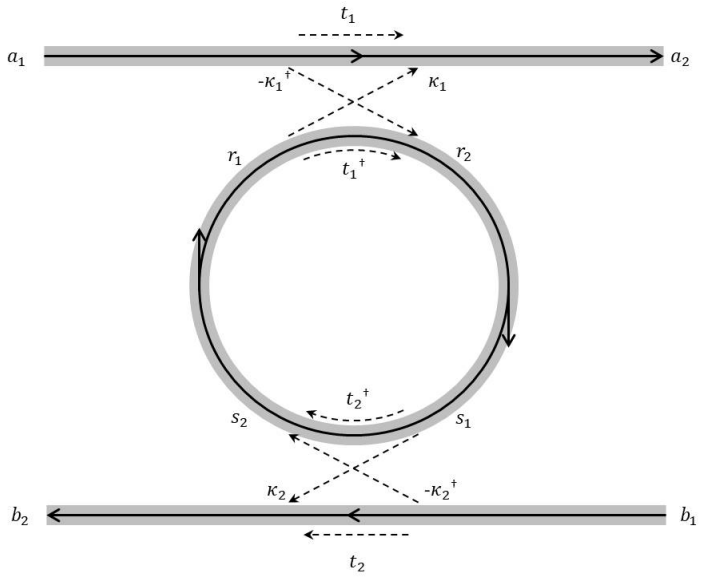

Figure 1.5: Mapping of amplitude and field definitions for characterizing properties of double-bused ring resonators.

1.3.1.1 Input-Output Theory

To understand the spectrum of double-bused ring resonators, we use input-output theory to calculate the interference effects and resonance properties. Referring to Fig. 1.5 above, we assign electric field amplitudes and phases to the waveguides of each coupling region (a_n, b_n, r_n, s_n), and we define transmission $(t_n, t_n^\dagger)$ and absorption $(\kappa_n, \kappa_n^\dagger)$ coefficients for the couplers. With the idea that $|\kappa_n|^2 + |t_n|^2 = 1$, we can write the coupling equations as:

$$\begin{pmatrix} a_2 \\ r_2 \end{pmatrix} = \begin{pmatrix} t_1 & \kappa_1 \\ -\kappa_1^\dagger & t_1^\dagger \end{pmatrix} \begin{pmatrix} a_1 \\ r_1 \end{pmatrix} \tag{1.54}$$

$$\begin{pmatrix} b_2 \\ s_2 \end{pmatrix} = \begin{pmatrix} t_2 & \kappa_2 \\ -\kappa_2^\dagger & t_2^\dagger \end{pmatrix} \begin{pmatrix} b_1 \\ s_1 \end{pmatrix} \tag{1.55}$$

The phase associated with the optical field propagating around the circumference of the rings is given by:

$$\theta_R = \frac{2\pi n_{eff}}{\lambda} 2\pi R = 4\pi^2 n_{eff} \frac{R}{\lambda} \tag{1.56}$$

where R is the radius of the ring, λ is the wavelength of the laser source, and n_{eff} is the effective index of refraction of the mode. With this quantity in mind, we can relate the fields inside the ring with the equations:

$$s_1 = r_2 \alpha_R^{1/2} \exp(i\frac{\theta_R}{2}) \tag{1.57}$$

$$r_1 = s_2 \alpha_R^{1/2} \exp(i\frac{\theta_R}{2}) \tag{1.58}$$

where α_R is the loss coefficient and phase associated with a single round trip around the ring. Using equations 1.54 - 1.58, we are able to create a self-consistent equation for the field inside the ring:

$$r_2 = r_2 t_1^\dagger t_2^\dagger \alpha_R \exp(i\theta_R) - \kappa_1^\dagger a_1 - t_1^\dagger \kappa_2^\dagger b_1 \tag{1.59}$$

and thus solve for r_2:

$$r_2 = \frac{-\kappa_1^\dagger a_1 - t_1^\dagger \kappa_2^\dagger b_1}{1 - t_1^\dagger t_2^\dagger \alpha_R \exp(i\theta_R)} \tag{1.60}$$

This allows us to solve for the general solution of the output field b_2:

$$b_2 = b_1 t_2 - \kappa_1^\dagger \kappa_2 \alpha_R^{1/2} \exp(i\theta_R/2) \frac{a_1 + b_1 t_1^\dagger \alpha_R^{1/2} \exp(i\theta_R/2)}{1 - t_1^\dagger t_2^\dagger \alpha_R \exp(i\theta_R)} \tag{1.61}$$

It is generally the case that the coupling regions on both sides are identical. In such cases, by defining $t_1 = t_2 = t\exp(i\phi_t)$ and $\kappa_1 = \kappa_2 = \kappa\exp(i\phi_\kappa)$, our general result can

simplify to:

$$b_2 = b_1 t e^{i\phi_\kappa} - \kappa^2 \frac{a_1 + b_1 t \alpha_R^{1/2} e^{i(\theta_R/2 - \phi_t)}}{1 - t^2 \alpha_R e^{i(\theta_R - 2\phi_t)}} \alpha_R^{1/2} e^{i\theta_R/2} \tag{1.62}$$

For the case in which only the input port is being excited ($a_1 \neq 0, b_1 = 0$), Eq 1.62 reduces to:

$$b_2 = \frac{a_1 \kappa^2 \alpha_R^{1/2}}{1 - t^2 \alpha_{1/2}^2 \exp(i\theta_R - 2\phi_t)} e^{i(\theta_R/2 + \pi)} \tag{1.63}$$

The power transferred from the input port (a_1) to the drop port (b_1) is then given by:

$$\frac{P_b}{P_a} = \frac{|b_2|^2}{|a_1|^2} = \frac{\alpha_R \kappa^4}{1 + \alpha_R^2 t^4 - 2\alpha_R t^2 \cos(\theta_R - 2\phi_t)} \tag{1.64}$$

$$= \frac{\alpha_R (1 - t^2)^2}{1 + \alpha_R^2 t^4 - 2\alpha_R t^2 \cos(\theta_R - 2\phi_t)} \tag{1.65}$$

$$= \frac{\alpha_R (1 - t^2)^2}{(1 - \alpha_R t^2)^2 + 2\alpha_R t^2 (1 - \cos(\theta_R - 2\phi_t))} \tag{1.66}$$

where we used the normalization condition $|\kappa_n|^2 + |t_n|^2 = 1$ to reduce the number of parameters. Noting that $\alpha_R t^2$ approaches 1 for ideal systems, we see that the system will resonate when $\theta - 2\phi_t = 2\pi n$ for integer values of n. On resonance, the transferred power is thus:

$$\left.\frac{P_b}{P_a}\right|_{\text{res}} = \alpha_R \left(\frac{1 - t^2}{1 - \alpha_R t^2}\right)^2 \tag{1.67}$$

We see that in the low-loss limit ($\alpha_R \to 1$), all of the power is transferred from the input/output waveguide to the add/drop waveguide. Had $t_1 \neq t_2$, this would have not been the case.

1.3.1.2 Resonance and Loss

Let us consider a small change in phase $\delta\theta_R$ away from the resonant condition. Taylor expanding Eq. 1.66 around a resonance yields:

$$\frac{P_b}{P_a} \approx \frac{\alpha_R(1-t^2)^2}{(1-\alpha_R t^2)^2 + \alpha_R t^2 \delta\theta_R^2} \tag{1.68}$$

which is a Lorentzian with a full-width at half maximum given by:

$$(\frac{1}{2}\Gamma_\theta)^2 = \alpha_R \frac{1-\alpha_R t^2}{\alpha_R t^2} \tag{1.69}$$

$$\rightarrow \quad \Gamma_\theta = \frac{2(1-\alpha_R t^2)}{\sqrt{\alpha_R t^2}} \tag{1.70}$$

The quality factor of such a resonance is then given by:

$$Q = \frac{\theta_R}{\Gamma_\theta} = \frac{2\pi R}{\lambda/n_{eff}} \frac{\pi\sqrt{\alpha_R t^2}}{1-\alpha_R t^2} \tag{1.71}$$

To obtain the optical finesse (average number of round trips), we simply take the quality factor (average number of oscillations) and divide it by the number of oscillations per round trip. This gives us:

$$\mathcal{F} = \mathcal{Q}\frac{\lambda/n_{eff}}{2\pi R} = \pi \frac{\sqrt{\alpha_R t^2}}{1-\alpha_R t^2} \tag{1.72}$$

At first glance, it may appear that the finesse is independent on the radius of the ring, and the quality factor can be increased by simply making the ring larger. However, α_R will be of the form

$$\alpha_R = (\alpha_L)^{2\pi R/L} \tag{1.73}$$

where L is some characteristic length associated with a certain amount of loss. For any ultra-low loss system, α_L will approach 1. With that in mind, let us for now write $\alpha = 1 - \epsilon$ where $\epsilon \ll 1$. Using the binomial approximation, we can then simplify Eq. 1.72 as follows:

$$\begin{aligned} \mathcal{F}|_{t=1} &= \pi \frac{(1-\epsilon)^{\pi R/L}}{1-(1-\epsilon)^{2\pi R/L}} && (1.74) \\ &\approx \pi \frac{1-\pi\frac{R}{L}\epsilon}{2\pi\frac{R}{L}\epsilon} && (1.75) \\ &= \frac{1}{R}\frac{L}{2\epsilon} - \frac{\pi}{2} && (1.76) \\ &\approx \frac{1}{2}\frac{L}{R}\frac{1}{1-\alpha} && (1.77) \end{aligned}$$

We see the finesse scales inversely with ring radius. This leads to the internal quality factor being independent of radius:

$$\begin{aligned} Q &\approx \frac{2\pi R}{\lambda/n_{eff}}\frac{1}{2}\frac{L}{R}\frac{1}{1-\alpha} && (1.78) \\ &= \pi\frac{L}{\lambda/n_{eff}}\frac{1}{1-\alpha} && (1.79) \end{aligned}$$

This means the upper bound of our $\mathcal{Q}$ factors is not determined by the radius of the ring, as might have appeared at first glance of Eq. 1.71. Instead, it is primarily determined by the loss per unit length of the waveguides which make it up.

Propagation loss of optical power is frequently characterized in units of [db/cm], where 3db = 50% power loss. As such, light propagating through a waveguide with 0.3 db/cm will have its power reduced to 50% after 10 cm of waveguide. Generally, losses on the order of 1 db/cm are considered good, 0.1 db/cm are considered high-quality, and 0.01 db/cm are considered ultra-high quality.

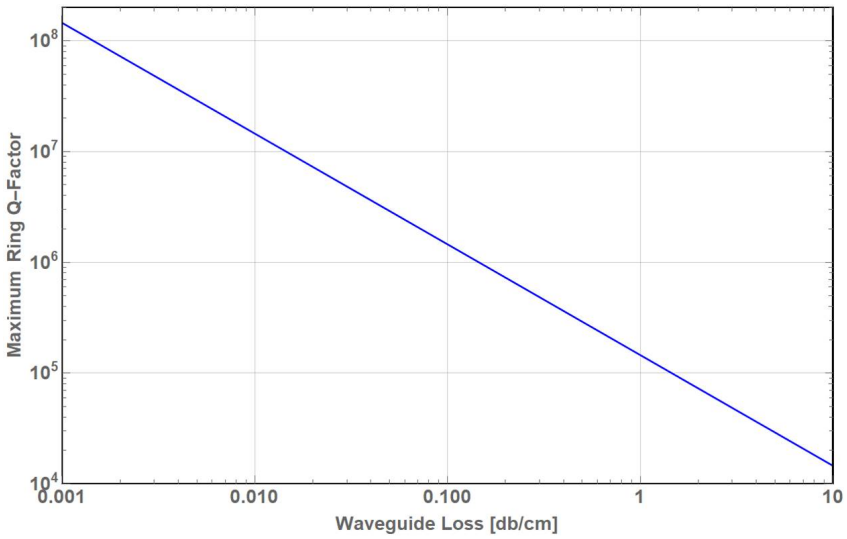

Figure 1.6: Predicted internal quality factors of ring resonators as a function of propagation loss (db/cm).

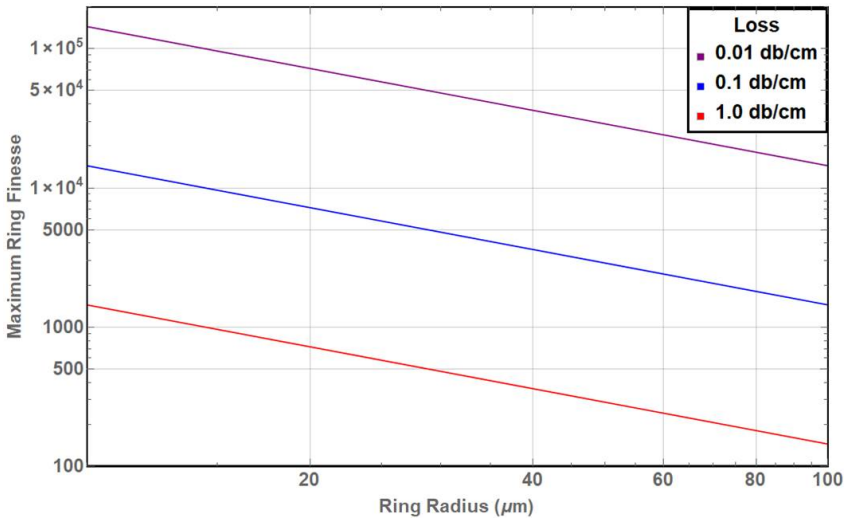

Figure 1.7: Simulated predictions of optical finesse as a function of ring radius.

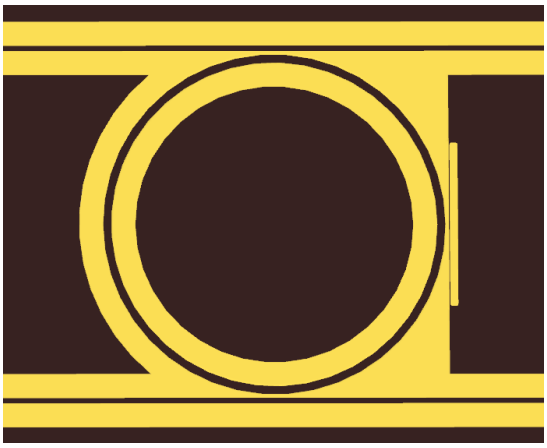

Figure 1.8: Schematic of an integrated optomechanical system, coupling a nanobeam to an optical ring resonator both fabricated from the same layer of Si_3N_4.

1.3.2 Adding an Optomechanical Interaction

By releasing a nanomechanical resonator at the outer edge of an optical ring resonator, as depicted in Fig. 1.8, we generate the optomechanical Hamiltonian derived in Section 1.1.2. Although we are not changing the physical length of the ring resonator, we are changing its *effective* length by modifying the effective index of the optical mode near the region of optomechanical coupling. In this way, the resonant frequency of the ring resonator is dependent upon the position of the released mechanical structure.

The ring resonator is coupled to two optical waveguides, diametrically opposed. One waveguide is fed by a laser source and functions as the input of the system. The other waveguide functions as the output of the system, carrying only light that had been absorbed by the ring and interacted with the nanomechanical resonator. Both the ring and bridge are fabricated from the same Si_3N_4 layer, with the bridge oscillating horizontally (in the wafer plane) to within close proximity of the outer radius of the ring.

As shown in Section 1.1.2, the strength of the optomechanical coupling is determined by $G = \frac{\partial}{\partial x}\omega_{cav}(x)$, the optical frequency shift in the resonator per unit displacement of the mechanical oscillator. In the case of the movable mirror, calculating this coupling

term required simple geometric arguments. However, estimating it for this photonic integrated system is considerably more involved. The proximity of the nanobeam to the optical ring increases the effective index of the optical modes in that region of the ring. Consequently, the movement of the nanobeam causes a predictable change in the ring's resonant frequencies.

Let $n_x(\theta)$ be the effective index of the optical mode as a function of angle around the ring, for a distance x between the ring and the nanobeam. For most the ring, $n_x(\theta) = n_\infty$, but as θ sweeps over the optomechanical region $n_x(\theta)$ increases in value. The phase shift induced by the presence of the mechanical resonator is given by:

$$\phi_{OM}(x) = \frac{2\pi}{\lambda} \int_{\theta_-}^{\theta_+} \big(n_x(\theta) - n_\infty\big) R \, d\theta \tag{1.80}$$

where we have introduced θ_- and θ_+ to restrict our integral to the region of the ring non–negligibly effected by the presence of the nanobeam.

With the knowledge that a phase accumulation of 2π will shift the phase from one resonance to the other, we know that the resulting change in frequency from such a phase shift is given by:

$$\begin{aligned}
\delta\omega_{ring}(x) &= \Delta\omega_{FSR} \frac{\phi_{OM}(x)}{2\pi} && (1.81)\\
&= \frac{c/n_{eff}}{2\pi R} \frac{2\pi R}{\lambda} \int_{\theta_-}^{\theta_+} \big(n_x(\theta) - n_\infty\big) d\theta && (1.82)\\
&= \frac{c}{\lambda n_{eff}} \int_{\theta_-}^{\theta_+} \big(n_x(\theta) - n_\infty\big) d\theta && (1.83)\\
&= \frac{\omega_{cav}}{2\pi} \frac{1}{n_{eff}} \int_{\theta_-}^{\theta_+} \big(n_x(\theta) - n_\infty\big) d\theta && (1.84)
\end{aligned}$$

Unlike the Fabry-Perot optomechanical systems, we do not find a closed-form solution for the optomechanical coupling. Instead $\delta\omega_{ring}(x)$ must be obtained from simulations of

the device geometry and numercal integration of the results. By comparing the results to the change mechanical resonator's position with respect to the ring, we are able to approximate the frequency shift per displacement, $G \approx \frac{\partial}{\partial x}\delta\omega_{ring}(x)$. These simulations and calculations are covered in Section. 2.3

This page intentionally left blank.

Chapter 2

Experimental Design and Simulation

Much work has already been done in fabricating ultra-high quality optical ring resonators. The John Bowers Group at UC Santa Barbara produces optical ring resonators with quality factors approaching 10^8 [21]. To accomplish this, they utilize Si_3N_4 deposited by Low Pressure Chemical Vapor Deposition (LPCVD) for the waveguide cores and SiO_2 for the embedding material. This latter detail is significant for the fabrication of optomechanical devices, as SiO_2 can be isotropically etched using HF solutions or vapor, with high selectivity with respect to LPCVD Si_3N_4. This gives us a method by which we are able to release freestanding mechanical nanobeams in the proximity of optical ring resonators, as long as they are fabricated from LPCVD Si_3N_4 deposited on SiO_2.

The original plan was to construct a mechanical nanobeam above Si_3N_4 ring resonators previously fabricated by the Bowers Group. However, many complications pushed us away from this layer-by-layer strategy. We moved toward a design in which the optical ring resonator and the mechanical nanobeam are both fabricated from the same layer of stoichiometric LPCVD Si_3N_4. For this to work, the thickness of the LPCVD Si_3N_4 was increased from 60 nm to 400 nm, to ensure that the primary mode of oscillation of the mechanical nanobeam is in the wafer plane. This also increases confinement of the

optical mode within the waveguide core, impacting the optical behavior in some positive and negative ways:

- The ring radii are able to get significantly smaller due to the sharp decrease in bending loss. Although the previous ring radii were on the order of 10 mm, 400 nm thick waveguides can approach radii as small as 12 µm before the bending loss is non-negligible with respect to other typical loss mechanisms. As derived in Eq. 1.77, the optical finesse scales inversely with radius. Reducing the radius by a factor of 10^3 will increase the optical finesse by a factor of 10^3. A high finesse implies stronger optomechanical coupling relative to optical loss.

- The SiO_2 cladding layer becomes less critical with stronger optical confinement to the waveguide core. We thus forego cladding the waveguides near the optical ring resonators and worry much less about reflections generated near where the nanobeam is released by undercutting.

- Increased confinement corresponds directly to stronger optical field density near the left and right edges of the waveguide core. This suggests a larger fraction of photons are interacting with waveguide sidewalls on average. Consequently, optical loss from sidewall roughness will increase.

- With lensed fibers we are unable to focus the laser light source to a spot size smaller than the waveguide mode size. Insertion losses increase.

In this chapter, we start with 2 inherently fixed parameters for our optomechanical devices:

1. **Si_3N_4 waveguide height $h_{WG} = 400$ nm**: High-stress LPCVD Si_3N_4 layers are known to suffer critical failure at thicknesses >400 nm. In short, the tensile stress of the Si_3N_4 becomes so strong that it rips the material itself apart. There is significant research on techniques that would allow for thicker layers of Si_3N_4 [22], but for now we stick with the safe upper limit of 400 nm.

2. **Laser Wavelength $\lambda_L = 1060 \pm 10$ nm**: We use a Sacher Lasertechnik brand, Litmann class tunable diode laser, model TEC-500-1060-030. This gives us access to wavelengths in the range 990–1075 nm, with operation optimized for 1060 nm. With that in mind, we consider the laser wavelength to span the range $\lambda_L = 1060 \pm 10$ nm when performing calculations and simulations.

Using these parameters as a starting point, we determine the appropriate parameter space to explore with our fabrication process. The parameters of interest are:

- **Width of ring waveguide:** Simulations of mode profiles are used to determine that 400 nm thick Si_3N_4 uncladded waveguides need to be at least 400 nm wide to support a single mode (Section 2.1.2). The actual chosen minimum width for the mask design is 600 nm, to be on the conservative side. Calculations indicate that waveguide thickness >1200 nm lead to weak optomechanical coupling (Section 2.3.1.4).

- **Radius of ring waveguide:** Simulations indicate bending loss becomes non-negligible when the ring radius is on the order of 12 µm (Section 2.1.3). We choose 16 µm as the minimum ring radius for our mask design.

- **Thickness of SiO_2 Underlayer:** Simulations indicate substrate absorption loss starts becoming an issue when the wet oxide underlayer is smaller than 2 µm (Section 2.1.4). We chose a wet oxide thickness of 3 µm.

- **Coupling Split:** This refers to the distance between the optical ring resonators and the straight waveguides in the evanescent coupling regions. Estimations of the coupling amplitudes and corresponding$\mathcal{Q}$-factors are done using FDM simulation (Section 2.1.5). However, the actual limits are determined by experimental parameters. The minimum value, 300 nm, is set by the fabrication process. Attempting stronger coupling results in the straight waveguide and ring waveguide etch geometries influencing each other. The maximum value is set by the expected optical quality factors. Our coupling splits are between 300 and 600 nm.

- **Properties of Si_3N_4 Nanobeams:** The engineering physics of the nanobeams is covered in Section 2.2. The dependency of the optomechanical coupling on the nanobeam dimensions are explored in Section 2.3.1.2.

2.1 Photonic Simulations

The PhotonD software suites FIMMWAVE and OMNISIM are used to simulate the various optical properties of our photonic integrated system in pseudo-3D (2D + $\hat{z}$). For our simulations, we restrict ourselves to two different solvers, primarily based on how well each is capable of handling *perfectly-matched layers* (PMLs). PMLs are material layers placed at the outer edges of the simulation space to force a rapid decay of fields that propagate into them. They are capable of doing this through a 'complex coordinate stretching' technique that effectively gives the outer layer real and imaginary component to its thickness. The imaginary portion of the thickness provides a boundary condition capable of satisfying reflectionless absorption of radiating fields. The two solvers we use are:

- **Film-Mode Matching (FMM)** is a semi-analytic algorithm based on using thin rectangular layers as meshing for the simulation space. As such, it is capable of producing fast and accurate calculations for specifically rectangular geometries. It is capable of handling PMLS on the side boundaries, but is not suited for PMLs on the top or bottom. This makes them great for simulating bending loss which primarily radiates along the wafer plane, but ill-suited for simulating absorption into the substrate.

- **Finite-Difference Method (FDM)** is capable of dealing with waveguides of arbitrary cross-sectional geometry, made of both real and lossy materials. Unlike FMM, it is capable of dealing with PMLs on all 4 sides, and thus is the necessary solver to use when calculating absorption loss into the substrate. Due to its robustness, computation time is generally longer, but the results are more likely to be devoid of computational artifacts. When applicable, it is recommended that FDM be used to check the results of using FMM.

2.1.1 Optical Mode Simulations

A majority of our design is determined by simulating the optical modes of waveguides given their cross-sectional geometry and curvature, and the frequency of light propagating in them. From the calculated modes, we can extract the mode's effective index, TE/TM characteristics, and various forms of loss.

As a demonstration, let us investigate the mode differences between 60 nm and 400 nm thick Si_3N_4 waveguides, both 1200 nm wide and fully surrounded by SiO_2. We use the complex FMM mode solver in FIMMWAVE, with the complex option enabled for loss calculations, to obtain the initial results shown in the Fig. 2.1. We find that thin (60 nm) waveguides are only able to support a single transverse-electric (TE) mode, and zero transverse-magnetic (TM) modes. The thick (400 nm) waveguides are able to support 3 TE and 3 TM modes. Comparing the TE1 modes of the two (Fig. 2.1a and 2.1b), we observe that a significant portion of the mode of the thin waveguide is found outside of the waveguide geometry (highlighted by a white line). On the contrary, the TE1 mode of the thick waveguide is predominantly localized inside of the waveguide geometry.

Now, let us match the geometry to a ring resonator by adding a radius of curvature. Fig. 2.2 shows the resulting cross-sectional fields when a 100 µm radius of curvature is

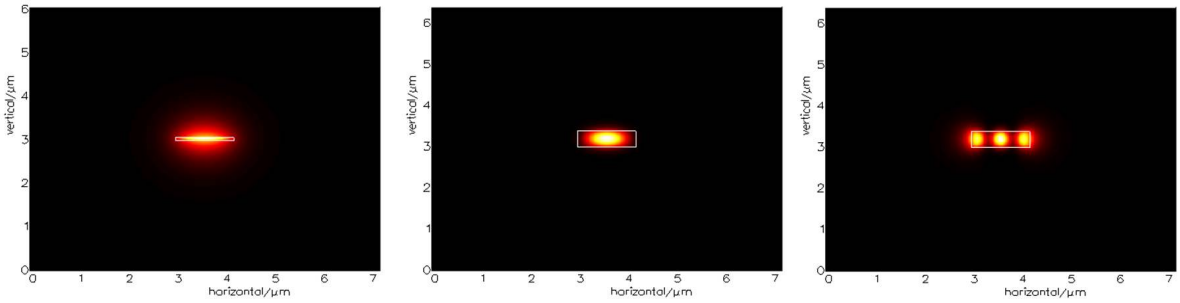

(a) TE_1, 60 nm waveguide (b) TE_1, 400 nm waveguide (c) TE_3, 400 nm waveguide

Figure 2.1: Optical mode simulations obtained using FMM mode solver in FIMMWAVE. Each waveguide is 1200 nm wide, with varying height, and composed of Si_3N_4 surrounded by SiO_2

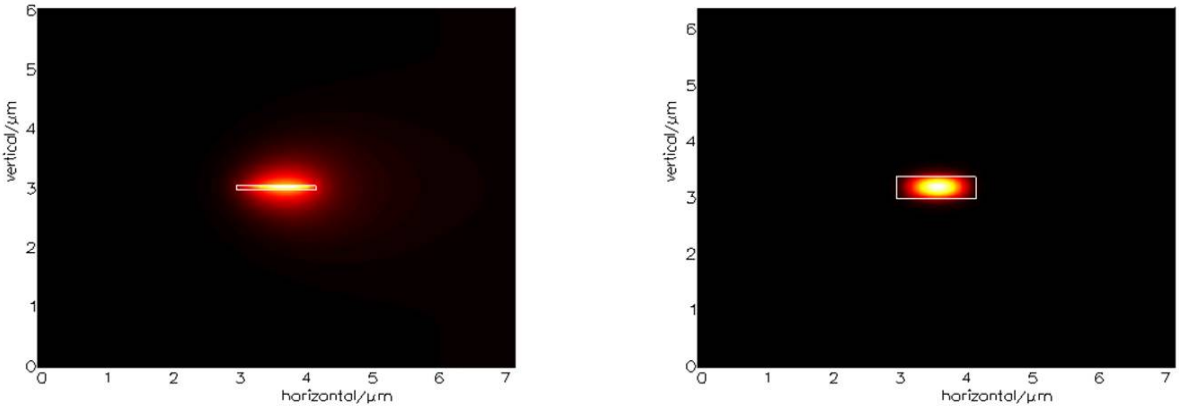

(a) TE_1, 60 nm waveguide with 100 µm radius of curvature. Measured loss: 900 db/cm

(b) TE_1, 400 nm waveguide with 100 µm radius of curvature. No bending loss measured ($< 10^{-11}$ db/cm).

Figure 2.2: FIMMWAVE simulations of bent waveguides representative of optical ring resonators. A PML is necessary on the right side of the waveguide to avoid boundary reflections from the mode distortion to that side; they also allow for direct measurement of bending loss.

enabled. The resulting distortion in the optical mode of the thin waveguide is strongly apparent. By adding a PML to the right-side geometry to absorb the radiation lost in that direction, we find that the bending loss of the thin waveguide is approximately 900 db/cm. The thick waveguide has no apparent distortion from the implementation of the 100 µm radius of curvature. Not only that, but no detectable bending loss was measured by the PMLs at the boundary, indicating that it was below the software threshold of 10^{-11} db/cm. As we will further elaborate on in Section 2.1.3, these thick rings are therefore capable of getting considerably smaller before bending loss becomes non-negligible.

By building these simulations entirely by parameter definitions, we are able to sweep across the prospective parameter space of our ring resonators to determine which range of parameters to investigate experimentally with our fabricated devices.

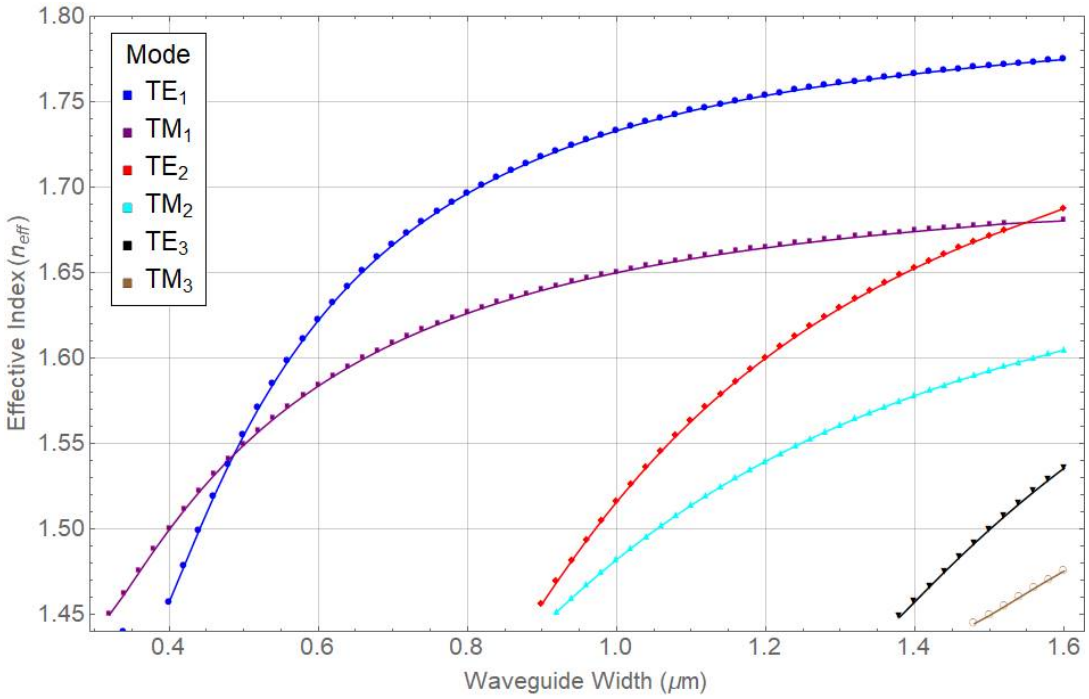

Figure 2.3: Effective index n_{eff} for Si_3N_4 waveguides of varying widths. Caculations are performed using the FFM mode solver, with PMLs placed on both sides of the simulation space.

2.1.2 Waveguide Width

Figure 2.3 shows the TE and TM mode characteristics for 400 nm thick Si_3N_4 waveguides fabricated on top of SiO_2, with air cladding. We see that the waveguides are able to support a single mode down to about 400 nm wide. The simulations predict they become multimode when the width is on the order of 900 nm.

As the data shows, there is difference in the n_{eff} between the TE1 and TE2 modes. This leads to a difference in the the free spectral ranges of their resonances within the ring, and thus them having significantly different resonant frequencies. With this in mind, overlapping resonances are possible. We chose to fabricate a mixture of single-mode and double-mode rings, ranging in width from 600 nm to 1200 nm.

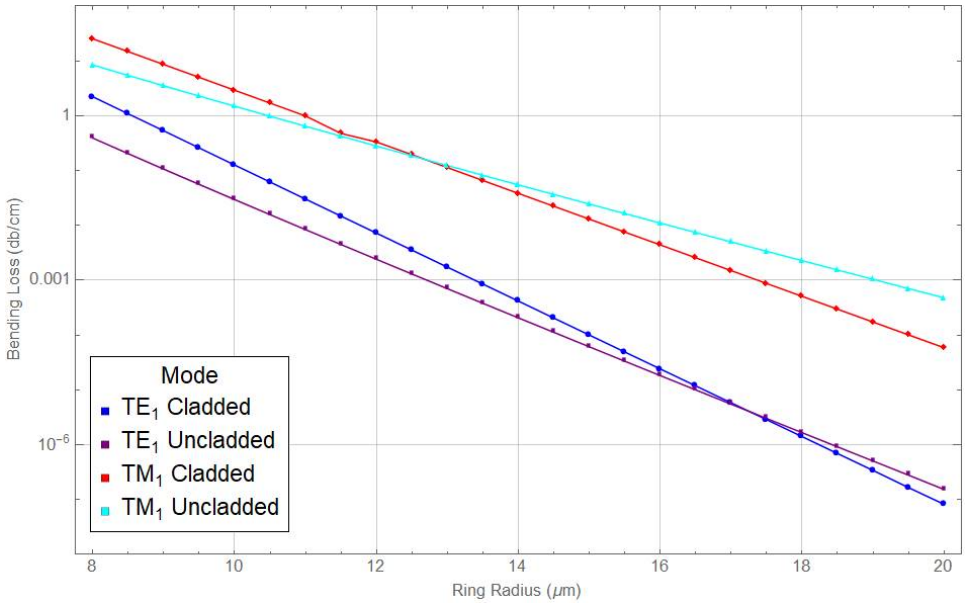

Figure 2.4: Comparison of simulated bending loss for the modes of 400 nm × 800 nm Si_3N_4 waveguides, obtained using the FMM mode solver in FIMMWAVE

2.1.3 Bending Loss

Figure 2.4 shows bending loss simulations for 400 nm × 800 nm Si_3N_4 waveguide cores on SiO_2, both with and without SiO_2 cladding. We observe:

- For both cladded and uncladded waveguides, the TM modes are more sensitive to bending loss than TE modes.
- Although the presence of cladding does seem to effect the bending loss, the differences in the results are not significant.
- If we consider propagation loss from bending to be acceptable at 0.01 db/cm, then the critical radius of curvature is around 11 µm for TE modes and 14 µm for TM modes.

With all of this taken into account, we chose to focus on rings with a minimum radius of 16 µm (with respect to the outer edge). According to the simulations, this corresponds to $<10^{-5}$ db/cm for the TE modes, and on the order of 10^{-3} for the TM modes.

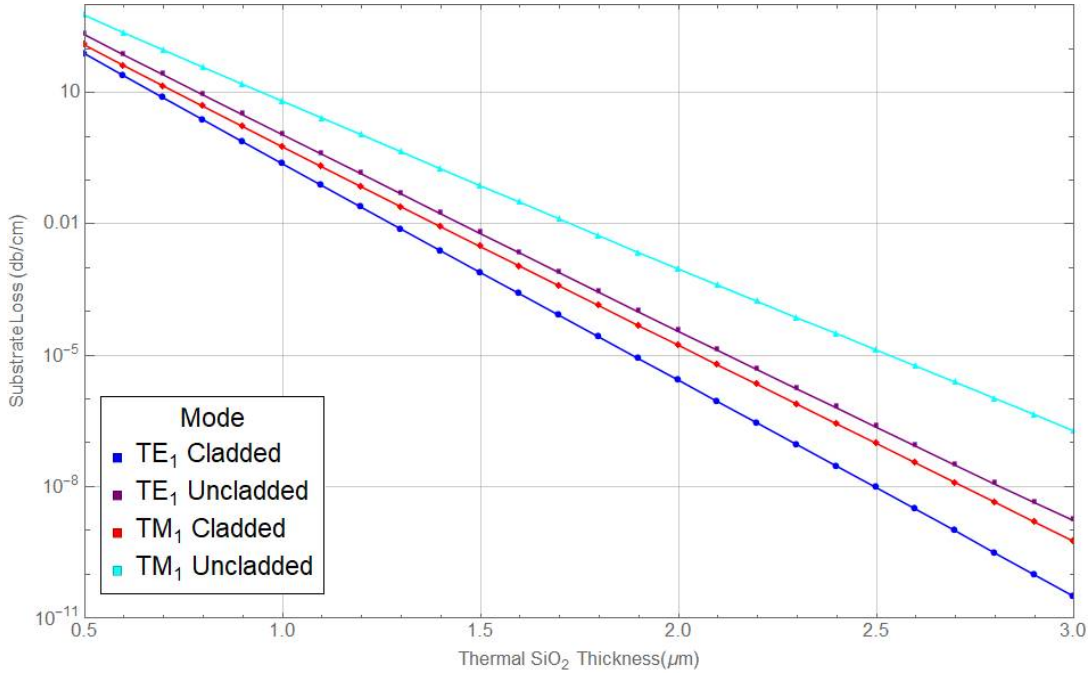

Figure 2.5: Simulated absorption loss for a 800 nm wide Si_3N_4 waveguide, as a function of thickness of the SiO_2 layer between the Si substrate and Si_3N_4.

2.1.4 Thickness of Thermal SiO_2 Base Layer

Due to the high index of refraction of pure silicon ($n \approx 3.67$ at 1060 nm), any portion of the mode that propagates in silicon substrate is lost at a rapid rate. It is necessary for us to use the complex FDM solver in FIMMWAVE, which allows us to place PMLs at the bottom boundary where we would naturally expect the loss to propagate.[1]

Substrate absorption loss was studied for both cladded and uncladded waveguides. The significant results are shown in Fig. 2.5. The uncladded waveguides exhibit stronger substrate loss than the cladded waveguides fully encapsulated in SiO_2. We also see that the TM modes are more lossy than the TE modes by an order of magnitude.

[1]Initial simulations using the FMM solver predicted acceptable losses with an SiO_2 layer of 500 nm between the 400 nm LPCVD Si_3N_4 layer and the Si substrate. This seemed reasonable given the strong confinement of the mode and that the distance from Si substrate to the Si_3N_4/SiO_2 interface was 2.5 times the distance from the center of the waveguide to its bottom edge. However, these predictions were flawed due to the inability for FFM to deal with PML on the bottom boundary of the simulation space. As a result, non-functional rings were fabricated with an undercladding thickness of 500 nm. It took some time to realize that this undercladding thickness was the cause of detrimental losses.

Our original intent behind having a thin SiO_2 layer between the Si substrate and the LPCVD Si_3N_4 was to allow for simple anodic bonding between our sample and Borofloat-33 glass (Chapter 4). For this to work, the total thickness of both the SiO_2 and Si_3N_4 would have needed to be below 1 µm. These simulations indicate that such a target is impossible. As there is no benefit to using an intermediate value, we chose 3 µm as the thickness of the thermal SiO_2 layer. If there were reason to do so, the simulations indicate that one might achieve good results with a 2 µm thick thermal oxide layer, for most applications.

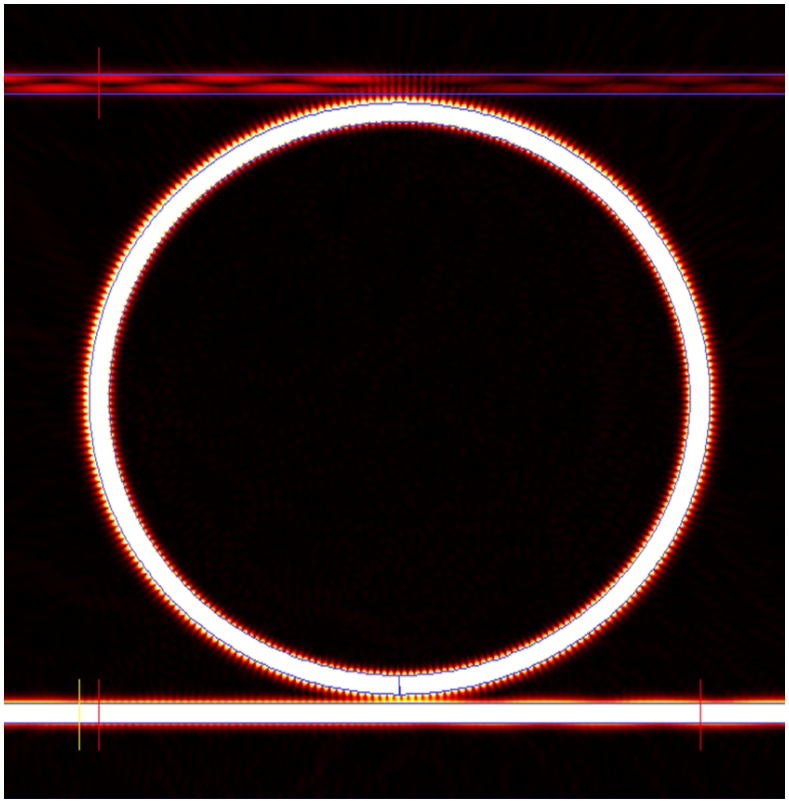

Figure 2.6: Simulation of a full ring resonator geometry in OMNISIM, near resonance. The amplitude of calculated H_y fields, shown here, are good for visually discerning ring absorption for TE modes.

2.1.5 Full Ring Simulation (OMNISIM)

Simulation of *just* the coupling regions of high-$\mathcal{Q}$ single-mode ring resonators provided to be a challenging task. When using FIMMPROP[2] to simulate the coupling regions that would correspond to high $\mathcal{Q}$-devices, more light appeared to be lost from the simulation than made it into the ring regions. Attempts at normalzing the results were attempted with the help of Photon-D support, but nothing sensible seemed to come out of it. More success was found using the software module OMNISIM to simulate full ring geometries. However, due to the scaling of computational complexity with the size of the rings[3],

[2]the propagation module integrated with FIMMWAVE's FDM solver

[3]From the manual: 10x change in geometry spacing will typically result in a 1,000x increase in memory use and a 10,000x increase in calculation time

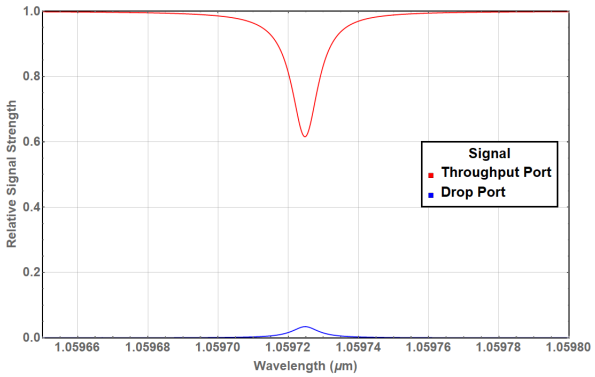

(a) After an FDTD simulation, OMNISIM allows for the sweeping of frequencies for drop and throughput ports

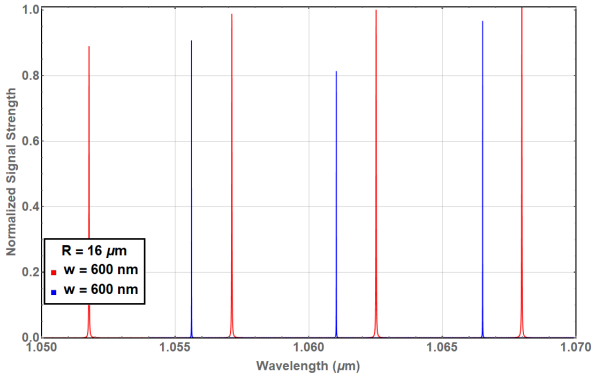

(b) Longer scans can be useful for determining the relative effect changes in parameter will have on the FSR.

Figure 2.7: Sample simulations obtained using OMNISIM, after an initial FDTD simulation of the geometry.

simulations were limited to smaller rings ($R < 20\,\mu\text{m}$).

OMNISIM utilizes a number of solvers for different uses. For the simulation of resonance behavior in optical rings, one must perform finite-difference time domain (FDTD) simulations. FDTD works by using a 'leapfrog' algorithm to alternately evolve the electric and magnetic field vectors using Maxwell's equations until convergence to a steady state solution. Using the FDTD solver, we are also able to obtain estimations of coupling $\mathcal{Q}$s of resonances, as well the free-spectral ranges. As shown in Fig. 2.7a, we are able to detect resonances at either the throughput port or the drop ports.

The primary goal of using the software was to estimate the expected coupling $\mathcal{Q}$ for our smaller ring resonators. The results from simulating 16 µm radius rings is shown on the next page. Based on these results, optical coupling distances in the range of 300–600 nm should suffice for characterization until measured $\mathcal{Q}_{opt}$ reach the 10^6 regime.

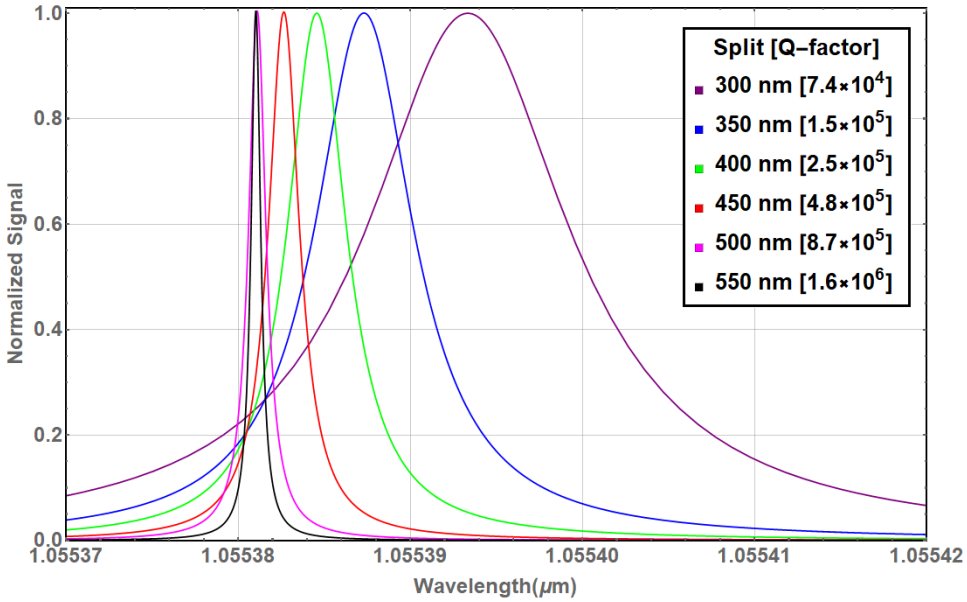

Figure 2.8: Results demonstrating the effect of changing the coupling split on both the optical $\mathcal{Q}$ and resonance frequency. The latter is due to a change in the phase of the coupler. All simulations were for a ring of radius 16 µm, with a width of 800 nm. Data is plotted below.

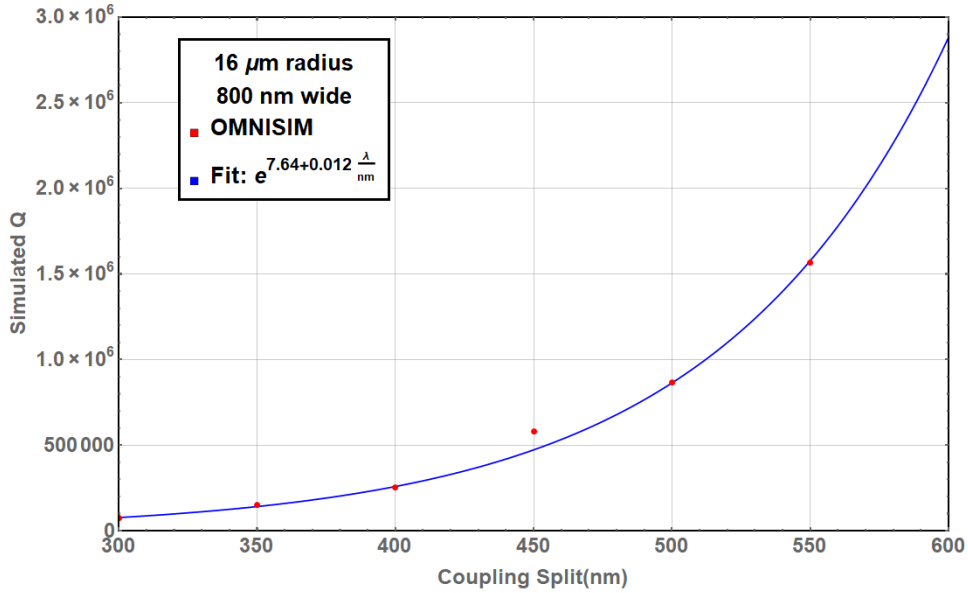

Figure 2.9: Plot of the simulated $\mathcal{Q}$ as a function of the separation between waveguide and ring resonator. The data matches the fit to an exponential very well, with the exception of the data point at 450 nm.

2.2 Mechanical Calculations and Simulations

Our goal is to realize a Si_3N_4 nanomechanical resonator within 100 nm of an optical ring resonator, using a combination of lithography and dry etching. However, such critical dimensions are not obtainable using stepper lithography, and would be far too expensive to implement on full wafer scale using electron-beam lithography. Even then, EBL would still be unable to obtain critical dimensions below 50 nm, and loading issues during the dry etching process would likely yield distorted geometries. Instead, we fabricate deformed 'snap-release' nanobeams that swerve around the ring resonators. Initially, these nanobeams are approximately 500 nm from the ring resonators at the point of closest approach. When the nanobeams are released by using vapor HF to remove the SiO_2, the tensile stress in the material causes the nanobeam to straighten and 'snap' toward the optical ring resonator, ideally reaching a new equilibrium position at close proximity to the outer edge of the ring waveguide.

In this section, we cover the modeling and simulation of 'snap-release' nanobeams. First, we discuss the underlying physics behind rectangular nanomechanical resonators, with emphasis on the effects of tensile stress in the material. Next, we predict the effects of the 'snap-release' mechanism, and compare the results to FEM simulations obtained using COMSOL Multiphysics. Finally, we look at the predicted sources of loss to predict the quality factors of the nanomechanical resonance.

2.2.1 Properties of Si_3N_4 Nanobeams with Tensile Stress

The physics of doubly-clamped beams is well explained through Euler-Bernouli beam theory, which is considered valid when the beam width is small with respect to the wavelengths of the modes being considered.[4] The governing differential equation for 1D oscillation of a long/thin beam of uniform cross section is given by:

$$EI\frac{\partial^4}{\partial x^4}z(x,t) - \sigma A\frac{\partial^2}{\partial x^2}z(x,t) + \rho A\frac{\partial^2}{\partial t^2}z(x,t) = 0 \tag{2.1}$$

where E, ρ, and σ are the Young's Modulus, density, and tensile stress of the nanobeam material, and A and I are cross-sectional area and cross-sectional inertia of the nanobeam geometry. Reported literature values for the Young's Modulus E of LPCVD Si_3N_4 span the range 160-380 GPa, depending on the conditions of the deposition [23, 24, 25, 26, 27, 28]. The value of 280 GPa is chosen for calculations, as an average from the most relatable sources [26, 27]. A density value of $\rho = 3184\,\mathrm{kg/m^3}$ is initially assumed [25], though deviation is possible due to potential variance in hydrogen content in the films from the source material.

If we assume an oscillatory function of the form $z(x,t) = u(x)\exp(i\omega t)$ and any force is time independent, we get:

$$EI\frac{\partial^4}{\partial x^4}u(x) - \sigma A\frac{\partial^2}{\partial x^2}u(x) - \rho A\,\omega^2\,u(x) = 0 \tag{2.2}$$

[4] When the beam width and mode wavelength are on the same order, Timshenko beam theory should be used.

2.2.1.1 General Solution to Euler-Bernouli Equation

The general solution to Eq. 2.2, for a characteristic length L, is given by:[5]

$$u_j(x) = \frac{1}{K_j}\left[A_j \sin\left(\alpha_j \frac{x}{L}\right) + B_j \cos\left(\alpha_j \frac{x}{L}\right) + C_j \sinh\left(\beta_j \frac{x}{L}\right) + D_j \cosh\left(\beta_j \frac{x}{L}\right)\right] \quad (2.3)$$

$$\alpha_j = \frac{L}{\sqrt{2}}\left(\frac{\sigma A}{EI}\right)^{1/2}\left[\left(1 + \frac{4\rho E \omega_j^2}{\sigma^2}\frac{I}{A}\right)^{1/2} - 1\right]^{1/2} \quad (2.4)$$

$$\beta_j = \frac{L}{\sqrt{2}}\left(\frac{\sigma A}{EI}\right)^{1/2}\left[\left(1 + \frac{4\rho E \omega_j^2}{\sigma^2}\frac{I}{A}\right)^{1/2} + 1\right]^{1/2} \quad (2.5)$$

where K_j is chosen such that $u_i(x)$ has a maximum value of 1. The choice to normalize $u_i(x)$ in such a manner is related to equipartition theory [29]. The boundary conditions for a doubly-clamped beam is are $u(x) = 0$ and $\frac{\partial}{\partial x}u(x) = 0$ at $x = 0$ and $x = L$. Imposing these on the general solution:

1. Setting $u(0) = 0$ leads directly to $B_j = -D_j$.

2. Setting $\frac{\partial}{\partial x}u(x) = 0$ at $x = 0$ leads to $\alpha_j A_j + \beta_j C_j = 0$.

3. Setting $u(L) = 0$ then leads to:

$$D_j\big[\cosh(\beta_j) - \cos(\alpha_j)\big] = -C_j\big[\sinh(\beta_j) - \frac{\beta_j}{\alpha_j}\sin(\alpha_j)\big] \quad (2.6)$$

4. With the final condition, $\frac{\partial}{\partial x}u(x) = 0$ at $x = L$, we get:

$$C_j\big[\cosh(\beta_j) - \cos(\alpha_j)\big] = -D_j\big[\frac{\beta_j}{\alpha_j}\sinh(\beta_j) + \sin(\alpha_j)\big] \quad (2.7)$$

[5]Source: Mathematica, with some artistic freedom added

Since we still have the normalization factor K_j to take care of the overall scaling, Eq. 2.6 can be used to set C_j and D_j. This gives us the overall solution

$$u_j(x) = \frac{1}{K_j}\left(C_j\left[\frac{\beta_j}{\alpha_j}\sin\left(\alpha_j\frac{x}{L}\right) - \sinh\left(\beta_j\frac{x}{L}\right)\right] + D_j\left[\cosh\left(\beta_j\frac{x}{L}\right) - \cos\left(\alpha_j\frac{x}{L}\right)\right]\right) \tag{2.8}$$

$$C_j = \cosh(\beta_j) - \cos(\alpha_j) \tag{2.9}$$

$$D_j = \sinh(\beta_j) - \frac{\beta_j}{\alpha_j}\sin(\alpha_j) \tag{2.10}$$

From the last boundary condition we now get:

$$2(1 - \cos(\alpha_j)\cosh(\beta_j)) = \frac{\alpha_j^2 - \beta_j^2}{\alpha_j\beta_j}\sin(\alpha_j)\sinh(\beta_j) \tag{2.11}$$

which simplifies to

$$\cos(\alpha_j)\cosh(\beta_j) - 1 = \left(\frac{\sigma^2}{4\rho E\omega_j^2}\frac{A}{I}\right)^{1/2}\sin(\alpha_j)\sinh(\beta_j) \tag{2.12}$$

which is a transcendental equation that can be solved for α_j, noting that

$$\beta_j^2 = \alpha_j^2 + L^2\left(\frac{\sigma A}{EI}\right) \tag{2.13}$$

Solving for ω_j gives the eigenfrequencies of each mode:

$$f_j = \frac{\omega_j}{2\pi} = \frac{\alpha_j^2}{2\pi L^2}\left[\frac{EI}{\rho A}\left(1 + \frac{L^2\sigma A}{\alpha_j^2 EI}\right)\right]^{1/2} \tag{2.14}$$

Both Eq. 2.2 and Eq. 2.14 have two different limits. However, the frequency equation reveals that the separation between these limits is dependent upon the mode parameter α_j. When the mode parameter $\alpha_j \sim \frac{w}{L}\sqrt{\frac{E}{\sigma}}$ one loses the ability to separate out these

regimes for even high-stress materials. Nevertheless, we are predominantly interested in low mode numbers, so for now we assume α_j to be on the order of unity. As such, we are able to isolate the two limits as such:

- **Low-Stress Limit** $\left[\frac{w}{L} \gg \sqrt{\frac{E}{\sigma}}\right]$**:** When the nanobeam width to length ratio is sufficiently large with respect to the tensile stress, the physics matches that of a rigid beam.
- **High-Stress Limit** $\left[\frac{L}{w} \gg \sqrt{\frac{E}{\sigma}}\right]$**:** When the bar is sufficiently long enough and stress is high enough, the physics matches that of a 1-D nanostring with stress σ.

Let us now examine these two regimes a bit more closely:

2.2.1.2 Low-Stress Solutions

In the low-stress limit ($\sigma \to 0$), the solution reduces to:

$$u_j(x) = \frac{1}{K_j}\left(A_j\left[\cosh\left(\alpha_j\frac{x}{L}\right) - \cos\left(\alpha_j\frac{x}{L}\right)\right] - B_j\left[\sinh\left(\alpha_j\frac{x}{L}\right) - \sin\left(\alpha_j\frac{x}{L}\right)\right]\right) \quad (2.15)$$

$$A_j = \sinh(\alpha_j) - \sin(\alpha_j) \quad (2.16)$$

$$B_j = \cosh(\alpha_j) - \cos(\alpha_j) \quad (2.17)$$

The frequency of the j^{th} mode is given by:

$$f_{j,LS} = \frac{\alpha_j^2}{2\pi L^2}\left(\frac{EI}{\rho A}\right)^{1/2} \quad (2.18)$$

Each unitless mode parameter α_j is the j^{th} root of the transcendental equation:

$$\cos(\alpha_j)\cosh(\alpha_j) - 1 = 0 \quad (2.19)$$

whose values are give by Table 2.1. As can be seen, the values of α_j are well approximated by $\pi(j + \frac{1}{2})$.

Table 2.1: Values of α_j for low-stress, doubly-clamped beams

index j	α_j	$\pi(i + \frac{1}{2})$
1	4.7300	4.7124
2	7.8532	7.8540
3	10.9956	10.9956
4	14.1372	14.1372

The fundamental mode is shown in Fig. 2.10, which compares it to the typical sinusoidal mode shape associated with strings and high-stress nanobeams.

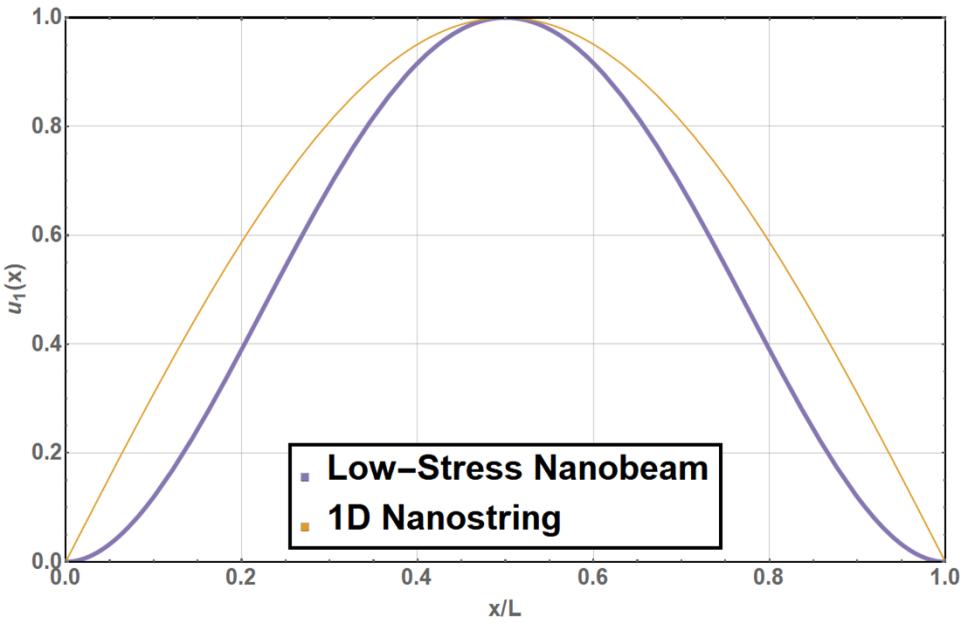

Figure 2.10: Comparison between fundamental mode shapes of low-stress nanobeams and nanostrings.

2.2.1.3 High-Stress Solutions

Let us now consider a nanobeam under high stress. The eigenfrequencies ω_j are approximated by:

$$\omega_{j,HS} = \frac{\alpha_j}{L}\left(\frac{\sigma}{\rho}\right)^{1/2} \tag{2.20}$$

which allows our transcendental function to simplify to:

$$\cos(\alpha_j)\cosh(\beta_j) - 1 = \left(\frac{\sigma A}{EI}\frac{L^2}{4\alpha_j^2}\right)^{1/2}\sin(\alpha_j)\sinh(\beta_j) \tag{2.21}$$

By defining the length scale:

$$L_s = \sqrt{\frac{EI}{\sigma A}} \tag{2.22}$$

we can write this equation as:

$$\cos(\alpha_j)\cosh(\beta_j) - 1 = \frac{L}{2\alpha_j L_s}\sin(\alpha_j)\sinh(\beta_j) \tag{2.23}$$

The physical significance of L_s will be clear shortly.

By looking at Eq. 2.13 and knowing that $\alpha_j \sim j\pi$, β_j will be large, and $\sinh(\beta_j)$ and $\cosh(\beta_j)$ will both be exponentially large and converge to the same value.[6] This leads to a 'selection' of the terms they are attached to (all other terms become negligible):

$$\cos(\alpha_j) = \frac{L}{2\alpha_j L_s}\sin(\alpha_j) \tag{2.24}$$

$$\rightarrow \tan(\alpha_j) = 2\alpha_j\frac{L_s}{L} \tag{2.25}$$

Seeing that the roots are going to be slightly larger than π, we expand out the tangent

[6]For typical values of nanobeams, we find $\beta_j \sim 50$, meaning the $\sinh(\beta_j)$ and $\cosh(\beta_j)$ are on the order of $e^2 5$.

to first order:

$$\alpha_j - j\pi = 2\alpha_j \frac{L_s}{L} \tag{2.26}$$

which allows us to solve for the first order correction to α_j in the high-stress limit:

$$\alpha_j = \frac{j\pi}{1 - 2\frac{L_s}{L}} \tag{2.27}$$

For a rectangular nanobeam, $I = \frac{1}{12}Aw^2$, giving:

$$L_s = w\sqrt{\frac{E}{12\sigma}} \tag{2.28}$$

which yields:

$$\alpha_j = j\pi\left[1 - \left(\frac{w}{L}\right)\sqrt{\frac{E}{3\,\sigma}}\right]^{-1} \tag{2.29}$$

and leads to the corrected high-stress eigenfrequencies:

$$f_j = \frac{j}{2L}\left(\frac{\sigma}{\rho}\right)^{1/2}\left[1 - \left(\frac{w}{L}\right)\sqrt{\frac{E}{3\,\sigma}}\right]^{-1} \tag{2.30}$$

This first-order correction can be ignored when $L \gg 2L_s$. For $E = 280$ GPa and $\sigma = 1140$ MPa, this corresponds to approximately to $L \gg 10w$. Since our nanobeams are on the order of 100 nm wide and 20 µm long, we cannot.

To figure out the physical significance of L_s, we simply need to look at the corresponding u_j and frequencies. As discussed before, the ratio β_j/α_j is going to be large. As such, the $\sin(\alpha_j \frac{x}{L})$ term will determine the overall form, with the remaining terms there basically to ensure the boundary conditions are satisfied and preserve symmetry.

This leads to:[7]

$$u_{j,HS}(x) \sim \sin\left(\alpha_j \frac{x}{L}\right) \tag{2.31}$$

$$\sim \sin(j\pi \frac{x - L_s}{L - 2L_s}) \tag{2.32}$$

with the frequencies:

$$f_{j,HS} = \frac{\omega_{j,HS}}{2\pi} = \frac{j}{2(L - 2L_s)} \left(\frac{\sigma}{\rho}\right)^{1/2} \tag{2.33}$$

which are both the profile and frequencies for a 1-D nanostring whose length is given by $L - 2L_s$.

The origin of this effective reduction in length can be traced back to the application of clamped boundary conditions, $\frac{\partial}{\partial x} u(x) = 0$ at $x = 0$ and $x = L$. Without these conditions the material would form a kink at the boundary, which is unphysical. That being said, it is unwise to take this interpretation too far and attempt to say that the nanobeam can be modeled in such a manner. It is merely that the high-energy, oscillatory behavior is restricted to the length $L - 2L_s$, which is what determines the shape and frequency. As will be discussed later in Section 2.2.2.1, it is bending near the clamping region that determines damping characteristics of standard-geometry rectangular nanomechanical resonators.

Interestingly enough, this value can be obtained almost straight from Eq. 2.2 using a physical argument. By normalizing our position coordinates to the length of the beam through $\tilde{x} = \frac{x}{L}$, we get:

$$\frac{EI}{L^4} \frac{\partial^4}{\partial \tilde{x}^4} u(\tilde{x}) - \frac{\sigma A}{L^2} \frac{\partial^2}{\partial \tilde{x}^2} u(\tilde{x}) - \rho A \, \omega^2 \, u(\tilde{x}) = F(\tilde{x}) \tag{2.34}$$

[7] If you notice, we shift over the sin function by L_s. This shift inherently comes from the small amplitude $\cos(\alpha_j \frac{x}{L})$ term, which we are reducing down to a phase shift.

Examining the first two terms, we see that $\frac{EI}{L^4} > \frac{\sigma A}{L^2}$ is when the system dynamics are going to be determined by the first term, which corresponds to the rigidity of the material. That is, the system must appear locally rigid over the length scales

$$L_s = \sqrt{\frac{EI}{\sigma A}} \tag{2.35}$$

Thus, considering the clamped boundary condition, the nanobeam cannot 'kink' over a shorter length scale than L_s. The rigidity of the boundary condition protrudes a distance L_s before the material is able to contribute to the oscilliatory dynamics.

Fig. 2.11 shows the calculated mode profiles obtained with and without the correction, in comparison to FEM simulation results obtained using COMSOL (covered in Section 2.2.1.5). In Section 2.2.1.5, further simulations will be performed as a function of stress, and the results will be shown to be in strong agreement with the fundamental mode. For higher order modes, the agreement starts to deviate as the effective L_s appears to increase, perhaps suggesting that the material has a higher impedence of sorts to high frequency motion.

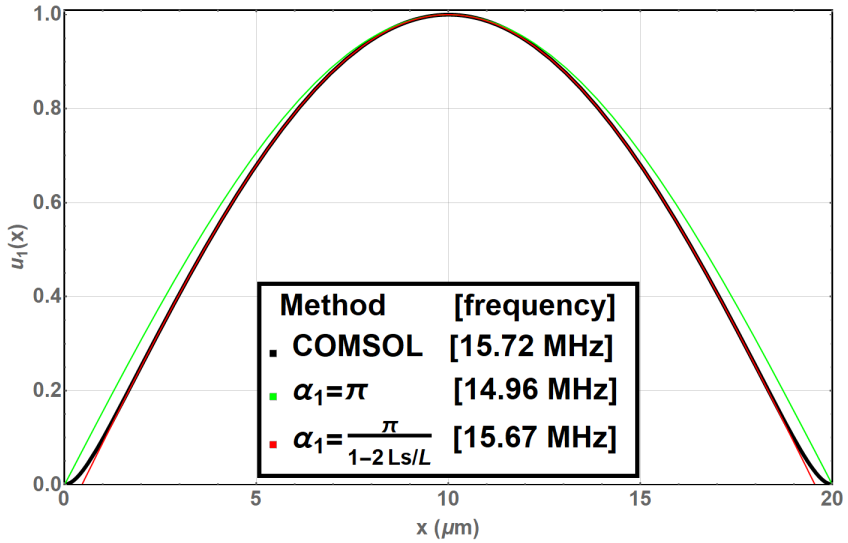

Figure 2.11: FEM simulations compared to the standard 1D nanostring approximation and the first-order corrected equations.

Dimensions
$L = 20\,\mu m$
$w = 100\,nm$
$h = 400\,nm$
$\sigma = 1140$

As for the 'rigid' behavior observed near the clamping points, we can perform similar asymptotic analysis to obtain analytic solutions near the end points. First, we note that from Eq. 2.13, we can approximate:

$$\beta_j \approx \frac{L}{L_s} \tag{2.36}$$

Now, by singling out the terms of the general solution that are attached to a $\cosh(\beta_j)$ or $\sinh(\beta_j)$, we get:

$$u_j(x)_{clamp} = \sin\left(\alpha_j \frac{x - L_s}{L}\right) + \alpha_j \frac{L}{L_s} \exp\left(-\frac{x}{L_s}\right) \tag{2.37}$$

$$\approx \alpha_j \frac{L_s}{L}\left[\frac{x - L_s}{L_s} + \exp\left(-\frac{x}{L_s}\right)\right] \tag{2.38}$$

which strongly agrees with FEM simulations for the fundamental mode, as seen in Fig. 2.12. The two results are also compared to the model of Schmid et al. (2011)[30], a highly cited manuscript which models the clamping region as a cantilever under a load determined by the tensile stress. Although this model probably demonstrates stronger

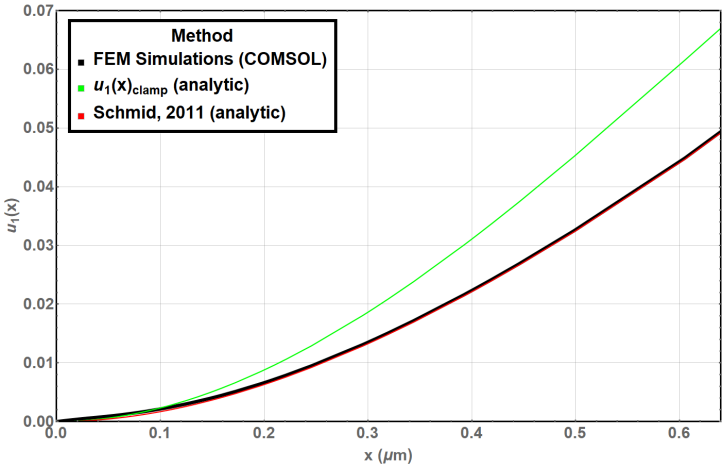

Figure 2.12: Comparison of mode shapes obtained for clamping regions using FEM simulations and analytic models.

agreement for $L_s \ll L$ (for which the model is designed), here we see the FEM simulations diverge significantly for our expected geometries. These models will be more strongly compared in Section 2.2.2.1.

Following the form of Eq. 2.37, we can encompass both clamping regions and the central sinusoidal form with the general solution:

$$u_j(x) = \sin\Big(\alpha_j \frac{x - L_s}{L}\Big) + \alpha_j \frac{L_s}{L}\Big(\exp(-\frac{x}{L_s}) + \exp(-\frac{L-x}{L_s})\Big) \tag{2.39}$$

A comparison of this solution for $j = 1$ and and FEM simulations are presented on the next page, in Figs. 2.13 and 2.14.

Using the first-order corrected α_j allows us to write the full general solutions for the frequency and mode shape conveniently:

The first-order corrected, high-stress solutions for a nanomechanical resonator of cross-sectional area A and cross-sectional inertia I, and material properties of Young's Modulus E, density ρ, and tensile stress σ, can be written in terms of the length of the nanomechanical L and the length scale:

$$L_s = \sqrt{\frac{EI}{\sigma A}} \tag{2.22}$$

The normalized mode shapes u_j are given by:

$$u_j(x) = \sin\Big(j\pi \frac{x - L_s}{L - 2L_s}\Big) + j\pi \frac{L_s}{L - 2L_s}\Big[\exp\big(-\frac{x}{L_s}\big) + \exp\big(-\frac{L-x}{L_s}\big)\Big] \tag{2.40}$$

with eigenfrequencies:

$$f_j = \frac{j}{2(L - 2L_s)}\Big(\frac{\sigma}{\rho}\Big)^{1/2} \tag{2.41}$$

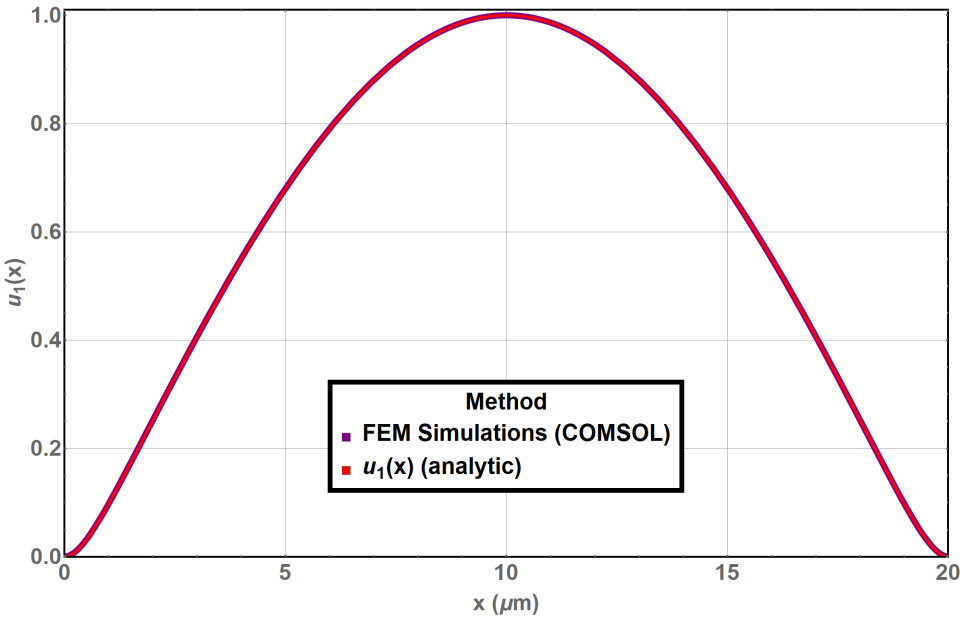

Figure 2.13: Comparison between FEM simulations and the first-order corrected eigenmode given by Eq. 2.40. See Fig. 2.14 below for residual plot.

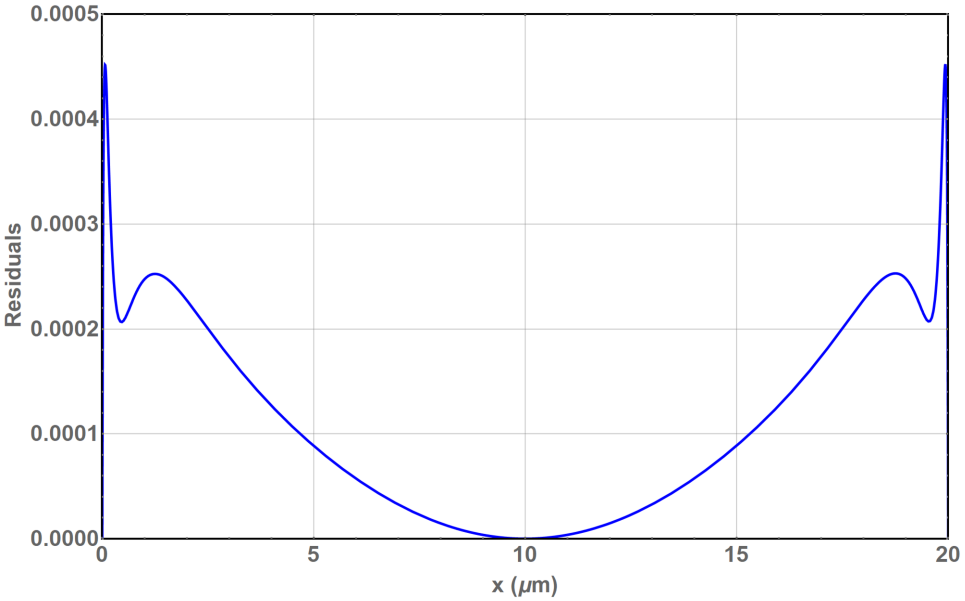

Figure 2.14: Residual Plot for Fig. 2.13. We see that the analytic equation agrees within 0.05% everywhere along the graph, maxmimally near the clamping region. The simulations appeared to produce a small, yet non-zero, slope at the clamping point.

2.2.1.4 Tensile Stress in LPCVD Si_3N_4 'Snap-Release' Nanobeams

Tensile stress in the LPCVD Si_3N_4 layer is a result of the differences in the coefficients of thermal expansion (α) between the Si_3N_4 and the Si substrate. LPCVD Si_3N_4 is typically deposited at temperatures in excess of 800 °C. When the wafer cools, the Si_3N_4 layer attempts to contract by $\alpha_{Si_3N_4} = 3.4\ \frac{\mu m}{m}$ per K[31]. However, it is unable to do so since the 500 µm Si substrate ultimately determines the contraction distance, with its $\alpha_{Si} = 2.69\ \frac{\mu m}{m}$ per K[32]. It is only when SiO_2 is removed by an undercutting process that the Si_3N_4 is free to contract.

When a straight nanobeam of length l is released, the Si_3N_4 material will desire to contract by an amount δl, but will not be able to physically do so since it is still anchored at its endpoints. Instead, the resulting strain $\frac{\delta l}{l}$ results in a stress σ give by:

$$\sigma = E\frac{\delta l}{l} \tag{2.42}$$

where E is Young's Modulus of the material. Our 400 nm LPCVD Si_3N_4 is provided by Rogue Valley Microdevices (RVM), which has internally characterized the stress to be approximately 1140 ± 15 MPa (personal communications). This corresponds to a strain of $\frac{\delta l}{l} = \frac{1140\ \text{MPa}}{280\ \text{GPa}} \approx 0.0041$, or about 1 in 250.

The high strain of LPCVD Si_3N_4 is vital in its ability to obtain high-quality nanomechanical resonators. However, we propose that we can sacrifice a fraction of this strain to create an optomechanical interaction strong enough to more than justify the expected change in mechanical quality factors. This is the subject of the remainder of this chapter.

Let us now consider the design of our 'snap-release' nanobeams, and examine how the change in shape impacts the final stress of the released nanobeam. Consider an unreleased Si_3N_4 nanobeam constructed from 4 circle arcs of equal length and radius of curvature R_{curv}, connected in the following way:

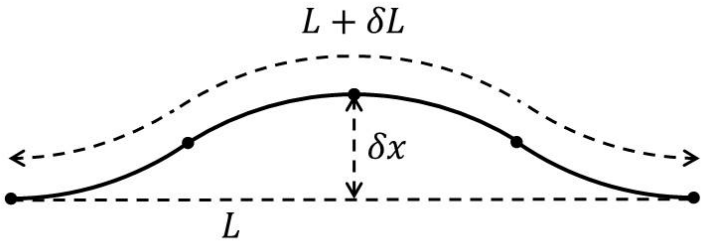

such that the endpoint to endpoint distance of the nanobeam is L, but the total length of the curved structure is $L+\delta L$, and the center of the beam is displaced by a small distance δx. When the SiO_2 is removed, the nanobeam material will contract. If the initial tensile stress is strong enough, the material should contract sufficiently into a straight nanobeam of length L, still fixed by the same two endpoints. It's stress should be reduced by some amount determined by the initial deformation.

Fig. 2.15 explodes the geometry of such a release. Adding the radius of curvature R_{curv} to the schematic allows for us to solve for δL as a function of the other parameters.

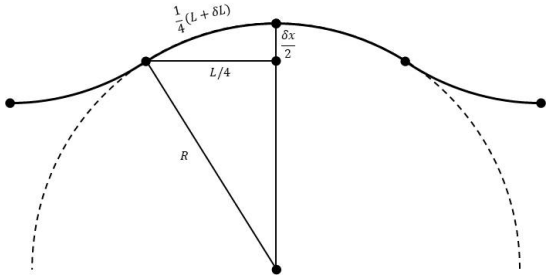

Figure 2.15: Geometric breakdown of the release of a 'snap-release' nanobeam.

Using simple geometry, we obtain the equation:

$$\frac{1}{4}(L+\delta L) = R_{curv}\arcsin\left(\frac{L/4}{R_{curv}}\right) \tag{2.43}$$

which allows us to solve for the change in strain:

$$\frac{\delta L}{L} = \left(\frac{L}{4R_{curv}}\right)^{-1}\arcsin\left(\frac{L}{4R_{curv}}\right) - 1 \tag{2.44}$$

where we notice a repetition of a characteristic term $\frac{L}{4R}$. Noting the right triangle geometry, we are able to solve for this characteristic parameter:

$$\frac{1}{4}L = \left(R_{curv}^2 - (R_{curv} - \frac{\delta x}{2})^2\right)^{1/2} \tag{2.45}$$

$$\rightarrow \frac{L}{4R_{curv}} = \left(\frac{\delta x}{R_{curv}} - \frac{1}{4}(\frac{\delta x}{R_{curv}})^2\right)^{1/2} \tag{2.46}$$

Plugging this into Eq. 2.44 gives us the less-than aesthetic equation:

$$\frac{\delta L}{L} = \left(\frac{\delta x}{R} - \frac{1}{4}(\frac{\delta x}{R})^2\right)^{-1/2}\arcsin\left(\left(\frac{\delta x}{R_{curv}} - \frac{1}{4}(\frac{\delta x}{R_{curv}})^2\right)^{1/2}\right) - 1 \tag{2.47}$$

However, a Taylor expansion around the small parameter $\frac{\delta x}{R_{curv}}$ leads to a significant simplification:

$$\frac{\delta L}{L} \approx \frac{1}{6}\frac{\delta x}{R_{curv}} + \frac{1}{30}\left(\frac{\delta x}{R_{curv}}\right)^2 + H.O.T. \tag{2.48}$$

Considering that $\frac{\delta x}{R_{curv}} \sim 0.01$, we comfortably ignore even the 2nd order term. Thus, the change in stress due to the release is:

$$\Delta\sigma = E\frac{\delta L}{L} = -\frac{1}{6}\frac{\delta x}{R_{curv}}E \tag{2.49}$$

The resulting stress of the 'snap release' nanobeam is give by:

$$\sigma_{SR} \approx \sigma_0 - \frac{1}{6}\frac{\delta x}{R_{curv}}E \tag{2.50}$$

If we now consider this stress-release beam to be a segment of length L_{SR} in a greater nanobeam of total length L:: then using the simple $\frac{\delta L}{L} = \frac{\delta L}{L_s}\frac{L_s}{L}$ gives us

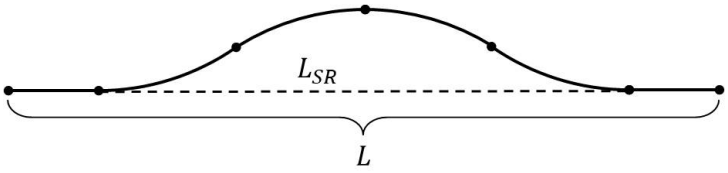

$$\Delta\sigma = \frac{1}{6}E\frac{\delta x}{R_{curv}}\frac{L_{SR}}{L} \tag{2.51}$$

The value of L_s in terms of the geometric release parameters is:

$$\begin{aligned} L_{SR} &= 4\left(R_{curv}^2 - \left(R_{curv} - \frac{\delta x}{2}\right)^2\right)^{1/2} && (2.52)\\ &= 4R_{curv}\left(1 - \left(1 - \frac{\delta x}{2R_{curv}}\right)^2\right)^{1/2} && (2.53)\\ &\approx 4\sqrt{R_{curv}\delta x} && (2.54) \end{aligned}$$

If we assume that enough stress remains that the nanobeam dynamics are still in the high-stress regime ($\sigma > 100$ MPa), the resulting frequency of the fundamental mode is:

$$f_1 = \frac{1}{2L}\left(\frac{\sigma - \Delta\sigma}{\rho}\right)^{1/2}\left[1 - \left(\frac{w}{L}\right)\sqrt{\frac{E}{3\left(\sigma - \Delta\sigma\right)}}\right]^{-1} \tag{2.55}$$

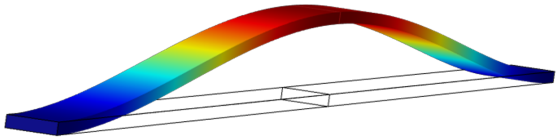

(a) Si3N4 Nanobeam with no internal tensile stress.

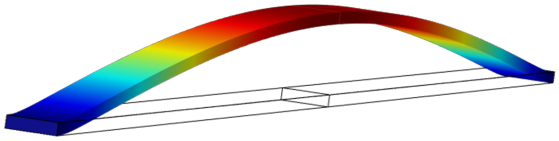

(b) Si_3N_4 Nanobeam with $\sigma = 1140$ MPa.

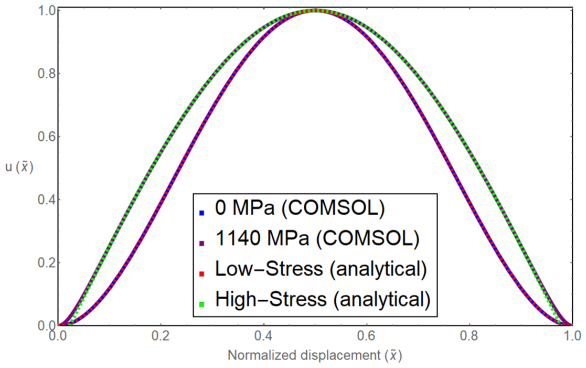

(c) Comparison of mode shapes obtained from COMSOL to Eqs. 2.15 and 2.32.

Figure 2.16: COMSOL simulations comparing the fundamental mode profiles of (a) zero-stress nanobeam to a (b) high-stress nanobeam. Dimensions for both are $w = 0.1\,\mu m$, $h = 0.4\,\mu m$, $L = 20\,\mu m$. In (c), the mode shapes are compared to the mode shape equations for low and high stress nanobeams.

2.2.1.5 Finite Element Method (FEM) Simulations in COMSOL

COMSOL Multiphysics is used to numerically simulate released Si_3N_4 nanobeams using Finite-Element Analysis (FEA). The Structural Mechanics Module allows us to input initial non-zero values for the 3-dimensional stress or strain tensors, σ_{ij} or ϵ_{ij}. Historically, our group has obtained results through use of the stress tensor, by setting $\sigma_{xx} = \sigma_{yy} = 1140$ MPa, and all off-diagonal terms and $\sigma_{zz} = 0$. This obtains similar results to working with ϵ_{ij}, but does not produce consistent results with derived equations. However, by setting $\epsilon_{xx} = \epsilon_{yy} = \frac{\sigma}{E}$, we obtain results within 1% of predictions made using the equations derived from Euler-Bernouli beam thoery. Implementing the strain directly, instead of the stress, is also more consistent with the physical interpretation of the system, and how we are modifying it.

To start, let us compare low and high stress nanobeams to predictions. Fig. 2.16 compares the fundamental modes between zero-stress and high-stress Si_3N_4 rectangular beams. We see that both low stress and high simulations agree strongly. As for the frequencies, COMSOL predicts a fundamental frequency of 2.4 MHZ for zero stress,

compared to 1.6 MHz obtained from Eq. 2.18. For $\epsilon_{xx} = \epsilon_{yy} = 1140$ MPa/280 GPa, the simulated frequency is 15.72 MHz, compared to 15.67 MHz from Eq. 2.30. So, despite the low-stress mode shape matching very well to the simulation, the calculated eigenfrequencies differ by $\sim 50\%$. The high-stress eigenfrequencies however agree reasonably well.

The 'snap-release' geometry is built parametrically in the COMSOL interface as a function of δx and R_{curv}, and covered with an 'extremely fine' mesh (Fig. 2.17a). The *Prestressed Analysis, Eigenfrequency* study is used to first determine the static equilibrium of the geometry, and then determine the eiqenfrequencies. Fig. 2.17b shows the 2nd eigenmode oscillating about the new equilibrium position. Additionally, we use:

$$\Delta\sigma = E\frac{\delta L}{L} = -\frac{1}{6}\frac{\delta x}{R_{curv}}E \tag{2.49}$$

to predict the amount of stress released, then simulate straight rectangular nanobeams with the new predicted stress. This is to determine whether COMSOL "agrees" that the stress in the SRNBs is quantitatively given by Eq. 2.49. The results are shown on the next page for simulations the first 3 modes of oscillation.

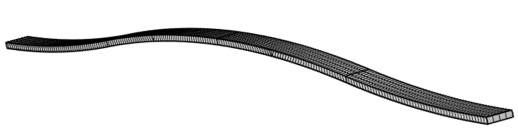

(a) Geometrical construction and meshing of SR nanobeam.

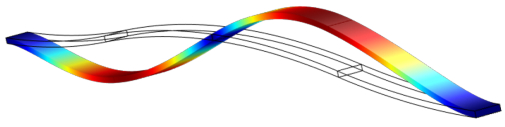

(b) 2nd eigenmode of SR nanobeam, demonstrating oscillation about flat nanobeam position.

Figure 2.17: Simulation setup and results of SR nanobeams using COMSOL.

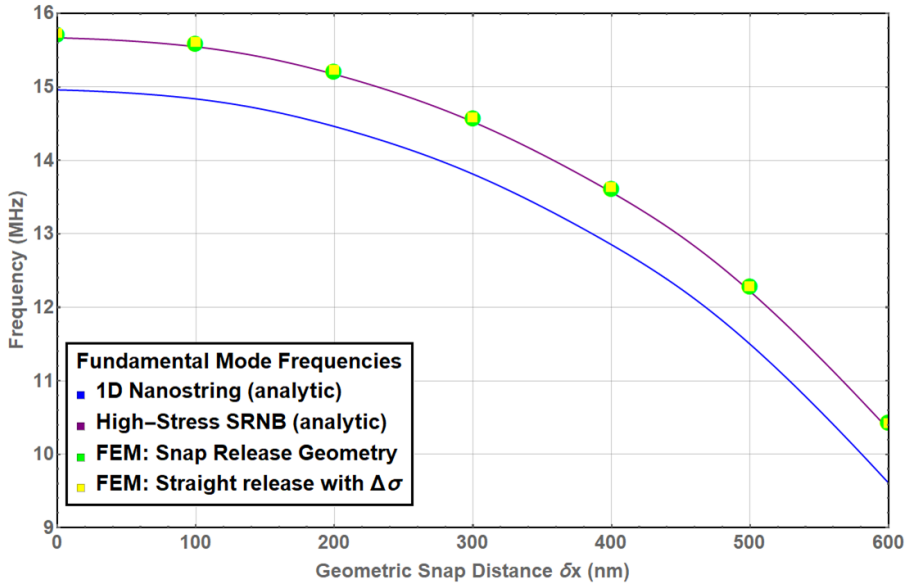

Figure 2.18: SRNB Simulations for the fundamental mode ($j = 1$).

In Fig. 2.18 above, very strong agreement is demonstrated between our analytic model (purple) and FEM simulations of both the 'snap-release' geometry (green) and the released-stress model (yellow). As can be seen in Figs. 2.19 and 2.20 on the next page, the agreement between our analytic equation for the frequency of an SRNB and the simulation results begins to deviate for higher order modes. Nevertheless, for both the $j = 2$ and $j = 3$ modes, COMSOL agrees in the evaluation that the stress released is given by Eq. 2.49, even when more than half of the stress has been released.

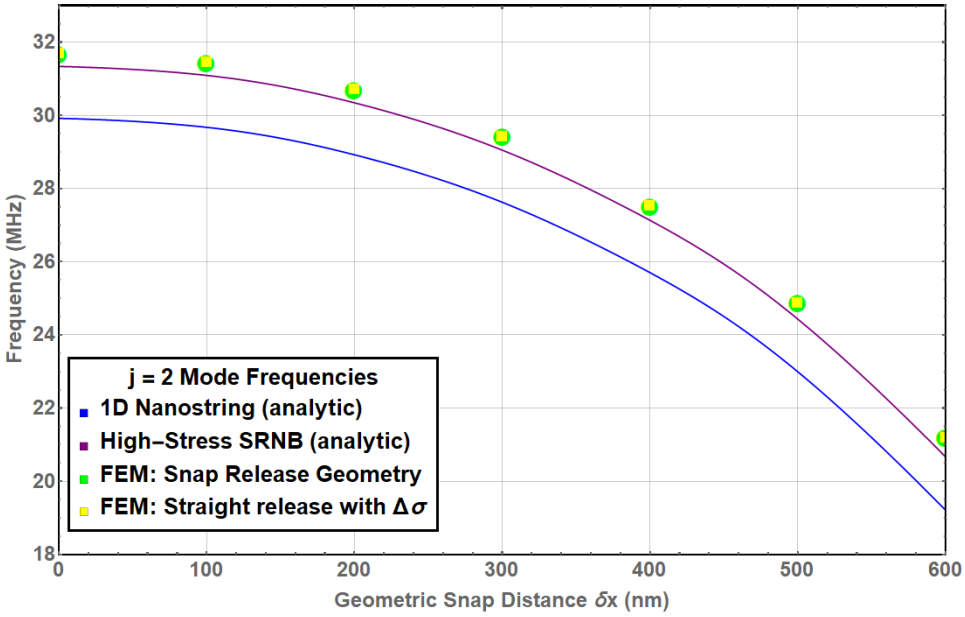

Figure 2.19: SRNB Simulations for the 2nd mode ($j = 2$).

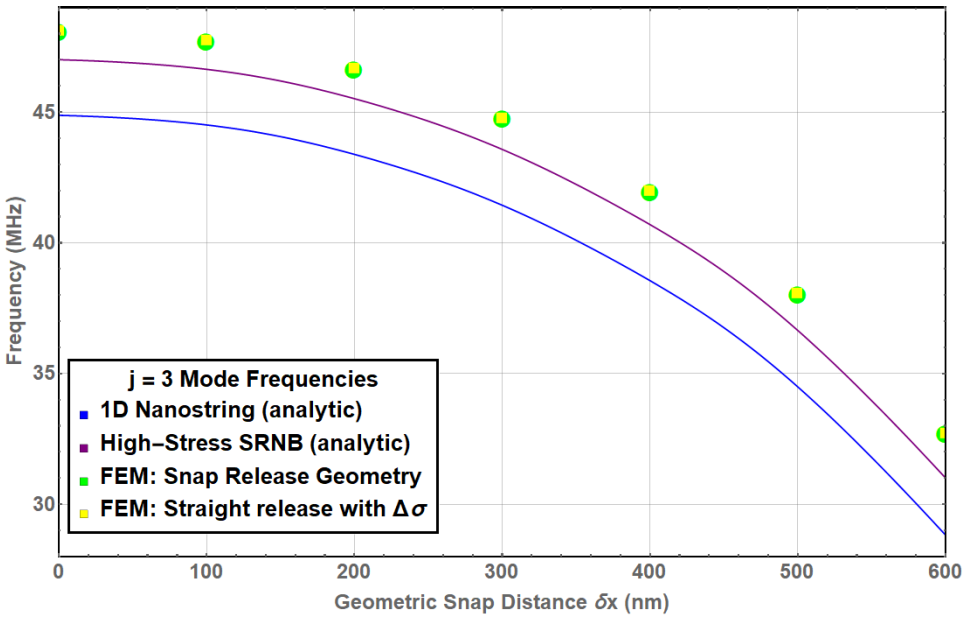

Figure 2.20: SRNB Simulations for the 3rd mode ($j = 3$).

2.2.1.6 Effective Mass

As the system exhibits oscillatory behavior, we wish to represent its modes as damped harmonic oscillators with spring constants k_j and effective masses m_j. This will allow us to relate the time-averaged motion of the device to its thermal energy in the next section. For a harmonic oscillator of volumetric mass m, the quantity $\frac{m_j}{m}$ is the average participation ratio of the mass of the j^{th} mode toward the behavior of the system as a harmonic oscillator. The formula for the effective mass is given by [29]:

$$m_j = \int dV \rho(x) |r_j(x)|^2 \tag{2.56}$$

where $r_j(x)$ is the normalized mode shape in 3 dimensions. In the case of an object with uniform density and cross sectional area, this simplifies to:

$$\begin{aligned} m_j &= \rho A \int_0^L dx |u_j(x)|^2 & (2.57) \\ &= \frac{m}{L} \int_0^L dx |u_j(x)|^2 & (2.58) \end{aligned}$$

With f_j and m_j determined, one is able to find the spring constant of the mode through the standard equation $2\pi f_j = \sqrt{k_j/m_j}$.

To check for self consistency of describing the physical behavior of the system as a harmonic oscillator, one can independently determine the spring constant k_j by calculating the deformation x_j of the beam shape under an applied force F_j to obtain $k_j = F_j/x_j$. Using this method, for a doubly-clamped nanobeam without any internal stress, one is able to find [29]:

$$k_1 = 192 \frac{EI}{L^3} \tag{2.59}$$

By comparing this to f_j using Eq. 2.18, one obtains the effective mass

$$\frac{m_1}{m} = \frac{k_1}{\omega_1^2} = \frac{192}{\alpha_1^4} \approx 0.384 \tag{2.60}$$

Hauer et al. (2013)[29] obtained values of $\frac{m_1}{m} = 0.39 \pm 0.01$ for a doubly-clamped beam using five different methods, including FEM simulations and integration of Eq. 2.15. Using the $u(x)$ for low-stress nanobeams shown in Fig. 2.16c, obtained using COMSOL simulations, we obtain a value of 0.396.

We are interested in the m_{eff} of our high-stress nanobeams to complete our model of our system as damped harmonic oscillators. For a purely sinusoidal function we would expect $\frac{m_1}{m} = 1\frac{1}{2}$. We would expect the high-stress value to be close to that, but slightly less do to the clamping regions.

We are able to directly calculate the effective mass through COMSOL using the full volume integral, without having to reduce our motion down to 1-dimension. After generating the nanobeam eigenmodes in COMSOL, we first normalize $r_i(x)$ so that its maximum value is 1. Then, COMSOL is able to perform a volume integral over the simulation space to get the effective mass. In the language of COMSOL, this is done by:

$$m_{eff} = \int dV \left[\frac{\texttt{solid.rho*(solid.disp)}^2}{\texttt{maxdisp}^2} \right] \tag{2.61}$$

where `maxdisp` is the determined maximum displacement of the mode. For the high-stress nanobeam, we obtain a value of $\frac{m_1}{m} = 0.484$, near the value of $\frac{1}{2}$ expected of a 1-D nanostring, but differing by enough relative to the low-stress value (0.396) to be non-negligible. Similarly, numerical integration of Eq. 2.58 using Eq. 2.40 yields $\frac{m_1}{m} = 0.478$.

2.2.1.7 Thermal Motion

With the effective mass determined, we are now able to consider the thermal motion of the nanobeam through full modeling of its behavior as that of a harmonic oscillator. The thermal properties of a quantum mechanical harmonic oscillator with frequency ω is explained with the standard phonon model. The total energy in a single mode with frequency ω_i is given by $E_n = (n+\frac{1}{2})\hbar\omega$, where n is the number of phonons in that mode. Since phonons are spin-0 particles, they are governed by Bose-Einstein statistics. At a temperature T, the probability of obtaining a phonon state of n phonons with is given by:

$$P(n) = \frac{\exp(-n\frac{\hbar\omega}{k_B T})}{1-\exp(-\frac{\hbar\omega}{k_B T})} \tag{2.62}$$

As such, the expected number of thermal phonons $n_{th,j}$ in the j^{th} mode of a Si_3N_4 nanobeam is:

$$n_{th,i} = \langle n \rangle = \sum_{n=0}^{\infty} nP(n) = \frac{1}{\exp\frac{\hbar\omega_i}{k_B T} - 1} \tag{2.63}$$

For $\omega_j = 2\pi \cdot 10$ MHz, when $T \gg 4.8$ mK we can simplify this to:

$$n_{th,j} \approx \frac{k_B T}{\hbar\omega_j} \tag{2.64}$$

To relate the number of thermal phonons n in the j^{th} mode to the physical amplitude of the oscillation δx_n, we simply set the classical energy of the harmonic oscillator equal to the quantum energy levels for n phonons. This gives us

$$\begin{aligned}
(\delta x_n)^2 &= 2(n+\frac{1}{2})\frac{\hbar\,\omega_j}{k_j} && (2.65)\\
&= 2(n+\frac{1}{2})\frac{\hbar}{m_{eff}\omega_j} && (2.66)\\
&= 4(n+\frac{1}{2})x_{zpf}^2 && (2.67)
\end{aligned}$$

where x_{zpf} is the zero-point fluctuation of the quantum harmonic oscillator. From here we can see x_{zpf} is the root-mean squared of the ground state amplitude $x_{zpf} = \frac{1}{\sqrt{2}}\delta x_0$. For large n, this reduces to:

$$\delta x_n = 2\sqrt{n_{th}}x_{zpf} = \frac{2}{\omega_i}\sqrt{\frac{k_B T}{m_{eff}}} \tag{2.68}$$

2.2.2 Damping Mechanisms

The dampening mechanisms for a nanomechanical resonator can be separated into two categories: internal and environmental. Environmental damping mechanisms dominate near atmospheric pressure, reducing mechanical $\mathcal{Q}$s to near unity, as discussed in Section 2.2.2.2. With proper isolation from the environment, internal damping mechanisms within the sample should be all that remain.

2.2.2.1 Mechanical Damping

The internal damping of high-stress Si_3N_4 nanomechanical resonators is well studied [33, 24, 30]. There are four main loss mechanisms that need to be considered for nanomechanical resonators [33]:

- Material damping: Energy is lost per cycle of oscillation due to intramaterial interactions initiated by deformation.
- Clamping loss: Coupling between the mechanical modes of the nanobeam and radiation modes of the surrounding material through the anchors leads to radiation of vibrational energy.
- Thermoelastic damping: Motion in the mechanical resonator leads to compression and expansion in the material. Compressed material becomes warmer and the stretched material becomes colder. Energy is lost from the system if the beam is able to significantly rethermalize within a period of oscillation.
- Surface loss: Defects on the surface of the resonator can modify the surface stress or cause lossy interactions with surface waves. [34]

Unterreithmeier et al. (2010) [24] determined that clamping loss and thermoelastic dampening and can be neglected for high-stress Si_3N_4 nanobeams, but were unable to distin-

guish between surface loss and material loss with their model. Schmid et al. (2011)[30] experimentally demonstrated that surface loss was not a limiting parameter by showing that internal $\mathcal{Q}$-factors were independent of width of the nanomechanical resonator.

Based on the above arguements, the expected mechanical quality factor $\mathcal{Q}_{mech}$ is approximated by [30]:

$$\mathcal{Q}_{mech} \approx 2\pi \frac{W_{tension} + W_{bending}}{\Delta W_{bending}} \tag{2.69}$$

where $W_{tension}$ is the stored elastic energy in the tension and ΔW_{deform} the energy lost per cycle due to material deformation. With the assumption that ΔW_{deform} is determined entirely by intrinsic material properties, a material specific quality factor for the deformation is defined by:

$$\mathcal{Q}_{mat} = 2\pi \frac{W_{deform}}{\Delta W_{deform}} \tag{2.70}$$

which allows us to write

$$\mathcal{Q}_{mech} = \frac{W_{tension}}{W_{deform}} \mathcal{Q}_{\mathrm{Si_3N_4}} \tag{2.71}$$

where $\mathcal{Q}_{\mathrm{Si_3N_4}} \approx 17000$ is the intrinsic material quality factor of Si_3N_4, determined by fit to experimental data [30]. This can be written as:

$$\mathcal{Q}_{mech} = \frac{\sigma A}{EI} \frac{\int_0^L [\frac{\partial}{\partial x} u(x)]^2 \, dx}{\int_0^L [\frac{\partial^2}{\partial x^2} u(x)]^2 \, dx} \mathcal{Q}_{\mathrm{Si_3N_4}} \tag{2.72}$$

where $u(x)$ is the normalized mode shape.

For analytical estimation of these integrals for 1D nanostrings, the model described in Schmid et al. (2011)[30] is very commonly used. Schmid matches the slope of the sinusoid to that of a cantilever under an effective point force determined by σ and the geometric parameters of the nanobeam. With this method, the local beam shape is estimated to

be[30]:

$$u(x) = \frac{n\pi}{L}\Big(\frac{x}{L_c}\Big)^2\Big(L_c - \frac{x}{3}\Big) \tag{2.73}$$

$$L_c = \sqrt{2\frac{EI}{\sigma A}} \tag{2.74}$$

For a rectangular nanobeam with cross-sectional inertia $I = \frac{1}{12}hw^3$, an analytical evaluation of the integrals in Eq. 2.72 for the fundamental mode leads to [30]:

$$\mathcal{Q}_{mech} = \left[\frac{\pi^2}{12}\frac{E}{\sigma}\Big(\frac{w}{L}\Big)^2 + \sqrt{\frac{32}{27}}\sqrt{\frac{E}{\sigma}}\frac{w}{L}\right]^{-1}\mathcal{Q}_{\mathrm{Si_3N_4}} \tag{2.75}$$

Alternatively, the mode shape $u(x)$ can be obtained from COMSOL, and the integrals in Eq. 2.72 evaluated numerically. If we normalize the mode shape to unit length through $\tilde{x} = \frac{x}{L}$ (to extract the dimensional dependence), Eq. 2.72 becomes:

$$\mathcal{Q}_{mech} = 12\frac{\sigma}{E}\Big(\frac{L}{w}\Big)^2\frac{\int_0^1 dz[\frac{\partial}{\partial z}v(z)]^2}{\int_0^1 \tilde{x}[\frac{\partial^2}{\partial \tilde{x}^2}u(\tilde{x})]^2}\mathcal{Q}_{\mathrm{Si_3N_4}} \tag{2.76}$$

To compare Eqs. 2.75 and 2.76, let us simulate a rectangular nanobeam with $L = 20\,\mu\mathrm{m}$, $w = 100\,\mathrm{nm}$, and $\sigma = 1140$ MPa. Evaluating the analytical result using Eq. 2.75 gives us:

$$\mathcal{Q}_{mech} = \left[\frac{\pi^2}{12}\frac{280\ \mathrm{GPa}}{1140\ \mathrm{MPa}}\Big(\frac{100\,\mathrm{nm}}{20\,\mu\mathrm{m}}\Big)^2 + \sqrt{\frac{32}{27}}\sqrt{\frac{280\ \mathrm{GPa}}{1140\ \mathrm{MPa}}}\frac{100\,\mathrm{nm}}{20\,\mu\mathrm{m}}\right]^{-1}\mathcal{Q}_{\mathrm{Si_3N_4}} \tag{2.77}$$

$$\approx 11.1 \cdot \mathcal{Q}_{\mathrm{Si_3N_4}} \tag{2.78}$$

$$\approx 190000 \tag{2.79}$$

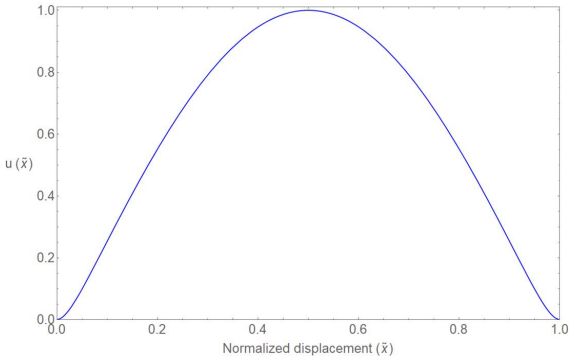

(a) Overall profile of $u_1(x)$

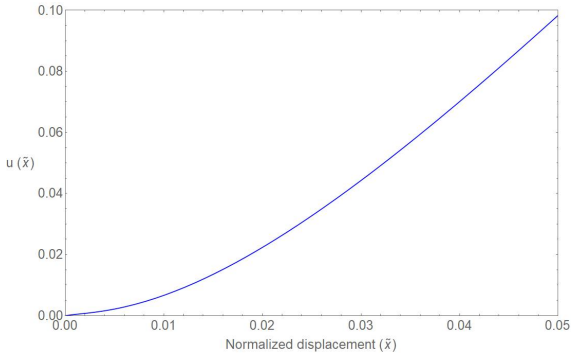

(b) The clamping regions of $u_1(x)$ determined by FEM analysis.

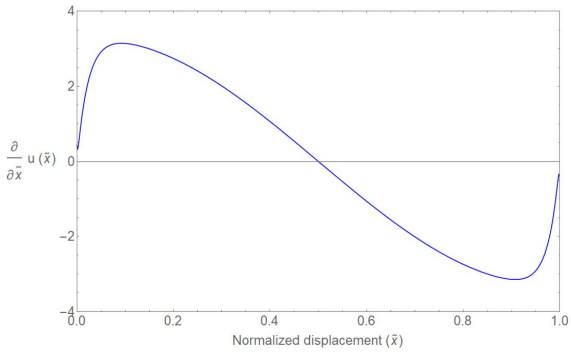

(c) Interpolated shape of $\frac{\partial}{\partial x}u_1(x)$

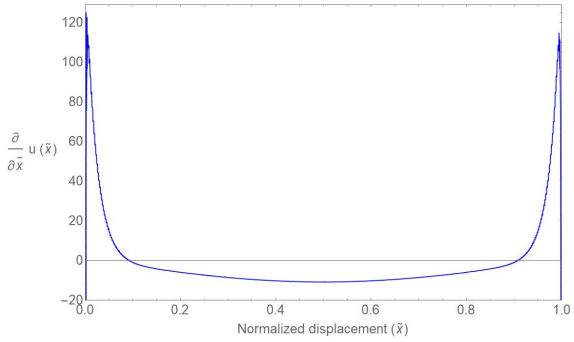

(d) Interpolated shape of $\frac{\partial^2}{\partial x^2}u_1(x)$

Figure 2.21: COMSOL evaluation of $u_1(x)$ and its derivatives. The derivatives are obtained using Mathematica's interpolation function.

The length-normalized beam shape $u(\tilde{x})$ is extracted from COMSOL for the given parameters. The results for $u(\tilde{x})$, $\frac{\partial}{\partial \tilde{x}}$, and $\frac{\partial^2}{\partial \tilde{x}^2}u(\tilde{x})$ are shown in Fig. 2.21. Evaluation of Eq. 2.76 using numerical integration of the results leads to:

$$\mathcal{Q}_{FEM} = 12\,\frac{1140\text{ MPa}}{280\text{ GPa}}\left(\frac{20\,\mu\text{m}}{100\,\text{nm}}\right)^2\frac{4.92246}{436.551}\mathcal{Q}_{Si_3N_4} \tag{2.80}$$

$$\approx 22.0\cdot\mathcal{Q}_{Si_3N_4} \tag{2.81}$$

$$\approx 370000 \tag{2.82}$$

which is nearly double the result obtained from the model. To figure out the discrepancy, let us see how our high-stress solutions compare to both the model and the FEM

simulations. Starting with the direct approach of taking our overall solution:

$$u_1(x) = \sin\Big(\pi\frac{x-L_s}{L-2L_s}\Big) + \pi\frac{L_s}{L-2L_s}\Big[\exp\big(-\frac{x}{L_s}\big) + \exp\big(-\frac{L-x}{L_s}\big)\Big] \tag{2.40}$$

and numerically integrating Eq. 2.72, which we choose to write in the form:

$$\mathcal{Q}_{mech} = \frac{1}{L_s^2}\frac{\int_0^L[\frac{\partial}{\partial x}u(x)]dx}{\int_0^L[\frac{\partial^2}{\partial x^2}u(x)]dx}\mathcal{Q}_{\mathrm{Si_3N_4}} \tag{2.83}$$

we end up with

$$\mathcal{Q}_{mech} \approx 18.00 \cdot \mathcal{Q}_{\mathrm{Si_3N_4}} \tag{2.84}$$

$$\approx 306000 \tag{2.85}$$

which is in between the results from the model and the simulated solutions. To gain more insight into why this is, we use the same method of breaking down the nanobeam into the clamped region and the free-oscillation region. Using the piece-wise equations derived in Section 2.2.1.3

$$u_j(x)_{clamp} = \alpha_j\frac{L_s}{L}\left[\frac{x-L_s}{L_s} + \exp\big(-\frac{x}{L_s}\big)\right] \tag{2.38}$$

$$u_j(x)_{str} = \sin(\alpha_j\frac{x-L_s}{L}) \tag{2.32}$$

we evaluate the integrals for energy stored in the deformation and tension. Noting the form of $\frac{\partial^2}{\partial x^2}u_1(x)$ demonstrated in Fig. 2.21d, the effects of the clamping region extend far beyond $\frac{L_s}{L} \approx 0.022$. To compensate for this, we extend the integral of our piecewise function out to infinity. Since it is of the form of decaying exponential, it will sufficiently

converge. The resulting energy integrals are thus:

$$W_{d,str} = \frac{1}{2}EI\int_{L_s}^{L-L_s} dx\left[\frac{\partial^2}{\partial x^2}u_j(x)_{str}\right]^2 \tag{2.86}$$

$$= \frac{1}{4}EI\left(\frac{\alpha_j}{L}\right)^4(L-2L_c) \tag{2.87}$$

$$W_{d,clamp} = \frac{1}{2}EI\int_{0}^{\infty} dx\left[\frac{\partial^2}{\partial x^2}u_j(x)_{clamp}\right]^2 \tag{2.88}$$

$$= \frac{1}{4}\frac{EI}{L_s}\left(\frac{\alpha_j}{L}\right)^2 \tag{2.89}$$

$$W_{tension} = \frac{1}{2}\sigma\int_{L_s}^{L-L_s} dx\left[\frac{\partial}{\partial x}u_j(x)_{str}\right]^2 \tag{2.90}$$

$$= \frac{1}{4}\sigma A\left(\frac{\alpha_j}{L}\right)^2(L-2L_c) \tag{2.91}$$

Evaluating Eq. 2.71 with these results give:

$$\mathcal{Q}_{mech} = \left[\frac{W_{d,str}}{W_{tension}} + 2\frac{W_{d,clamp}}{W_{tension}}\right]^{-1}\mathcal{Q}_{mat} \tag{2.92}$$

$$= \left[\frac{EI}{\sigma A}\left(\frac{\alpha_j}{L}\right)^2 + \frac{2}{L-2L_s}\sqrt{\frac{EI}{\sigma A}}\right]^{-1}\mathcal{Q}_{mat} \tag{2.93}$$

$$= \left[\alpha_j^2\left(\frac{L_s}{L}\right)^2 + 2\frac{L_s}{L-2L_s}\right]^{-1}\mathcal{Q}_{mat} \tag{2.94}$$

$$= \left[(j\pi)^2\left(\frac{L_s}{L-2L_s}\right)^2 + 2\frac{L_s}{L-2L_s}\right]^{-1}\mathcal{Q}_{mat} \tag{2.95}$$

Now, if we make the order of magnitude assumption that $L-2L_s \approx L$, and use assume

a rectangular cross section so $I = \frac{1}{12}Aw^2$, we get:

$$\mathcal{Q}_{mech} = \left[\frac{(j\pi)^2}{12}\frac{E}{\sigma}\left(\frac{w}{L-2L_s}\right)^2 + \frac{2}{\sqrt{12}}\frac{w}{L-2L_s}\sqrt{\frac{E}{\sigma}}\right]^{-1}\mathcal{Q}_{mat} \tag{2.96}$$

$$\approx \left[\frac{(j\pi)^2}{12}\frac{E}{\sigma}\left(\frac{w}{L}\right)^2 + \frac{1}{\sqrt{3}}\frac{w}{L}\sqrt{\frac{E}{\sigma}}\right]^{-1}\mathcal{Q}_{mat} \tag{2.97}$$

where we see that we have the same approximate form as Eq. 2.75, but we predict approximately half the energy dissipation from deformation in the clamping region, relative to the dissipation in the string component, when compared to the Schmid model. Evaluating Eq. 2.95 for $j = 1$ gives:

$$\mathcal{Q}_{mech} \approx 18.9 \cdot \mathcal{Q}_{\mathrm{Si_3N_4}} \tag{2.98}$$

$$\approx 320000 \tag{2.99}$$

which is close to our numerically integrated value. The deviation from COMSOL is likely due to the simulation behavior near the clamping region, best demonstrated by the graph of $\frac{\partial^2}{\partial x^2}u_1(x)$ in Fig. 2.21d. This function is seen to suddenly drop toward zero near the boundary, rather than increase exponentially upward. This leads to an underestimation of the bending energy stored in the clamping region, and thus an overestimation of the resulting quality factor.

To be clear, this should not outright be taken to mean that the quality factors should be larger. Considering the 'fit' parameter $\mathcal{Q}_{\mathrm{Si_3N_4}}$ associated with $\mathrm{Si_3N_4}$, the purpose of such models is to attribute relative losses correctly, and determine the scaling of each loss term. Our model suggests that energy dissipation in the oscillatory portion of the mode is double what the other model suggests (relative to the clamping region), but agrees with the assessment that this mode of dissipation should scale $\propto \left(\frac{L}{q}\right)^2$.

To remain consistent, we will choose Eq. 2.95 for analytic calculations for the remainder of the chapter, rather than the Schmid model. However, we necessarily need to adjust our $\mathcal{Q}_{Si_3N_4}$ for our new model to remain consistent with experimental observations. Since our model predicts approximately half the damping in the clamping region as the Schmid model, we need to reduce $\mathcal{Q}_{Si_3N_4}$ by a factor of 2 to compensate. With this final adjustment, the estimated intrinsic quality factor of the fundamental mode of our Si_3N_4 SRNBs is given by:

$$\mathcal{Q}_{mech} = \left[\pi^2\left(\frac{L_s}{L-2L_s}\right)^2 + 2\frac{L_s}{L-2L_s}\right]^{-1}\mathcal{Q}'_{Si_3N_4} \tag{2.100}$$

where $\mathcal{Q}'_{Si_3N_4} \approx 8500$ is the adjusted material quality factor for Si_3N_4.

2.2.2.2 Air Damping

The effect of air damping is an important point of consideration for the characterization of any MEMS device. In general, high-quality mechanical resonators suffer from a significant reduction in measured $\mathcal{Q}$-factors near atmospheric pressure. This is caused by there being a significant number of collisions between air molecules and the oscillator over a single period of oscillation. However, depending on the mean free path of the air molecules and the geometry of the resonator, different models are used to predict the depreciation in $\mathcal{Q}$-factor.

Here we introduce the Knudsen number K_n of the system, which is the ratio of the mean free path of air particles to the characteristic length of the device:

$$K_n = \frac{\ell_{FP}}{\lambda_{char}} \tag{2.101}$$

The value of K_n is used to estimate what interaction regime a mechanical system is in with respect to its environemtn [35, 36]:

- $K_n > 10$: *free-molecule regime*: The interaction of air molecules with each other can be ignored, and the air dampening effects are determined by collisions between the oscillator and the air molecules. The $\mathcal{Q}$ is expected to scale inversely with density of collisions, or equivalently inverse to the pressure.

- $0.01 < K_n$: *viscous regime*: The ability to ignore the interaction of air molecules with each other completely breaks down. Instead, the air must be treated as a viscous fluid. Since viscosity is independent of pressure, the $\mathcal{Q}$-factor must also be independent of pressure.

- $0.01 < K_n < 10$: *the transition regime*: Between the free-molecule and viscous fluid regimes, air molecules still dampen the oscillation through collisions, but also

exhibit nontrivial interactions with each other which impede their dampening of the bar. As the mean free path decreases, the $\mathcal{Q}$-factor dependency transitions from scaling as inversely with pressure toward being pressure independent.

The mean free path ℓ_{FP} is approximately 68 nm at STP[37]. The characteristic length λ_{char} is best taken as the shorter of the 2 dimensions that correspond to the surface of the nanobeam as it moves through the medium [38]. For our nanobeams, that is the height 400 nm, which gives us $K_n \approx 0.17$ at atmospheric pressure. This puts us well in the middle of the transition regime based on the Knudsen number.

However, based on the results of Verbridge et al. (2008)[38] we should expect to be able to obtain a reasonable estimate of the expected $\mathcal{Q}$-factor through consideration of the free-molecular regime. Verbridge demonstrated that a 55 nm wide Si_3N_4 nanobeam follows the free-molecular limit all the way to atmospheric pressure, despite having a $K_n \sim 1$. The pressure dependence of a much wider 1.5 µm nanobeam ($K_n \sim 0.05$ at 1 atm) began to deviate from $\mathcal{Q} \propto P^{-1}$ behavior at around 1 Torr, but not by a large amount. The $\mathcal{Q}$ still demonstrated strong negative scaling with pressure, and had a final atmospheric $\mathcal{Q}$ of only 3 times the predicted value. Consequently, we expect our $\mathcal{Q}_{atm}$-behavior to fit somewhere in the range $\mathcal{Q}_{atm} \approx \mathcal{Q}_{fm}|_{atm} \cdot (2 \pm 1)$. Although such an approach may seem inaccurate, such strategies are standard in the transition regime due to the lack of models. For example, when considering nanobeams near the viscous limit, a recommended approach is to simply modify the viscosity μ to μ_{eff}, where μ_{eff} is experimentally determined [39, 36].

Christian (1966)[40] first derived the expected damping for rigid beams in the free-molcule regime, and Newell (1968)[35] clarified the result and derived the corresponding quality factor:

$$\mathcal{Q}_{fm} = \left(\frac{\pi}{2}\right)^{3/2} \frac{\rho\, t f}{P} \sqrt{\frac{k_B T}{m_{air}}} \tag{2.102}$$

where ρ is the density of the beam material, t is the thickness of the beam, f is the frequency of the beam, P and T are the environmental pressure and temperature, and m_{air} is the average mass of an air molecule. Li et al. (2007)[41] later showed that the same equation was also applicable to for elastic beams using the results of Yasumura et al. (2000)[34]. Li et al. also provides a thorough derivation of Eq. 2.102.

Using the parameters for our Si_3N_4 nanobeams, and assuming the air is composed of N_2 molecules, we obtain the initial room-temperature prediction for our

$$\mathcal{Q}_{fm} = \left(\frac{\pi}{2}\right)^{\frac{3}{2}} \frac{3184\,\mathrm{kg/m^3} \cdot t f_1}{1.01 \times 10^5\,\mathrm{Pa}} \sqrt{\frac{k_B \cdot 300\,\mathrm{K}}{4.65 \times 10^{-26}\,\mathrm{kg}}} \tag{2.103}$$

$$\approx 1.85 \cdot \left[\frac{f}{1\,\mathrm{MHz}}\right] \cdot \left[\frac{1.01 \times 10^5\,\mathrm{Pa}}{P}\right] \left[\frac{t}{100\,\mathrm{nm}}\right] \tag{2.104}$$

which effectively serves as a lower bound for our $\mathcal{Q}_{air}$ estimation.

By combining this result with the predictions of $\mathcal{Q}_{mech}$ in the previous section, the expected total quality factor of the nanomechanical resonance $\mathcal{Q}_{tot} = (\mathcal{Q}_{mech}^{-1} + \mathcal{Q}_{fm}^{-1})^{-1}$ is shown in Fig. 2.22.

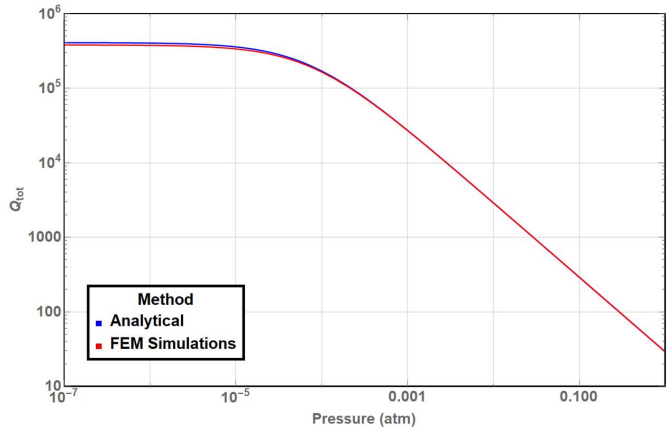

Figure 2.22: Predicted pressure dependency on observed nanomechanical $\mathcal{Q}$-factors, for both analytic approximations and numerical estimates obtained using FEM simulations.

2.3 Optomechanical Coupling

Now that we have independently studied the optical and mechanical system which act as the foundations of our photonic integrated device, we examine how the two systems should interact with each other. FIMMWAVE simulations are used to calculate the relationship between the effective index of optical modes and the geometry and position of a nanobeams located just outside ring waveguide. With this, we estimate the potential strength and behavior of the resulting optomechanical interaction.

As discussed in Section 1.1.2, to estimate the strength of the optomechanical interaction we must determine the optical frequency shift in the resonator per unit displacement of the mechanical oscillator, given by:

$$G = -\frac{\partial}{\partial x}\omega_{res}(x) = -\frac{\partial}{\partial x}(\omega_{res} + \delta\omega_{OM}(x)) \tag{2.105}$$

$$= -\frac{\partial}{\partial x}\delta\omega_{OM}(x) \tag{2.106}$$

where $\delta\omega_{OM}(x)$ is the shift in frequency due to the presence of the nanobeam, reproduced here:

$$\delta\omega_{OM}(x) = \frac{\omega_{res}}{2\pi}\frac{1}{n_{eff}}\int_{\theta_-}^{\theta_+}\big(n_x(\theta) - n_\infty\big)d\theta \tag{1.84}$$

where $n_x(\theta)$ is the effective index of the ring mode at angular position θ along the ring, for a distance x between the ring and nanobeam. Let us define the function:

$$N(x) = \int_{\theta_-}^{\theta_+}\big(n_x(\theta) - n_\infty\big)d\theta \tag{2.107}$$

such that we can write:

$$G = \left(\frac{\omega_{res}}{2\pi}\frac{1}{n_{eff}}\right)\left[-\frac{\partial}{\partial x}N(x)\right] \tag{2.108}$$

We call $N(x)$ the Integrated Index Shift caused by the presence of the optomechanical resonator. The quantity $\frac{\partial}{\partial x}N(x)$ is thus the Integrated Index Shift per Displacement, which is directly proportional to G.

2.3.1 Simulations

To calculate $N(x)$, we obtain $n_x(\theta)$ through simulating waveguide cross-sections representative of a mechanical nanobeam a distance x from an optical ring resonator. A sample simulation geometry is shown in Fig. 2.23a. To more accurately simulate the final fabricated cross-section, we implement an 'overetching' of the SiO_2 layer on the sides, which occurs when the Si_3N_4 nanobeam is undercut by a vapor HF process. By performing a parameter sweep over the distance between the two Si_3N_4 sections, we obtain the effective index data shown in Fig. 2.23b. This data is converted to the angular $n_x(\theta)$ by considering the distance from the ring at angle θ (where $\theta = 0$ is the point of closest approach), to the nanobeam, perpendicular to the direction of propagation. The

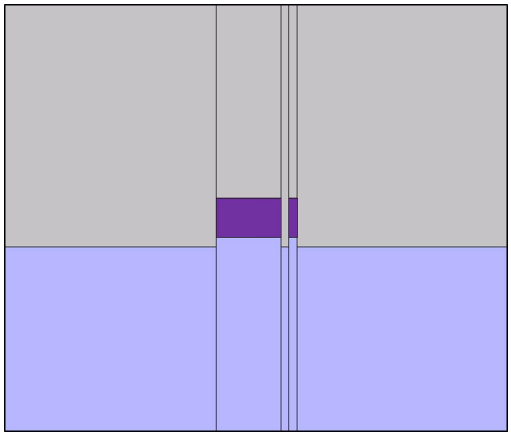

(a) Simulation setup. Si_3N_4, SiO_2, and air are respectively shown in purple, blue, and grey.

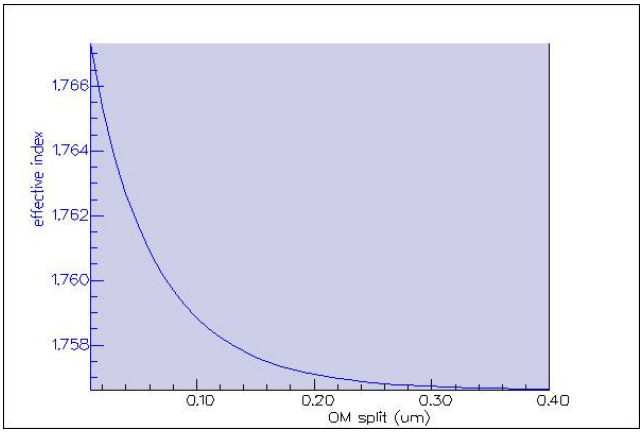

(b) Effective index simulation results for 800 nm wide waveguide with 100 nm wide nanobeam.

Figure 2.23: Geometry and sample results of simulations used to determine shift in effective index of optical modes

values for n_∞ are obtained from the asymptotic values of the effective index. Plots of the integrand $[n_x(\theta) - n_\infty]$ are shown in Fig. 2.24 as a function of the optomechanical split, from the data shown in Fig. 2.23b.

The integrated index shift per displacement $\frac{\partial}{\partial x}N(x)$ is calculated by integrating the individual curves in Fig. 2.24, interpolating the resulting values as a function of x, and taking the derivative. We are interested in determining the dependency of the coupling strength on various parameters of the ring resonator and mechanical nanobeam. Since the optomechanical coupling strength is scaled directly from the index shift per displacement, it is sufficient to compare values of the latter to determine the dependency of the former.

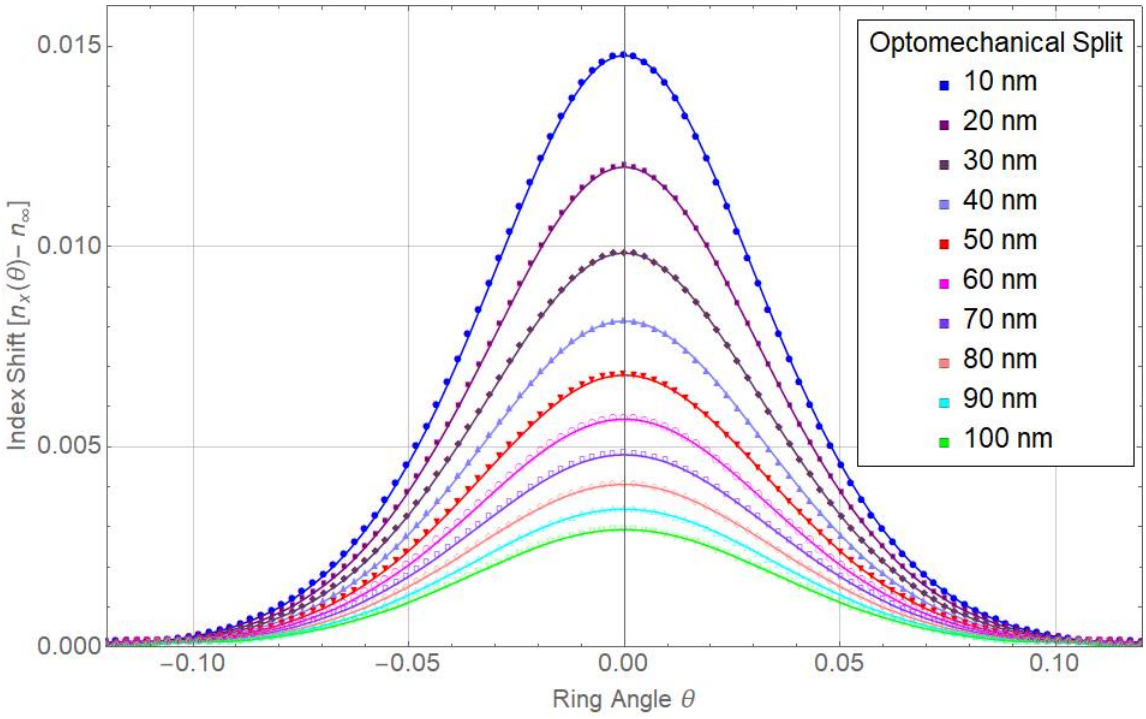

Figure 2.24: Change in effective index for varying optomechanical split. The integral of each curve represent N(x), and the change between those integrals as a function of optomechanical split is $\frac{\partial}{\partial x}N(x)$.

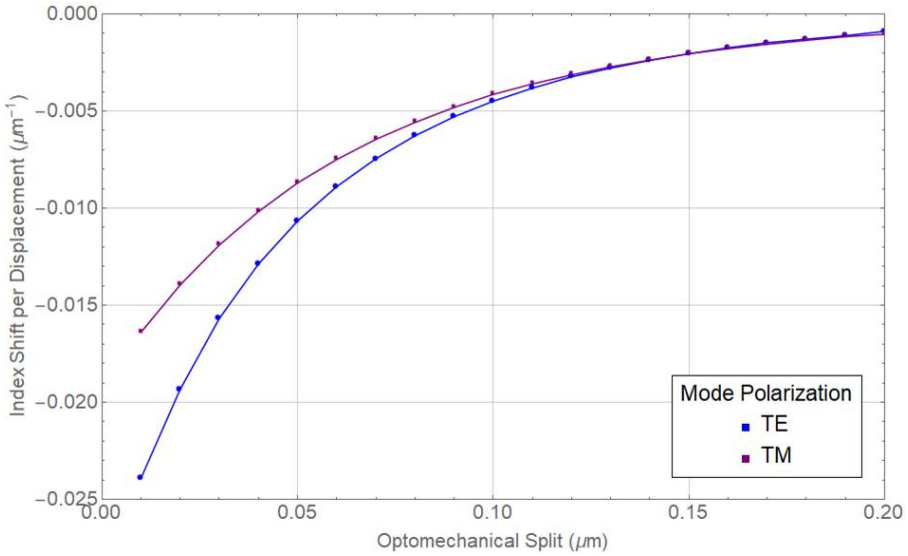

Figure 2.25: Calculated Integrated Index Shift curves of the TE and TM modes of a 800 nm wide single-mode optical ring resonator with a radius of 50 µm, optomechanically coupled to a nanobeam of width 100 nm.

2.3.1.1 Mode Polarization

As shown in Fig. 2.25, the TE modes are predicted to exhibit stronger coupling to nanobeams. Although there is only an $\approx 20\%$ difference when the split is on the order of 50 nm, the difference increases to $\approx 50\%$ when the nanobeam is within 20 nm. This could be predicted from the slopes on Fig. 2.3. Overall, TE modes demonstrate stronger increases in effective index as the waveguide geometry changes. This is most likely due to the fact that TE modes generally have stronger interactions with the sidewalls, whereas the TM modes live on the surfaces. When changing the waveguide geometry, the overally confinement of the mode changes. The TE modes interact more or less with the material outside the sides, and the TM modes interact less with the material above and below the waveguide. Since the material below the waveguide (SiO_2) has a closer index to the waveguide material (Si_3N_4) than the material above and to the sides of the waveguide (air/vacuum), the effect of the change in interaction with the material below the waveguide is reduced.

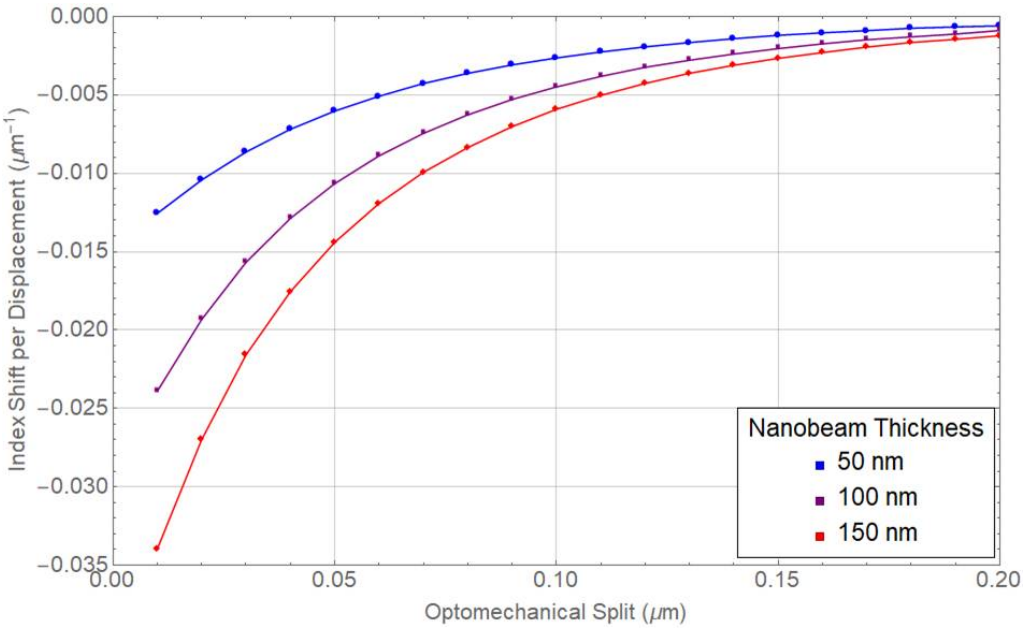

Figure 2.26: Calculated Integrated Index Shift curves for the TE mode of a 800 nm wide single-mode optical ring resonator with a radius of 50 µm, optomechanically coupled to nanobeams of varying widths.

2.3.1.2 Nanobeam Width

In general, we see that the strength of the interaction scales fairly linearly with the size of the nanobeam. By doubling or tripling the width, the final effect on the optomechanical coupling appears to scale by approximately as much. Since the motion of the nanobeam scales with the inverse square root of the mass, by:

$$x_{ZPF} = \langle \hat{x}^2 \rangle^{1/2} = \langle 0|\hat{x}^2|0\rangle^{1/2} = \sqrt{\frac{\hbar}{2m_{eff}\Omega_m}} \tag{xzpf}$$

this suggests that wider nanobeams might be better for optomechanical coupling, since a linear scaling of G with with respect to width would imply:

$$g \propto G x_{zpf} \propto \frac{G}{m_i} \propto w_{NB}^{1/2} \tag{2.109}$$

However, as discussed in Section 2.2.2.1, this leads to a reduction the mechanical quality factors $\mathcal{Q}_{mech}$ of the nanobeam. As such, the ideal nanobeam width is situation dependent, with the ability to sacrifice f$\mathcal{Q}$ product for an increase in optomechanical coupling by increasing the width of the nanobeam.

2.3.1.3 Ring Radius

Overall, the index shift per displacement increases as rings are made smaller. Although the nanobeam interacts with smaller rings over a shorter distance, the phase of the smaller rings is more strongly effected, leading to greater optomechanical coupling. This appears to be yet another reason why smaller rings are better for optomechanical applications.

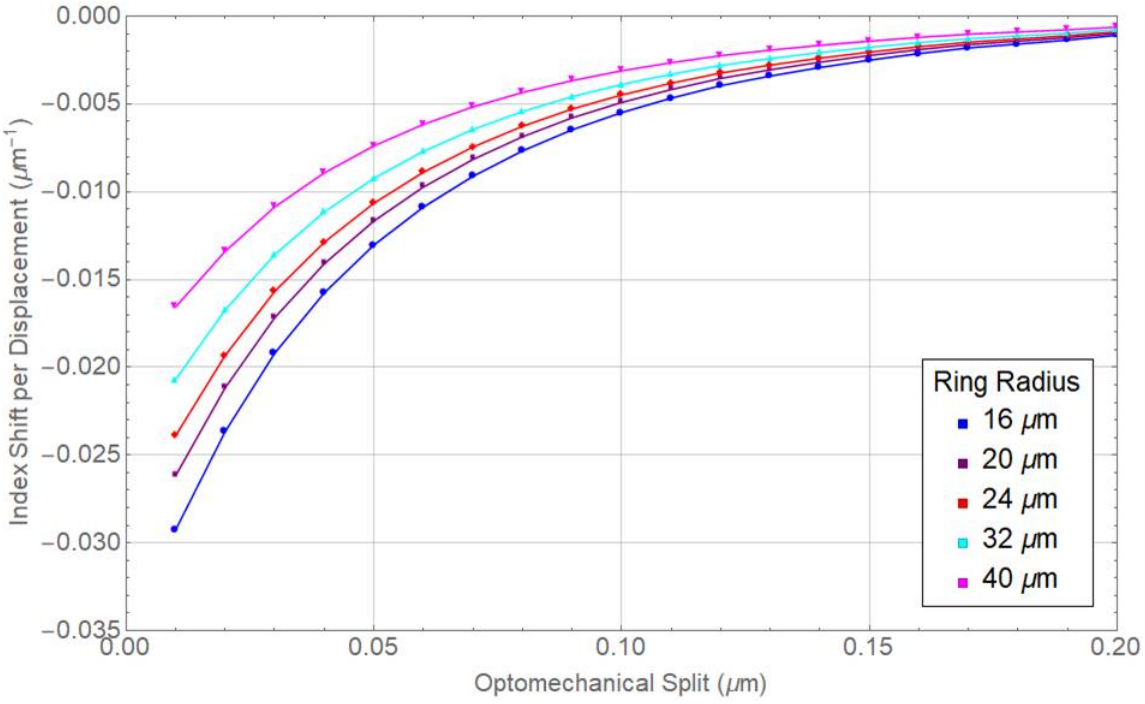

Figure 2.27: Calculated Integrated Index Shift curves for the TE modes of 800 nm wide single-mode optical ring resonators of varying radii, optomechanically coupled to a 100 nm wide nanobeam.

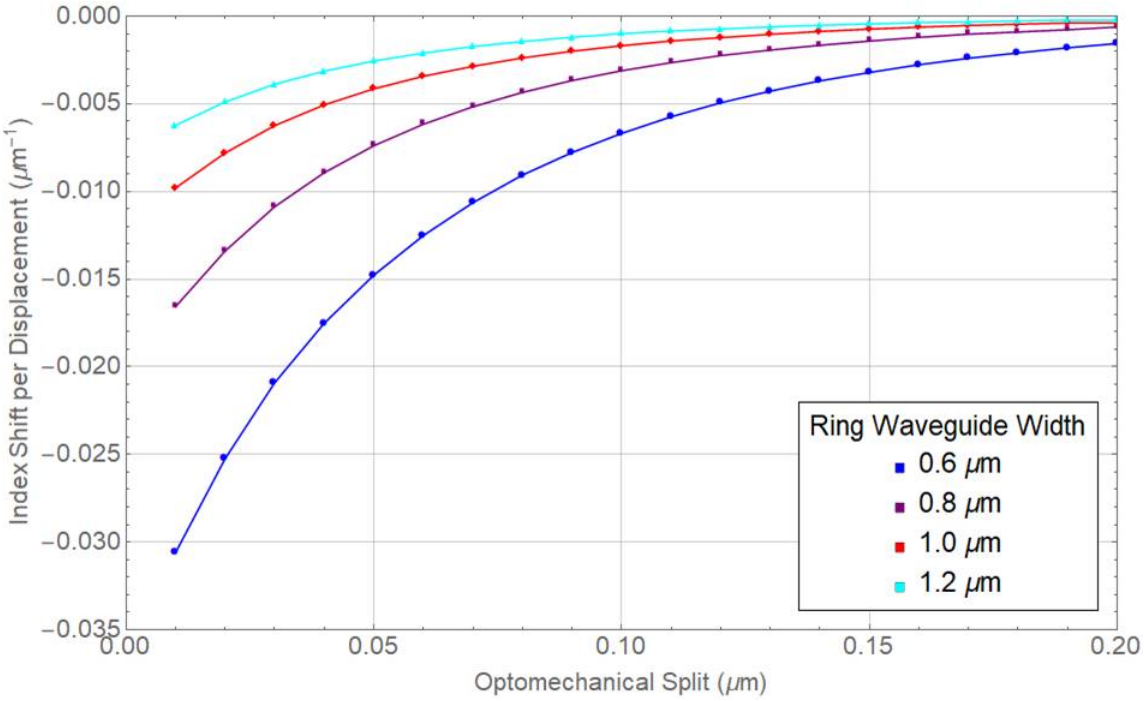

Figure 2.28: Calculated Integrated Index Shift curves between a 100 nm wide nanobeam and 50 µm radii optical ring resonators of varying widths.

2.3.1.4 Ring Waveguide Width

The increased confinement from narrower ring waveguides results in an increased sensitivity to the presence of the nanobeams. There is approximately a doubling of the predicted optomechanical coupling when going from 0.8 µm to 0.6 µm, and approximately a 60% when going from 1.0 µm to 0.8 µm. This is a fairly predictable outcome, knowing that the change in index of refraction as a function of waveguide width is concave down. If the oscillation of the nanobeam as viewed as changing the effective width of the core waveguide, then it would be moving up and down along a shallower sloped when modulating wider waveguides.

2.3.2 Estimation of Frequency Shift

To recapitulate the contents of this chapter, let us estimate the frequency shift due to an optomechanical interaction between a specific optical ring resonator and SRNB. Consider such a pair defined by the following parameters:

Table 2.2: Calculation Parameters of Sample SRNB

Parameter	Value
Ring Resonator	
Radius	16 µm
Width	800 nm
Height	400 nm
Si_3N_4 Nanobeam	
Length	20 µm
Width	100 nm
Height	400 nm
Initial Stress	1140 MPa
δx	500 nm
R_{curv}	50 µm
Coupling Splits	
Optical	400 nm
Optomechanical	40 nm

1. The release parameters δx, R_{curv} of the Si_3N_4 nanobeam allow us to calculate the final tensile stress in the nanobeam after removal of the SiO_2. Using Eq. 2.50, we predict that the stress in the nanobeam decreases from 1140 MPa to 674 MPa.

2. Either calculations or simulations are used to estimate the frequency and effective mass of the fundamental mode:

   (a) For $\sigma = 674$ MPa, Eq. 2.55 predicts a fundamental frequency of 12.2 MHz. If we assume $\frac{m_{eff}}{m} = 0.48$, then we get $m_{eff} \approx 1.22 \times 10^{-15}$ kg.

(b) COMSOL simulations with $\epsilon_x x = \epsilon_y y = \frac{674\text{ MPa}}{280\text{ GPa}}$ yield a fundamental frequency of 12.2 MHz and $m_{eff} \approx 1.22 \times 10^{-15}$ kg.

3. The thermal amplitude of the fundamental mode is estimated using Eq. 2.68. For $\omega_1 = 2\pi \cdot 12.2$ MHz, $m_{eff} = 1.22 \times 10^{-15}$ kg, and $T = 300\,\mathrm{K}$, we get:

$$\delta x_n = \frac{2}{2\pi \cdot 12.2\,\mathrm{MHz}} \sqrt{\frac{k_B\, 300\,\mathrm{K}}{1.22 \times 10^{-15}\,\mathrm{kg}}} \approx 48.1\,\mathrm{pm} \tag{2.110}$$

or approximately a 0.1 nm peak-to-peak amplitude for the Si_3N_4 nanobeam.

4. FIMMWAVE predicts $n_{eff} \approx 1.70$ for the given cross-sectional parameters of the ring, as seen in Fig. 2.3.

5. From Fig. 2.27, we see that $\frac{\partial}{\partial x} N(x)|_{x=40\,\mathrm{nm}} \approx -0.016\,\mu\mathrm{m}^{-1}$. Using this value, Eq. 2.108 gives us:

$$\begin{aligned} G &= \left(\frac{\omega_{res}}{2\pi}\frac{1}{n_{eff}}\right)\left[-\frac{\partial}{\partial x}N(x)\right] && (2.111)\\ &= \frac{2\pi \cdot 283\,\mathrm{THz}}{2\pi}\frac{1}{1.70} \cdot 0.016\,\mu\mathrm{m}^{-1} && (2.112)\\ &\approx 2\pi \cdot 0.42\mathrm{MHz/pm} && (2.113) \end{aligned}$$

6. This leads to an oscillation in the resonant frequency of the ring with an amplitude $\delta\omega_{OM}$, approximated by:

$$\delta\omega_{OM} = G \cdot \delta x_n = 2\pi \cdot 0.42\ \mathrm{MHz/pm} \cdot 48.1\ \mathrm{pm} \approx 2\pi \cdot 20.1\,\mathrm{MHz} \tag{2.114}$$

7. The fractional shift in signal will depend on the quality factor of the optical ring. From simulation of the coupling region (Section 2.3), 400 nm optomechanical split corresponds to $\mathcal{Q} \approx 150000$. This leads to a FWHM of the optical resonance of

$\Gamma = \frac{282\,\mathrm{THz}}{150000} \approx 1.9\,\mathrm{GHz}$. It can be shown that the maximum slope of a Lorentzian with signal voltage height V_0 is $\frac{3\sqrt{3}}{4}\frac{V_0}{\Gamma}$. The fractional response of the signal to a change in the resonance parameter is thus given by:

$$\frac{\delta V}{V_0} \approx \frac{3\sqrt{3}}{4}\frac{2(\delta\omega_{OM}/2\pi)}{\Gamma} \tag{2.115}$$

$$= \frac{3\sqrt{3}}{4}\frac{20.1\,\mathrm{MHz}}{1.9\,\mathrm{GHz}} \tag{2.116}$$

$$\approx 0.03 \tag{2.117}$$

Thus, the photodetector voltage will be modulated by $0.03\,V_0\exp(i\Omega_m t)$, which will then be detected by a signal analyzer or lock-in amplifier, as discussed in Section 5.4. The resulting frequency-space analysis will be broadened by the dampening of the mechanical resonator, in such a way that the integrated signal must correspond to 1 $k_B T$ of energy per mode. The ability to resolve the resulting peak in frequency space is determined by the effect of this broadening in comparison to background sources of frequency noise, such as classical and shot noise of the laser, which are outside the scope of this chapter. Sources of noise in optomechanical systems is well covered by the thesis of F. M. Buters [**?**].

Chapter 3

Characterization and Optimization of the Fabrication Process

Conservatively, the characterization and optimization of the fabrication process represents over 80% of the actual work put into this project. In many ways, designing and characterizing this new fabrication process has been an adventure through a deep dark forest in which $2 + 2 = 5$, and the path leading out is only wide enough for one.[1] I am particularly reminded of an instance in which the fabrication process failed because an individual step was done too well, and a little imperfection was the necessary ingredient to success. It would be unreasonable, if not impossible, to properly document every complication, diagnosis, and resolution encountered. Instead, we focus on the current procedure, and point out where potential issues might arise. A consequence of this approach is that most weeks of work are reduced to a fraction of a sentence, and some entire months do not even get that.

In this chapter, we discuss the fabrication of our integrated optomechanical system,

[1] A phrase I am borrowing from from 8^{th} World Chess Champion Mikhail Tal, where he describes a sharp and tactical game of chess in which the 'correct' moves are often counter-intuitive and simply require you to find them over the board.

consisting of optical ring resonators coupled to 'snap-release' nanomechanical resonators (Fig. 3.2). First, the device design is presented along with an outline of the current fabrication process. Then, the individual steps of the fabrication process are examined, including development and optimization. The results of fabricated devices are presented in Chapter 5.

A representation of our fabricated devices is shown above in Fig. 3.1. Each nanomechanical resonator, a rectangular nanobeam, is coupled to a double-bused optical ring resonator, all fabricated from the same layer of Si_3N_4 (shown in burgundy). Outside of the device region, an SiO_2 cladding (yellow) is deposited over the Si_3N_4 waveguides. The cladding protects the waveguides and reduces optical loss as the laser light propagates from the edge of the sample to each designated ring. The etched regions that define the waveguides terminate just short of edge of the sample, creating a uniform boundary of LPCVD Si_3N_4 that completely encapsulates the waveguide network from the sample edge. The thin wall around the circumference of the sample allows for the optomechani-

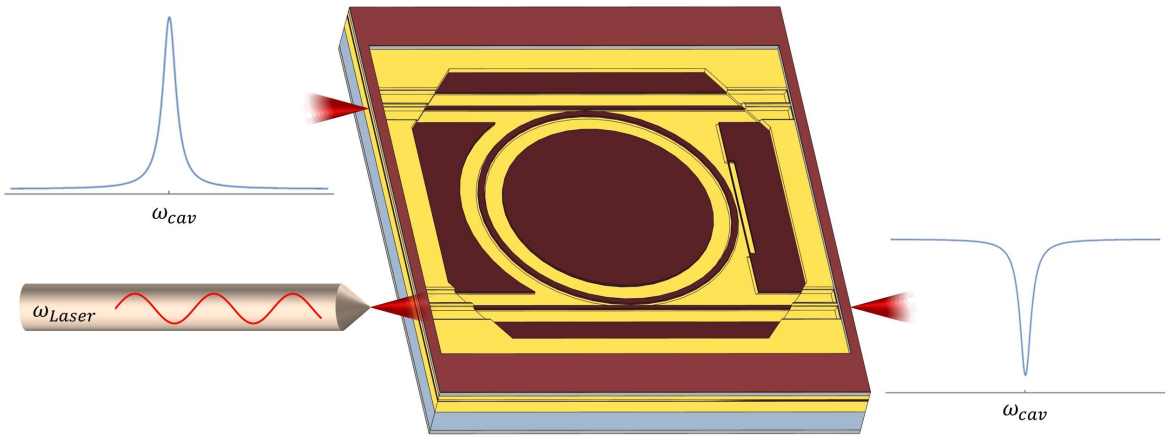

Figure 3.1: Topological representation of our device design. Light is coupled into the input waveguide (lower left) from a lensed single-mode fiber. Resonant light is absorbed by the ring and exits from the drop port (upper left). This light is usually then collected by a multi-mode lensed fiber (not shown).

cal system to be hermetically sealed at vacuum pressures by anodic bonding to the top boundary (Chapter 4). Despite the waveguides terminating short of the boundary, we are still able to couple in and out of them using lensed fibers, as long as the boundary layer is reasonably thin. Single-mode lensed fibers are used to couple to the input port of the input/throughput waveguide (lower left). Multi-mode lensed fibers (not shown) are used to collect light from the add or drop ports (upper left). By virtue of this double-bused design, photons collected from the drop port were absorbed by the ring resonator where they interacted with the Si_3N_4 nanobeam.

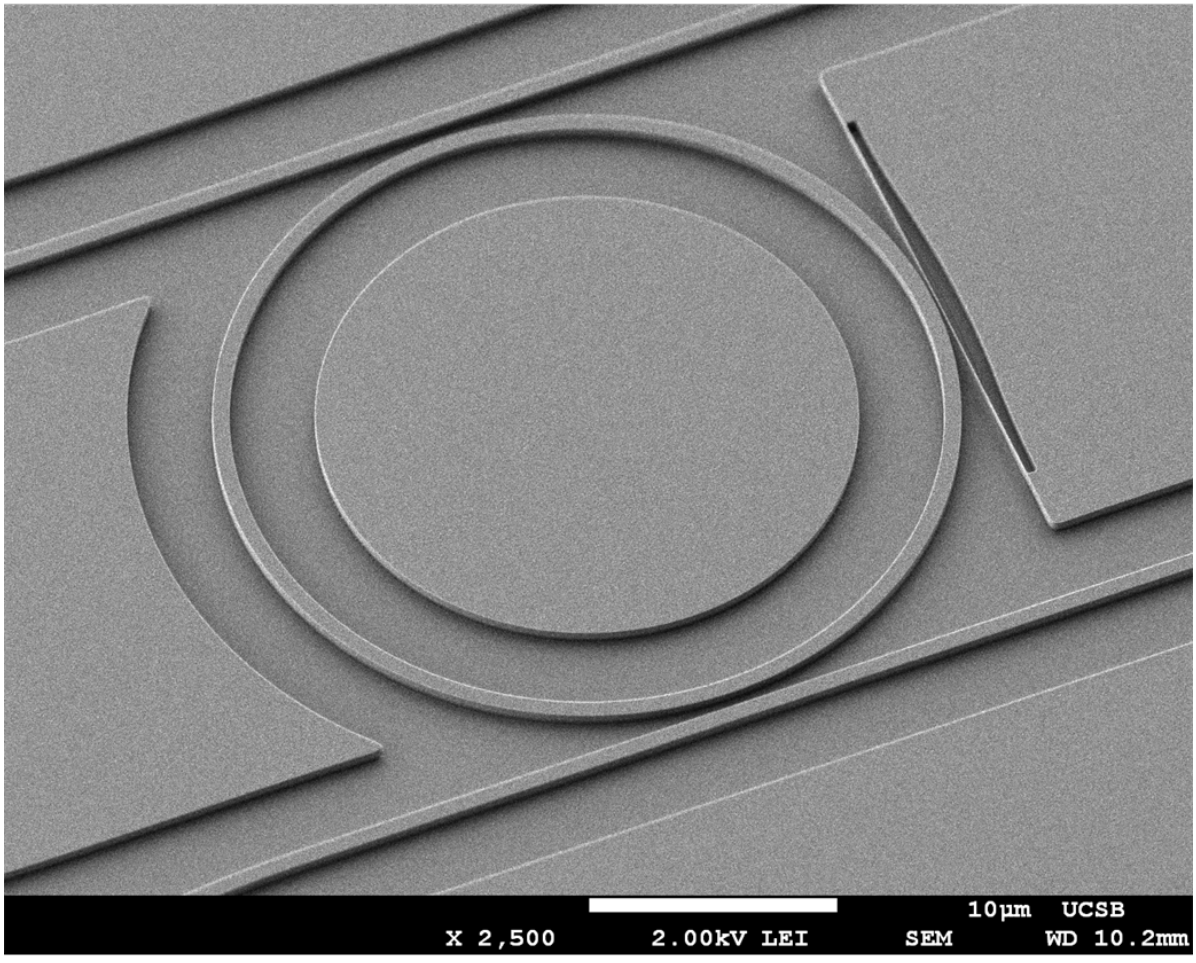

Figure 3.2: SEM image showing an individual optomechanical device from one of our samples. The ring resonator and 'snap-release' geometries are clearly visible.

3.1 Process Overview

The process starts with boron-doped, single-side polished 4" silicon wafers, with a 3.0 µm wet SiO_2 layer grown by Rogue Valley Microdevices (RVM). RVM then deposits 400 nm of stoichiometric Si_3N_4 on both sides using low-pressure chemical vapor deposition (LPCVD). RVM's LPCVD Si_3N_4 yields a tensile stress of approximately 1140 ± 15 MPa in the Si_3N_4 layer (personal communications, 2017), even though the advertised stress is >800 MPa. The total thickness of the stack is approximately 525 µm. For simplicity, a single 4" wafer is used for every full process run, which is capable of producing 4 complete versions of the mask (Section 3.2). The basic procedure is as follows:

1. **Metal Mask Layer Deposition:** Approximately 60 nm of chromium is deposited using electron-beam physical vapor deposition (EBPVD).

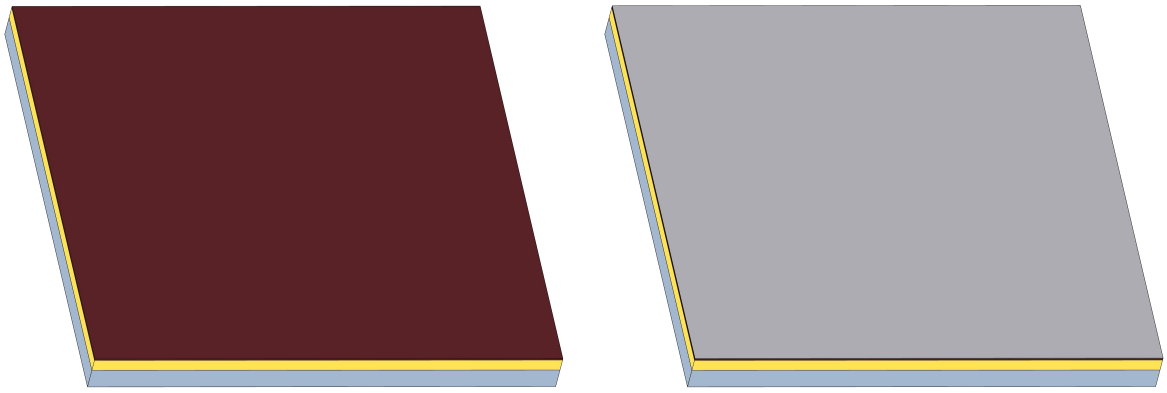

(a) Our initial wafer has 3 layer: Si (grey), SiO_2 (yellow), and Si_3N_4(maroon).

(b) 60 nm of chromium is deposited on the top layer.

Figure 3.3: Basic layers prior to lithography processes.

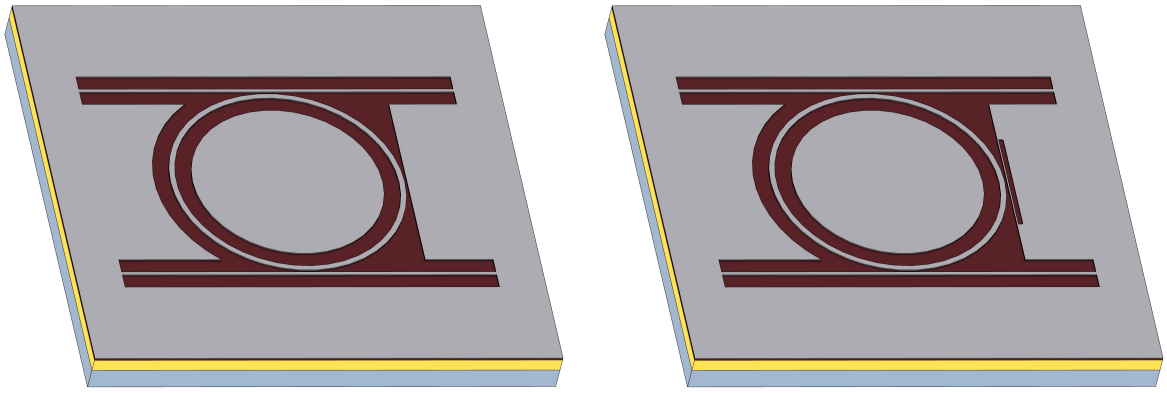

(a) DUV Lithography is used to pattern a 'template' mask, which consists of rings and waveguides of the photonic integrated system.

(b) Electron-Beam Lithography is used to modify the 'template' mask by strategically adding slits to form a thin structure near the rings.

Figure 3.4: The 60 nm chromium layer is etched using multiple techniques to yield a final mask which that yields thin mechanical oscillators released in close proximity to optical ring resonators.

2. **Etching of Chromium Hard Mask Layer (Section 3.3)**

   (a) **Deep Ultraviolet (DUV) Lithography (Section 3.3.1):** High-resolution DUV lithography is used to pattern rings, waveguides, and other large-scale structures. A thermal reflow of the resist reduces sidewall roughness.

   (b) **Etching of Template Pattern (Section 3.3.3):** A Cl_2/O_2 etch is used to etch through the chromium layer, imprinting the template pattern into it. (Fig. 3.4a)

   (c) **Electron Beam Lithography (EBL) (Section 3.3.2):** Ultra-high resolution EBL is used to pattern slits in the flat regions near the ring resonators.

   (d) **Etching of pattern modifications (Section 3.3.3):** An etch identical to (b) is used to imprint the slit patterns in the chromium mask, defining the unreleased mechanical nanobeams of the hard mask layer. (Fig. 3.4b)

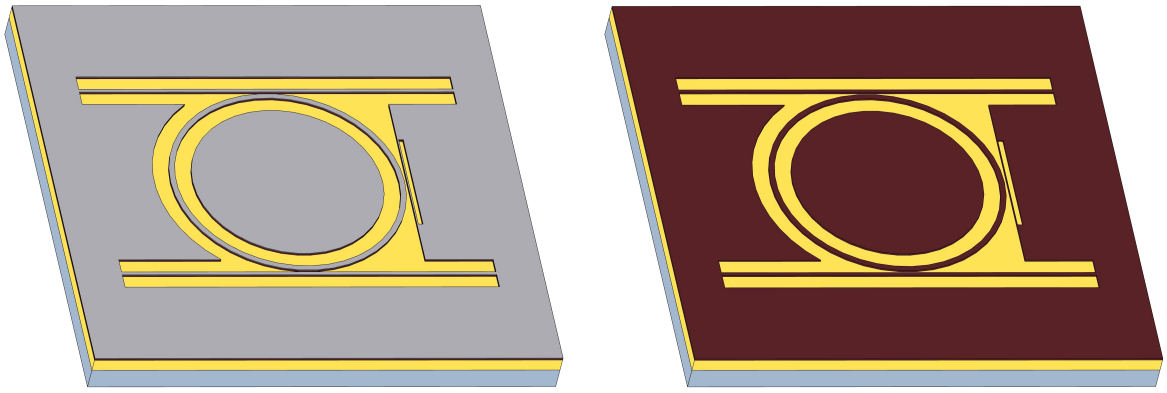

(a) Vertical etching of the Si_3N_4 using a CF_4/O_2 ICP etch.

(b) Removal of the metal mask layer leaves behind functional waveguides, optical ring resonators, and unreleased Si_3N_4 nanobeams.

Figure 3.5: ICP etching of the Si_3N_4 layer using chromium as a hard mask leads to near vertical sidewalls. The chromium can be removed afterwards using dry or wet options.

3. **Vertical etch of LPCVD Si_3N_4 (Section 3.3.4):** A CF_4/O_2 inductively-coupled plasma (ICP) process vertically etches through the Si_3N_4, realizing the image of the hard mask.

4. **Removal of metal mask layer and Surface Preparation:**

   (a) **Removal of metal mask layer:** A wet transene-based chromium etchant is used to remove the top chromium layer.

   (b) **Surface cleaning with Piranha Solution:** A 3:1 mixture of H_2SO_4 and H_2O_2, heated to 110 °C, is used to remove any chromium or organic residues.

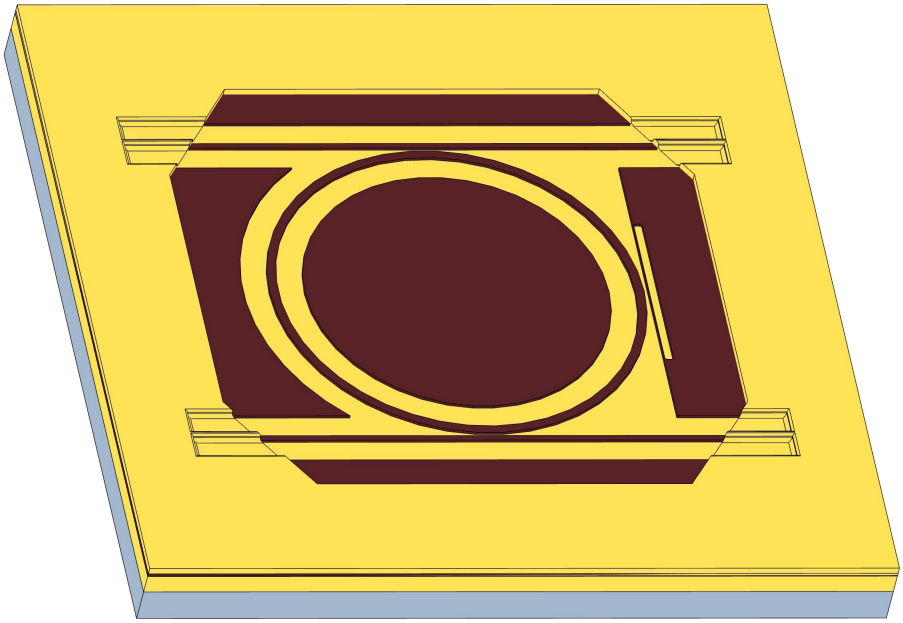

Figure 3.6: SiO_2 cladding is deposited on the Si_3N_4 waveguides located outside of the device regions, using RF-sputtering combined with a lift-off process. This both protects them and reduces loss in these waveguide regions.

5. **SiO_2 Cladding Layer (Section 3.4):**

   (a) **Stepper Lithography with dual-layer resist recipe:** A dual-layer resist recipe is used to protect the ring resonator regions. The bottom layer of the resist is excessively undercut to allow for easy lift-off after the dielectric deposition process.

   (b) **Cladding Deposition with RF Sputtering:** SiO_2 cladding is deposited everywhere but the regions containing the ring resonators.

   (c) **Dielectric Lift-off:** The photoresist protecting the ring resonators is removed by immersion in Nanomechanical Polish (NMP) at 80 °C. (Note: This part can be skipped if no-cleaning/characterization is needed before the wafer-bonding layers.)

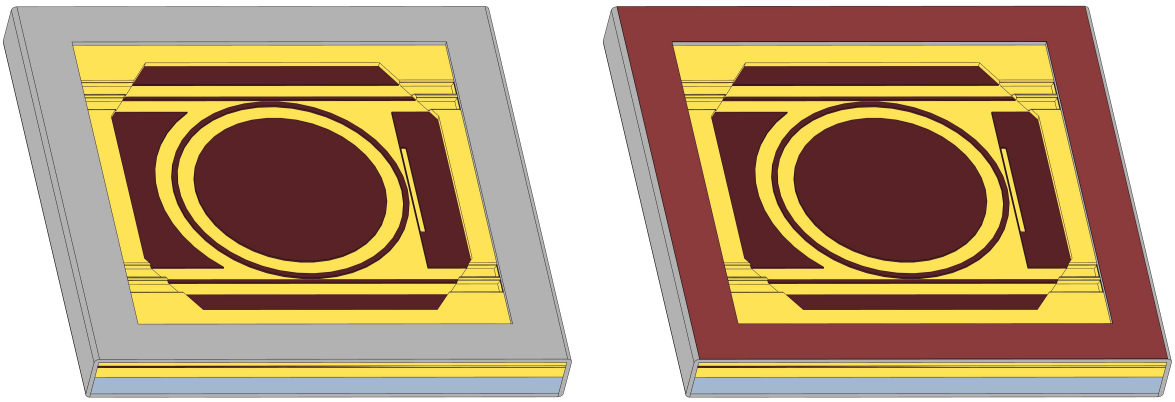

(a) A conductive material is deposited around the outside of the sample, shorting the top surface to the conductive Si wafer.

(b) Polycrystalline Si is deposited on top of the conductive layer.

Figure 3.7: A lift-off process is used to deposit a wafer-bonding compatible layer around the outer edges of the samples.

6. **Wafer Bonding Layer Deposition(Section 4.3):**

   (a) **Stepper Lithography with dual-layer resist recipe:** A dual-layer resist is used to protect all photonic regions of the sample.

   (b) **Conductive Layer Deposition (Section 4.2):** A conductive layer is deposited using EBPVD or sputtering. The deposition is done in such a way that it covers the top region that will be bonded to, as well as the side regions so as to short the top layer to the boron-doped Si wafer.

   (c) **Amorphous Silicon (α-Si) Deposition with RF Sputtering:** A thin layer ($\approx 50\,\text{nm}$) of α-Si is deposited using RF Sputtering.

   (d) **Dielectric Lift-off:** The photoresist protecting the photonic regions is removed by immersion in Nanomechanical Polish (NMP) at 80 °C. (Note: If lift-off was skipped for the SiO_2 cladding, then this step will remove that lift-off layer as well.)

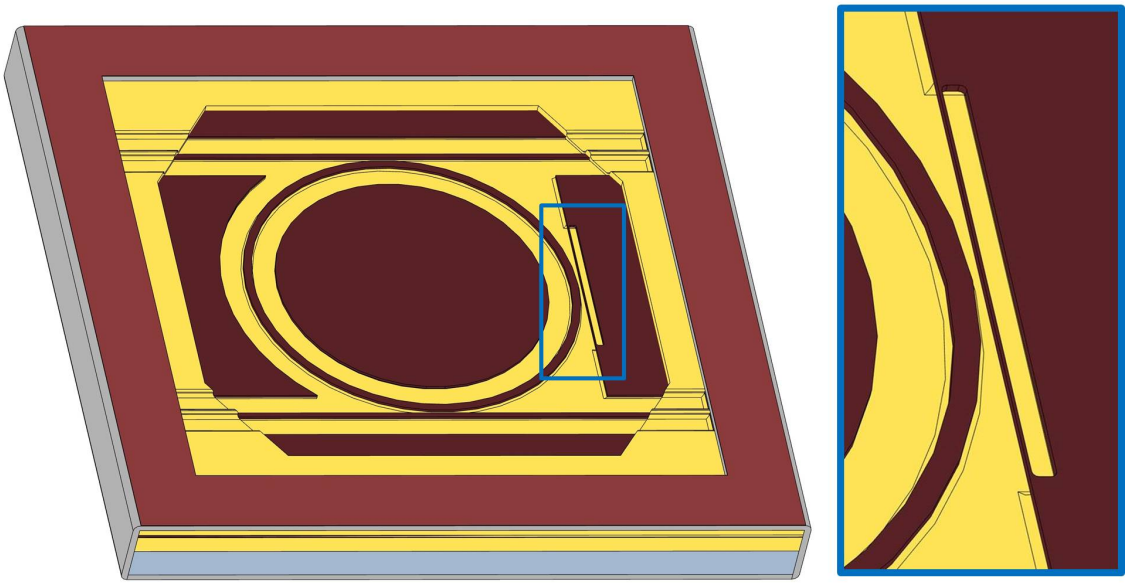

Figure 3.8: Removal of SiO_2 beneath the mechanical structures yields tall bridge-like structures. The fundamental mode of oscillation for such structures is in the wafer–plane, to and away from the optical ring resonator. The waferbonding layers protect the SiO_2 cladding from the vapor HF process, preserving surface uniformity in those critical regions.

7. **Undercutting of LPCVD SiN Optomechanical Elements with Vapor HF (Section 3.5):** A vapor HF process is used to released the mechanical structures that were defined by the electron-beam lithography. It is necessary to break the overall etch up into 30 second intervals to avoid complications from water-vapor build up on device surfaces.

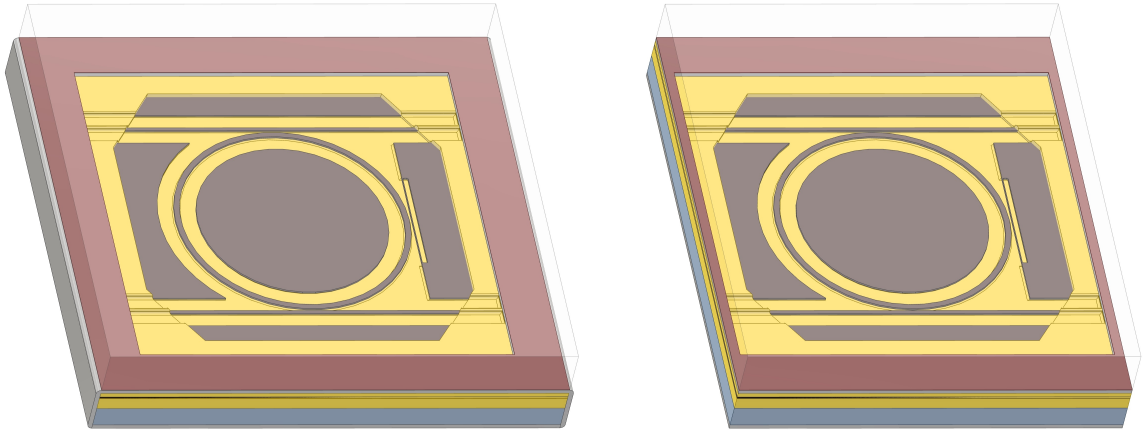

(a) Borofloat glass is bonded to the α-Si layer, hermetically sealing the ring resonators and mechanical oscillators at vacuum pressures.

(b) The hermetic seal is preserved by carefully polishing the bonding layer to no less than 10 µm.

Figure 3.9: Final packaging processes of the sample.

8. **Anodic Wafer Bonding (Chapter 4):** A Borofloat wafer is bonded to the α-Si layer using an anodic bonding. This hermetically seals the ring resonators and released nanobeams at 2×10^{-9} bar.

9. **Sample Dicing (Section 3.6):** Each sample is diced into 6 columns of ring devices.

10. **Facet Polishing (Section 3.6):** Approximately 20 µm of material is polished away from each edge, using various grades of polishing film.

3.2 Mask Design and Layout

The underlying geometry of our mask designs are shown in Fig. 3.10. They are 22 mm × 26 mm in extent, the maximum size the ASML DUV lithography system can image with the numerical aperture set to 0.57. Global EBL alignment marks, laser etch-depth monitoring pads, and fabrication characterization regions are found along the left and right sides of the mask. The central device region consists of a 6 × 6 array of independent device sets, each of which contains the framework for coupling to 12 ring resonators. The array is 3500 µm perodic in the horizontal direction, and 3600 µm periodic in the vertical direction. This periodicity is invaluable for utilizing stepper lithography for both the SiO_2 cladding and the waferbonding processes.

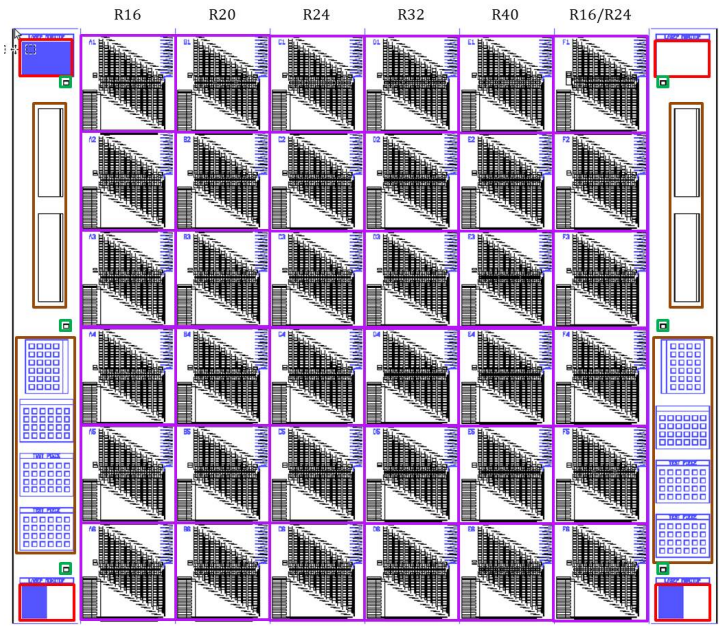

Figure 3.10: Schematic of ASML mask *ThickRings_v2*, designed for fabrication of bridges released on the outside of our ring resonators. The device region, located in the center, consists of a 6 × 6 array of sets of 12 rings (each boxed in plum). Three global EBL alignment marks are on each side of the device region. Laser etch-depth monitoring pads can be found on each corner. Test regions, containing structures for etch and mechanical release characterization, can be found along both sides.

Let us now look at the general design of an individual element of the array, and how we ultimately couple to each individual ring. A single set of rings is shown in Figure 3.11a. The input/throughput ports for all 12 rings are located on one side of the design, with all of the add/drop ports located on the other side. As can be seen in the figure, there is also a 13th pair of waveguides at the very end that acts a through-waveguide. This is invaluable for aligning the sample, as well as estimating maximum possible signal for the given fabrication. As can also be seen in the figure, every waveguide has a flat facet at one end and an angled facet in the other. This was implemented to avoid Fabry-Perot interference effects between two flat facets of the same waveguide.

Generally, light is coupled into the flat facet of one of the waveguides connected to the left side, where it then propagates to one of the 12 rings in the center. On resonance,

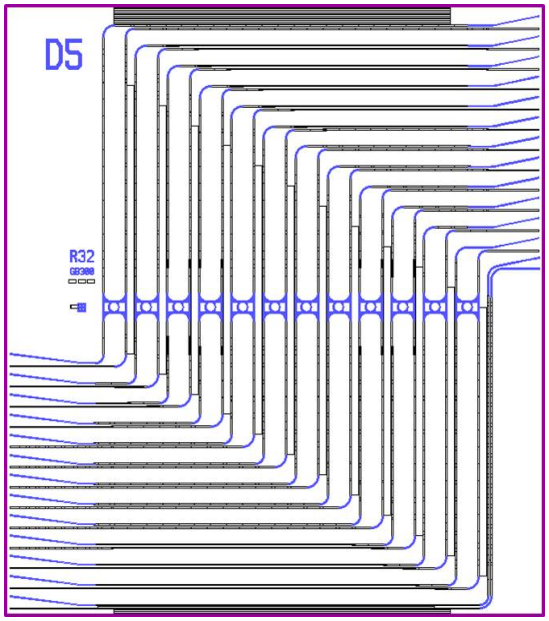

(a) General layout for any of the 36 device sets on the ASML mask. Usually, light is coupled into waveguides on the left side and collected on the right side.

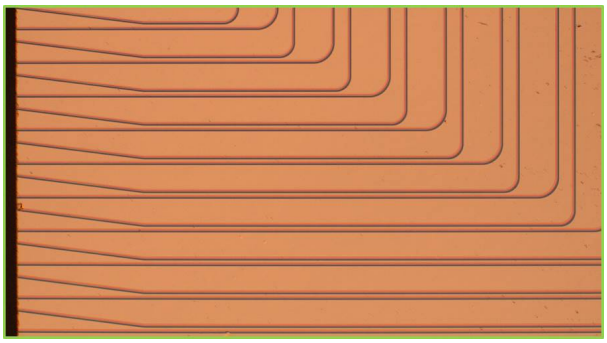

(b) Microscope image of the coupling region.

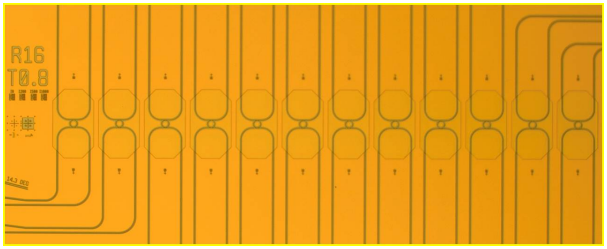

(c) Microscope image of the device region with 12 individual rings coupled to the outer edge.

Figure 3.11: Layout and images of a single set of 12 rings. The device region of our ASML mask is made up of a 6×6 array of such sets.

light is filtered by the ring and coupled to the add/drop waveguide on the other side. Light that couples through the add/drop waveguide exits through the corresponding flat facet on the right side (the drop port). The angled facets are used if reflections are an issue with the lensed fiber, or if there is damage to the waveguide between the flat facet and the ring.

The central ring region in Fig. 3.11c is further broken down in Fig. 3.12 on the next page.

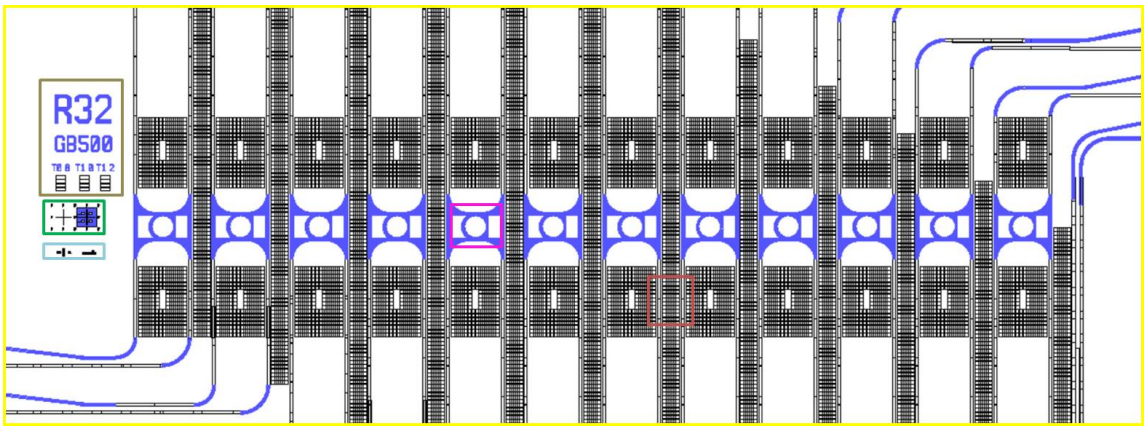

(a) Magnification of 1 of 36 ring device regions on the mask. There are 12 double-bused optical ring resonators of varying dimensions. A label of the devices, pair of positive/negative local EBL alignment markers, and a pair of horizontal/vertical 10 nmalignment calipers are all found to the left of the devices. Between the optical waveguides, 4 µm diameter circles prevent 'parastic modes' in the Si_3N_4 from coupling light from the input fibers to the collection fibers.

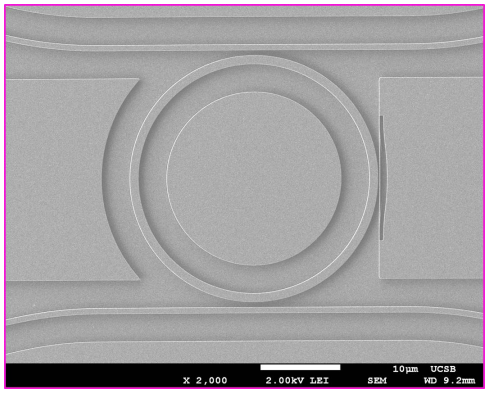

(b) Optical ring resonator with mechanical oscillator released.

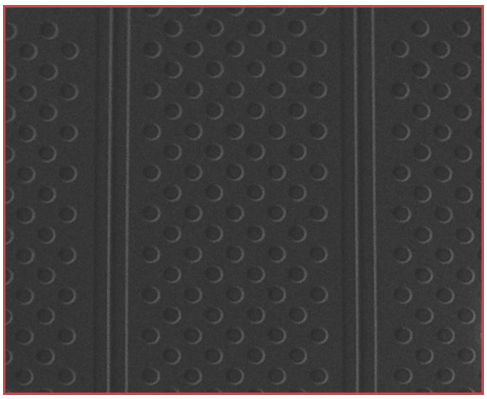

(c) 4 µm circles suppress 'parasitic' modes

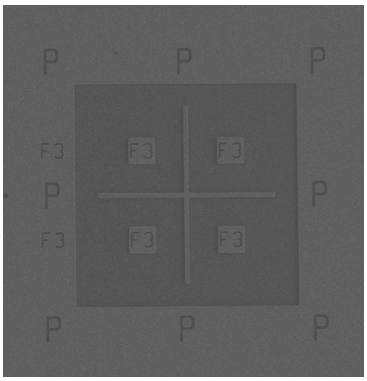

(d) Local alignment marks get exposed when being used during the EBL process.

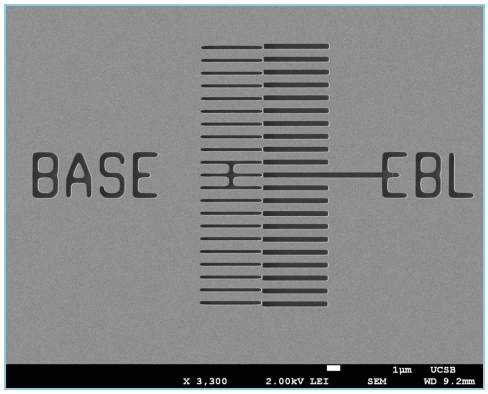

(e) Calipers show success of EBL write alignment to chromium template mask.

Figure 3.12: SEM Images of significant aspects of the ASML mask.

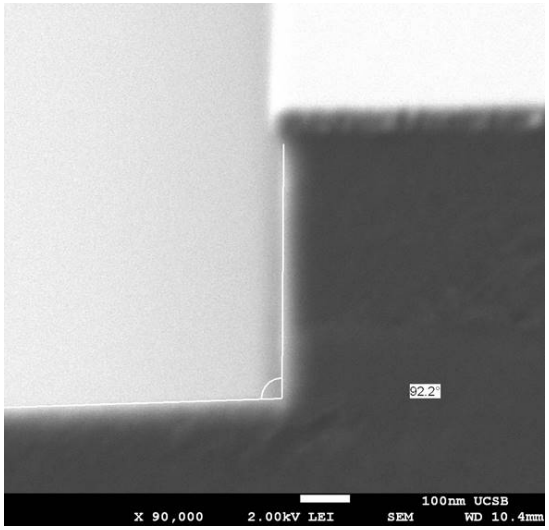

(a) Sidewall angles tend to have an angle of inclination greater than 85°.

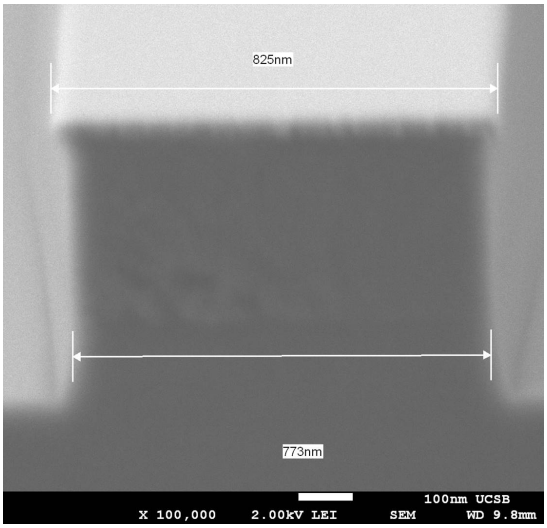

(b) Actual waveguide thickness tends to be approximately 20 nm inset from hard mask dimensions.

Figure 3.13: Vertical Etch profiles of Cr etch process.

3.3 Chromium Hard Mask and Vertical ICP Etching

A chromium metal mask is utilized, instead of standard photoresist, to yield nearly vertical sidewalls when etching through our LPCVD Si_3N_4 layer. Such vertical sidewalls are difficult to obtain when using photoresist as a masking layer, since the photoresist layer is etched away at a rapid rate by the presence of O_2 during the ICP anisotropic etch. Having vertical sidewalls in our LPCVD Si_3N_4 layer is vital for the fabrication of optomechanical devices intended to oscillate in the wafer plane. Vertical etch profiles from the chromium mask process is shown in Fig. 3.13, with the chromium mask still present on top.

Additionally, implementing a hard mask layer allows us to construct a single mask layer from multiple methods and/or steps of photolithography. We start with high-resolution DUV stepper lithography to pattern an initial 'template' mask. This mask contains >99% of the features to be defined. The template layer is then modified us-

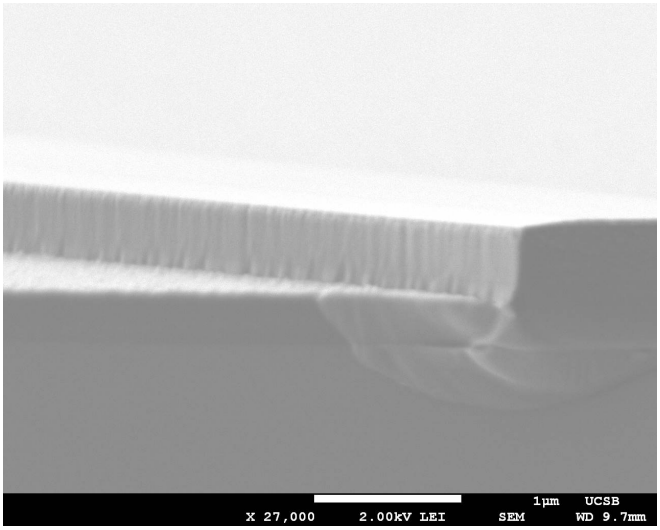

Figure 3.14: SEM Image of sidewall roughness following vertical etch of Si_3N_4 layer.

ing Electron Beam Lithography (EBL) to define the structure of our nanobeams. This gives us valuable flexibility with the ability to modify dimensions of nanobeams between fabrication runs, without having to design and order a new stepper mask.

3.3.1 High Resolution Deep Ultraviolet (DUV) Lithography

The highest resolution stepper lithography system available in the UCSB cleanroom is the the ASML 5500 DUV System. It uses 248 nm light from excimer lasers to expose chemically amplified photoresists, capable of resolving line structures down to 150 nm. Currently, we use cleanroom-stocked UV6 Positive DUV Photoresist. Exposures are done in the range of 12–18 mJ/cm^2, depending on the desired thickness of the final waveguides.

As can be seen in Fig. 3.14, any roughness in the chromium mask translates downward into the waveguides themselves. To improve the sidewall roughness of the final etch, it was necessary to implement as substantial thermal reflow of the resist. By heating the photoresist beyond its softening point, surface tension repairs much of the roughness. However, the photoresist also flows outward from this softening, requiring modifications

to the exposure dosage to compensate.

UV6 chemically amplified photoresist has a softening point around 145 °C. Following some calibration issues with the hotplates[2], thermal reflows of 145 and 150 °C were found to be insufficient at initiating surface-tension based repair of the sidewalls. A thermal reflow at 155 °C, however, was very effective at reducing sidewall roughness. However, the extent of the reflow was very sensitive to time. Reflows of 80 or 90 seconds seem ideal, with 120 seconds appearing to nearly liquefy the resist.

Due to the resulting variance in hard mask geometry from the sensitivity of the photoresist to the thermal reflow process at 155 °C, the ASML exposure is done with an energy exposure array. That is, each di is exposed to an incremenetally higher dosage than the previous one, resulting in a range of feature sizes from di to di. After SEM characterization of the resulting chromium hard mask, the di with the best feature sizes

[2]One of the most frustrating issues I came across was the variance and offset of hotplate temperatures within the UCSB NFF. To the point, the temperatures of any contact hotplate should be assumed to run 0–10 °C hot, which makes them unviable for use with the resist reflow process. The non-contact hotplate appears stable enough short term, but still needs to be checked regularly as the surface temperature has been shown to drift by 5 °C before cleanroom staff catches on. Because of this, prior to each resist reflow process, I recommend using a thermocouple attached to an Si wafer to check the temperature calibration of both the surface temperature and process temperature to keep track of this variable.

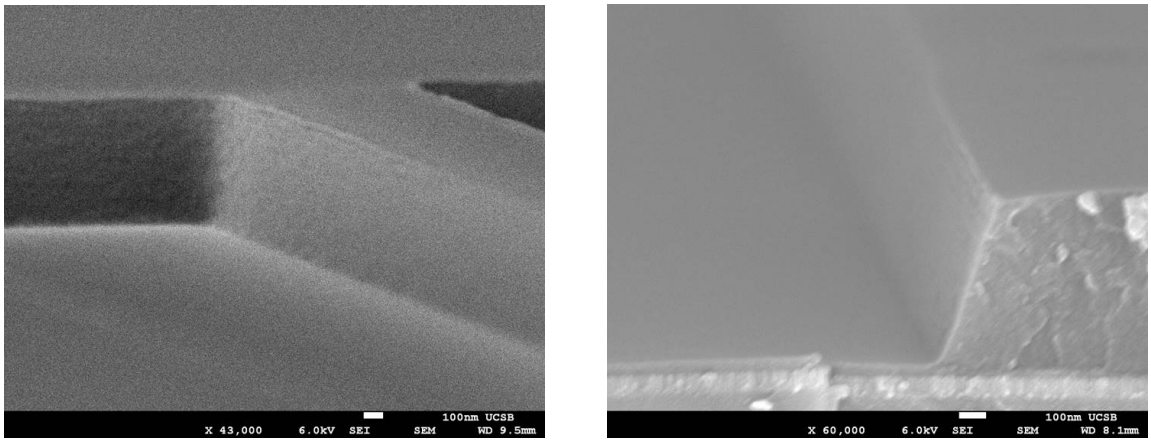

(a) Standard 135 °C PDB (b) 155 °C for 90 seconds.

Figure 3.15: Comparison of photoresist sidewall roughness, with and without a thermal reflow.

is selected for continued fabrication. The others are then used for test pieces, or to be processed later depending on the eventual results of the first-selected piece.

3.3.2 Ultra-High Resolution Electron Beam Lithography

Modification of the 'template' mask layer is done using a JEOL JBX-6300FS Electron Beam Lithography System, in conjunction with CSAR-62 (SX AR-P 6200/2) electron-beam resist and aquaSAVE conductive polymer. Four global alignment marks (P, Q, R, S) are used to account for sample position and rotation. Then, a local alignment mark is used for every row of rings to account for deviations in the the chromium mask pattern and the ideal mask geometry. Without local alignment marks, EBL patterns could only be consistently placed within 200 nm of their desired position on the mask. With local alignment marks, placement was generally improved to within 20 nm. For every row or rings, patterned calipers are used to determine the accuracy of the EBL positioning (See Fig. 3.12e).

3.3.3 Chromium Dry-Etching

Reactive Ion Etching (RIE) of chromium is done with chlorine and oxygen gases. The initial chromium-etching process recommended by clean-room staff was found to be unstable. Run-to-run variations on the etch rate could be greater than 50 %, essentially making the process nonviable. However, after several modifications beyond standard RIE procedures, the etch rate was stabilized, significantly improving viability of the process.

3.3.3.1 Purge Gas Selection

Helium gas is used as a purge gas, rather than standard N_2. Prior to the etching of the chromium, a layer of anti-reflective (AR) coating needs to me removed via an O_2

etch. If N_2 is injected into the etch chamber after the etch completes and the Cr layer is exposed, N^{3-} radicals in the plasma interact with the surface to form chromium nitride (CrN). CrN is insulating and has lower etch rates in the Cl_2/O_2 etch optimized for pure Cr layers.

3.3.3.2 Etch Loading Issues Induced by Carrier Wafer Interaction

After a couple years of experience with Cl_2/O_2 etching of chromium, it slowly became apparent the etch was somehow interacting with the 6" carrier wafer when compared with other etches. The carrier wafers would readily lose their luster and even start developing black spots in areas exposed to the etch. Etch rates would occasionally drop by up to 60% from one run to the next. This issue was reported by other people attempting to etch chromium via RIE methods.

We eventually postulated the etch was interacting with the silicon surface of the carrier wafer, ultimately leading to roughening of the surface. This roughening would effectively increase the surface area of the carrier wafer and consequently increase the interaction between the etch and the silicon. Our solution was to blanket the carrier wafer with a material known to not react with the etch, SiO_2. 1 µm of PECVD SiO_2 was deposited on a standard 6" carrier wafer to be exclusively used when etching with chromium.

The simple solution of using an SiO_2 carrier wafer proved very effective. Not only did the etch rates stabilize, but they stabilized at an etch rate 60% higher. This was most likely due to a loading effect between the etch reactants and the silicon carrier wafer. As such, it was necessary to recharacterize the etch profile, in case the effective gas ratios were effected by the loading.

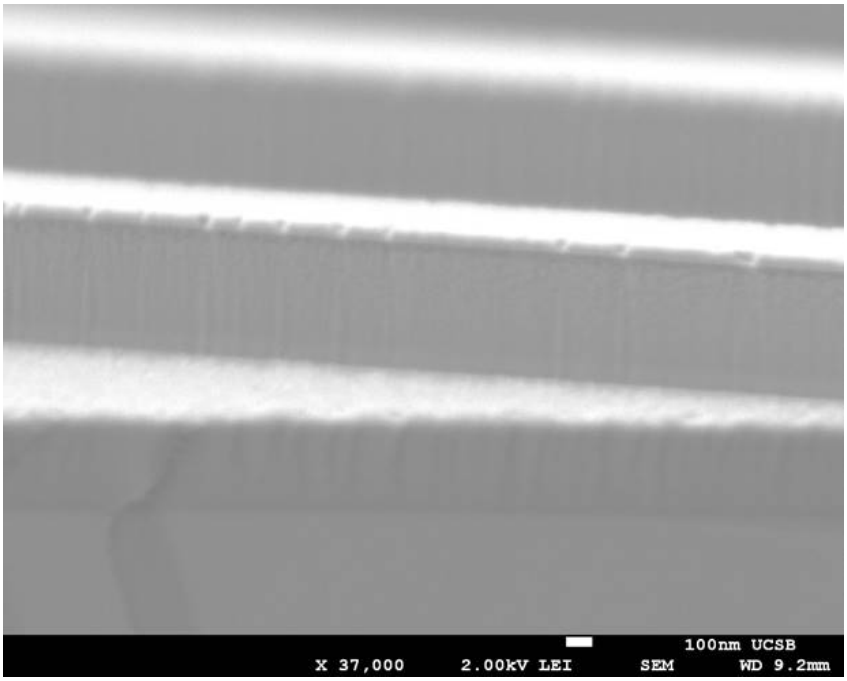

Figure 3.16: Notches along the outer edge of the chromium mask are correlated with sidewall roughness near the position of the notches.

3.3.3.3 Formation of Notches Along Edge of Chromium Mask

Originally, it was found that notches frequently formed along the edges of the chromium mask. As can be seen in Fig 3.16, these notches translate to sidewall roughness in the Si_3N_4 waveguides. We hypothesized that Cl^- residue was left along certain section of the mask edge following the Cl_2/O_2 etch. When the sample would reach atmosphere, the Cl^- residue would interact with the air to form droplets of hydrochloric acid (HCl) along the edges of the waveguide in random locations. As HCl is an active ingredient in chromium wet etchants, this could explain the formation of the notches.

Simply rinsing the sample in DI water was recommended to fix this problem. The idea was that the etching by HCl would not be fast enough to form significant notches if the residues were washed away as soon as possible. However, this did not solve the problem. Next, we decided to take advantage of the multi-recipe function of the ICP machines to

remove the Cl^- residue before the sample could reach vacuum. We originally tried:

Table 3.1: Chromium Etch Multi-Recipe: Remove resist, then clean (failed)

Step #	Active Gasses	Purpose
1	O_2	Removal of anti-reflective coating
2	Cl_2/O_2	etching of chromium mask layer
3	O_2	removal of remaining photoresist/AR coating
4	CF_4/O_2	removal of Cl^- residue

Not only did this not solve the problem, but new pits were found to form inward of the edge. With regard to persistent notch formation at the edge, it is reasonable to suspect that the Cl^- residue acted with the O_2 to continue etching the chromium. As for the pit-formation, we suspect that some Cl^- residue managed to find its way underneath the photoresist layer during the original etch process. Previously, this residue did not lead to etching as it was sufficiently sealed from the air by the photoresist. However, with the photoresist first removed, this hidden residue was now exposed to the same conditions as the residue at the edge, leading to further etching.

Simply swapping steps 3 and 4 proved sufficient to solve the issue entirely. As such, chromium etches followed the sequence:

Table 3.2: Chromium Etch Multi-Recipe: DUV Lithography

1	O_2	Removal of anti-reflective coating
2	Cl_2/O_2	etching of chromium mask layer
3	CF_4/O_2	removal of Cl^- residue
4	O_2	removal of remaining photoresist/AR coating

without breaking vacuum. In ICP#1 this is a standard feature. For ICP#2, this necessitates running the machine in *Test Mode* and performing the recipes manually in sequence. The resulting sidewalls are shown in Fig. 3.17, with chromium hard mask

layer still present on top.

The same procedure is followed for the chromium etch after the EBL patterning, but with the initial O_2 etch removed:

Table 3.3: Chromium Etch Multi-Recipe: Electron Beam Lithography

1	Cl_2/O_2	etching of chromium mask layer
2	CF_4/O_2	removal of Cl^- residue
3	O_2	removal of remaining E-beam resist

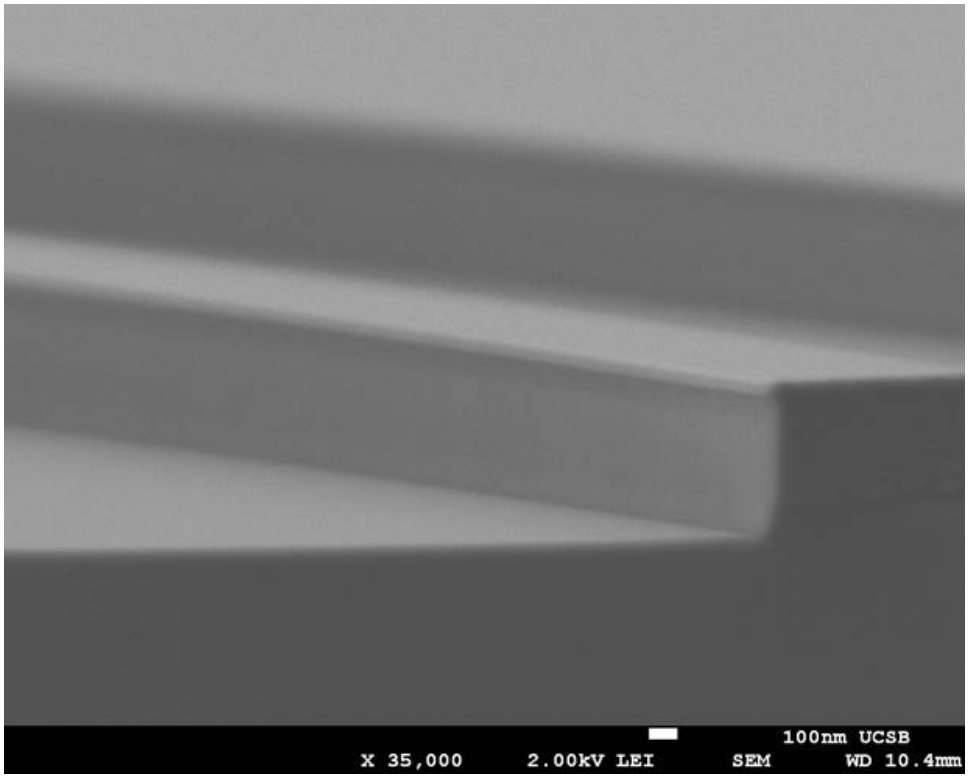

Figure 3.17: SEM image of sidewalls obtained using our optimized chromium etch process.

3.3.3.4 Chromium ICP Etch with Cl_2/O_2

The chromium dry etch recipe changed numerous times through modifications presented in the previous sections. The change was particularly dramatic following the change of the carrier wafer, where Cl_2 was dropped from 60 sccm to 24 sccm. Eventually, the following recipe was settled upon:

Table 3.4: Optimized Chromium Etch

Parameter	Value
Cl_2	24 sccm
O_2	6 sccm
Pressure	1.33 Pa
Source Bias	500 W
Forward Bias	25 W

Using this recipe, along with the right vertical dry etch for the Si_3N_4 layer below (Section 3.3.4), led to the sidewalls shown in Fig. 3.18.

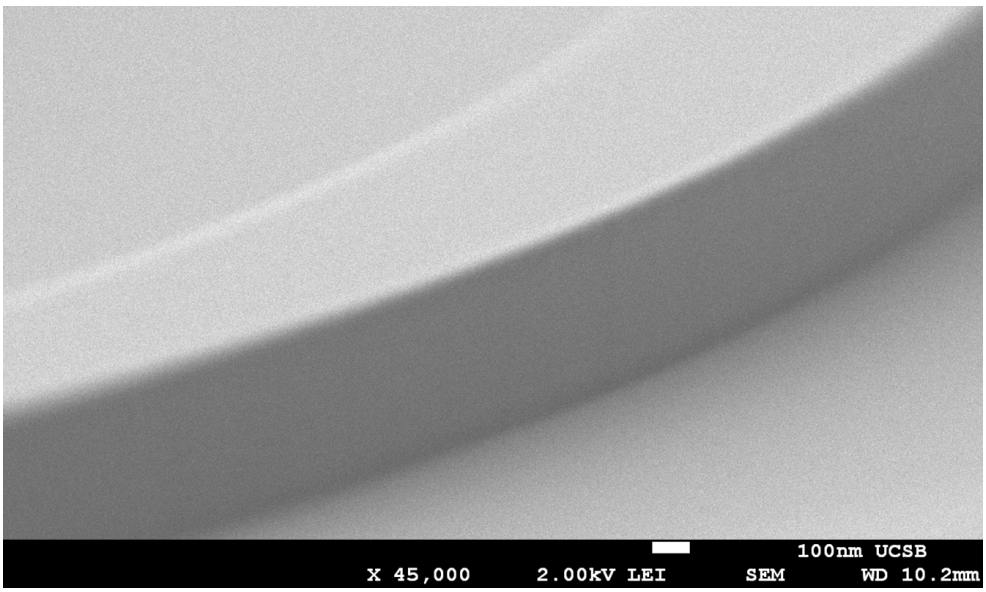

Figure 3.18: SEM Image of sidewall roughness following vertical etch of Si_3N_4 layer.

3.3.4 Vertical Etching of Si_3N_4

Generally, the vertical etching of Si, SiO_2, and Si_3N_4 is achieved using reactive ion etching with fluorine-containing plasmas. Commonly used gasses available in the UCSB NFF are CF_4, CHF_3, and SF_6. For Si_3N_4 specifically, CF_4 is most commonly used and works via the reaction:

$$12\,F + Si_3N_4 \longrightarrow 3\,SiF_4 + 2\,N_2 \tag{3.1}$$

where the fluorine ions are generated by the following reaction with plasma electrons

$$e^- + CF_4 \longleftrightarrow CF_3 + F + e^- \tag{3.2}$$

If O_2 is not present during the reactive ion etch, a fluorocarbon layer (CF_x) forms on the surface of the etched layers, inhibiting the etch rate. The introduction of O_2 suppresses the formation of the fluorocarbon layer and stabilizes the etch rate [42]. Specifically, the O_2 reacts with the CF_x, producing CO, CO_2, COF_2, and F [43]. If too much oxygen is present however, etch-resistant oxide patches can form on the surface, leading to grassing.

Passivation layers can be incorporated by including hydrogen or nitrogen containing process gasses such as CHF_3 and N_2. Such layers are used to protect the etch surface during the etch itself, or can be useful in some way after. For example, hydrogen passivation of Si_3N_4 surfaces is implemented in the field of photovoltaics to improve long-term stability of commercial solar cells. For such systems, hydrogen is bonded to dangling silicon bonds that otherwise create electrical issues.

Prior to our work, UCSB NFF staff member Bill Mitchell had already optimized the dry etching of Si_3N_4 for sidewall roughness. He provided the following recipe for use with ICP2:

Table 3.5: Si_3N_4 Vertical Etch (CHF_3-based)

Parameter	Value
CHF_3	35 sccm
CF_4	5 sccm
O_2	10 sccm
Pressure	0.5 Pa
Source Bias (RF)	500 W
Forward Bias (RF)	50 W
Expected Etch Rate	145 nm/ min

However, this recipe was optimized for use with plasma-enhanced chemical vapor deposition (PECVD) Si_3N_4. Although it would still likely provide the same etch quality with LPCVD Si_3N_4, its inclusion of CHF_3 comes with a drawback. The inclusion of a hydrogen-containing compound, such as CHF_3, allows for the formation of Si-H and N-H bonds, which are known to have a significant impact on the physical properties of Si_3N_4 [44, 45, 46, 47]. Eventually, the final recipe

Table 3.6: Si_3N_4 Vertical Etch (no CHF_3)

Parameter	Value
CF_4	50 sccm
O_2	5 sccm
Pressure	2.00 Pa
Source Bias (RF)	500 W
Forward Bias (RF)	25 W or 40 W

was found to produce smooth, vertical sidewalls. (See Fig. 3.18)

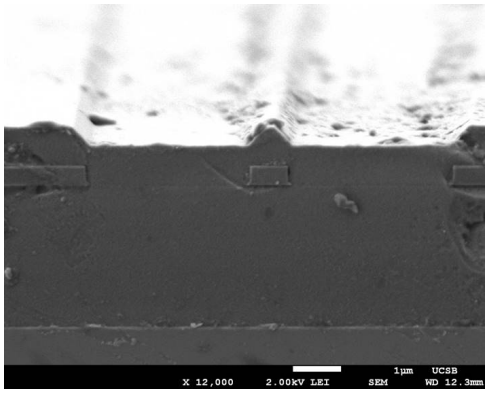

(a) SiO_2 cladding protects the waveguides from contamination.

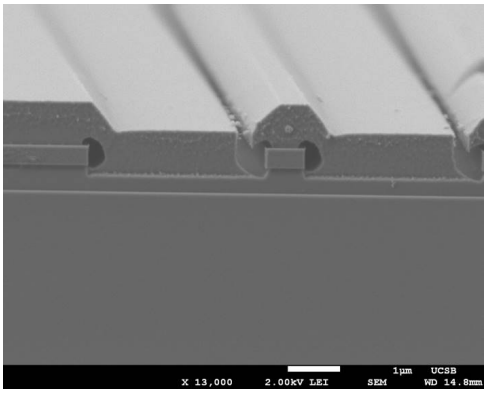

(b) Improper deposition can lead to folds in the cladding, which allow pathways for the vapor HF to the waveguides.

Figure 3.19: SEM images of the cladding deposition on 400 nm waveguides. Vapor HF is used to reveal the structure within the layers.

3.4 SiO_2 Cladding Deposition and Liftoff

In general, ultra-low loss Si_3N_4 waveguides are usually covered in SiO_2 to match the thermally grown SiO_2 beneath them. This cladding both improves the optical quality of the waveguides and protects the waveguides from particles post-fabrication. For these reasons, we clad the waveguides over a majority of the sample, only blocking the deposition in the region of our devices. The edge of the cladding layer intersects the waveguides at a 45° angle, as seen in Fig. 3.20, to reduce potential reflections issues.

An SiO_2 RF-Sputtering recipe had already been optimized for photonic applications by Mike Davenport (Ph.D. 2017) working under John Bowers. The remaining parameters to be determined were the height/tilt configuration of the source and substrate. Typically, lower angles of incidence are preferred when doing lift-off processes. However, uniformity and surface roughness are significantly more important for the later application of wafer bonding, covered in Chapter 4.

Eventually, the clean-room standard dual-liftoff recipe was modified sufficiently to allow the low-angle deposition of SiO_2 using RF-sputtering, resulting in the proper lift-

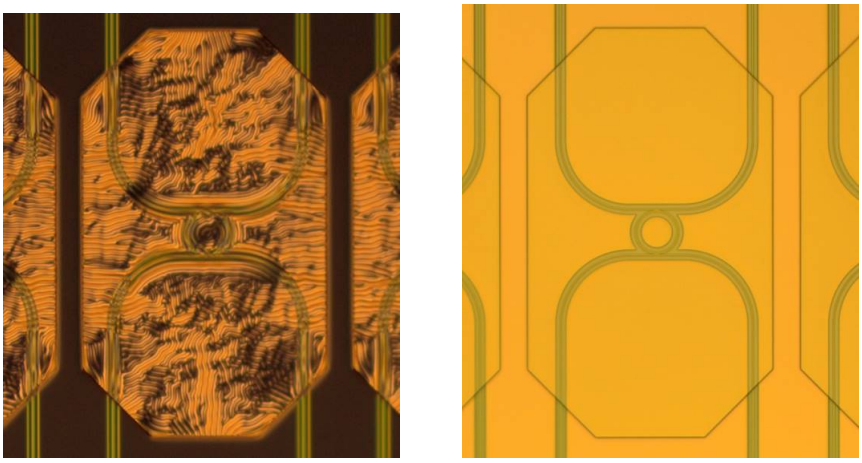

(a) After SiO_2 sputtering (b) After lift-off

Figure 3.20: An octagon-shaped patch of photoresist shields the ring resonators during the SiO_2 sputtering process.

off demonstrated in Fig. 3.20. The significance of this is demonstrated in Fig. 3.21, which compares the deposition uniformity for 3 hours sputtering depositions performed at the lowest and highest angle configurations. We see that the low angle configuration (a) exhibits approximately 10 nm variance from center to edge, whereas the high angle configuration (b) had 15 nm variance despite depositing only $^2/_3$ as much.

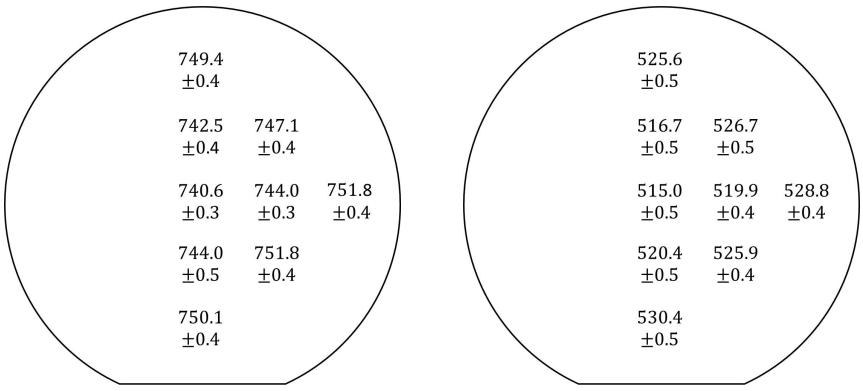

(a) $z = 2.75$ $h_\phi = 4\,\mathrm{mm}$ (b) $z = 1.52$ $h_\phi = 9\,\mathrm{mm}$

Figure 3.21: Layer thickness for 2 different height/tilt configurations on Sputter 3, for 3 hour deposition time.

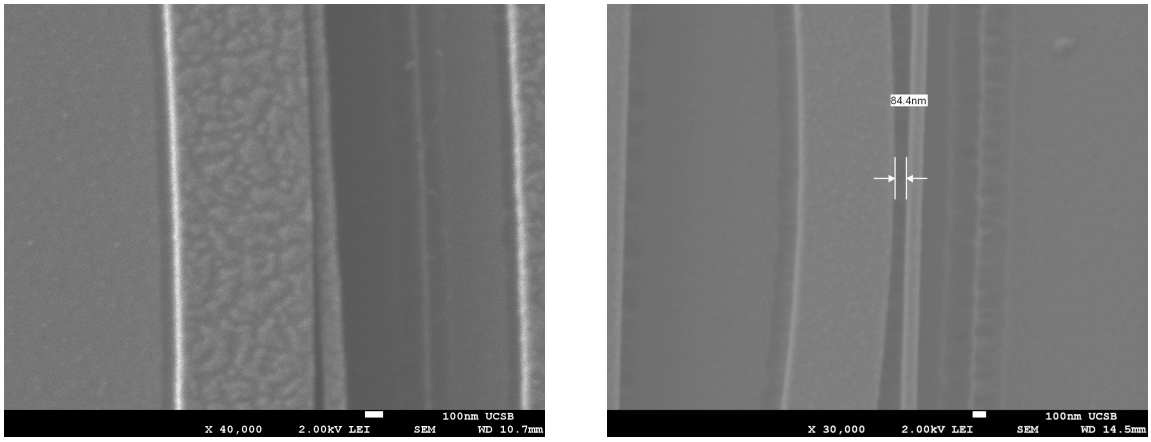

(a) Stiction will occur with 'snap-release' nanobeams when wet processing is done following the release of the mechanical structures.

(b) Vapor HF can be used to release Si_3N_4 nanobeams without stiction occurring.

Figure 3.22: Stiction can be avoided with a vapor HF etch instead of a standard wet release, making 'snap-release' nanobeams possible using the SiO_2 as a sacrificial layer.

3.5 Release of Mechanical Structures with Vapor HF Dry Etching

Our mechanical structures are released by removal of the SiO_2 layer beneath them. The most common removal technique for sacrificial SiO_2 layers is wet etching with diluted or buffered HF solutions. The chemical process for such reactions is:

$$SiO_2(s) + 4\,HF(aq) \xrightarrow{H2O} 2\,H_2O + SiF_4(g) \tag{3.3}$$

However, wet releases are problematic when the released structures are in close proximity to other objects. The surface tension of water will pull mechanically released objects toward their nearest neighbors, which can cause them to adhere together even after the water is fully removed. This problem is referred to as 'stiction' (static friction), and comes from the inability of the mechanical structure to surpass the threshold required to overcome the Van der Waals force between the two structures. Fig 3.22 shows an

example of stiction encountered in our samples encountered after wet processing.

A common solution to this problem is critical point drying, which solves the surface tension issue by going around the liquid-gas phase transition boundary, rather than across it. This means the mechanical structures never encounter a physical liquid-gas boundary as the liquid is converted to a gas, However, the critical point drying apparatus in our cleanroom is unreliable. According to the logbook, valve failures tended to ruin approximately 1 in 5 runs.

A relatively new option is the use of a dry HF vapor process, which uses gaseous HF instead of liquid HF to etch the SiO_2 layer. The UC Santa Barbara cleanroom obtain an STPS uEtch Vapor HF system in 2013, which utilizes the reaction:

$$SiO_2(s) + 4\,HF(g) \xrightarrow{EtOH} 2\,H_2O + SiF_4 \tag{3.4}$$

In this process, we see that ethanol (EtOH) is used to catalyze the reaction instead of H_2O. A problem arises in that H_2O is a product of the reaction. If this water is not removed from the system sufficiently, its ability to catalyze the reaction via Eq. 3.1 will interfere with the etch rates. For this reason, each etch is usually broken up into a number of shorter etches to avoid complications from the buildup of water over a single etch cycle.

We are restricted to 5 base recipes with our vapor HF system.

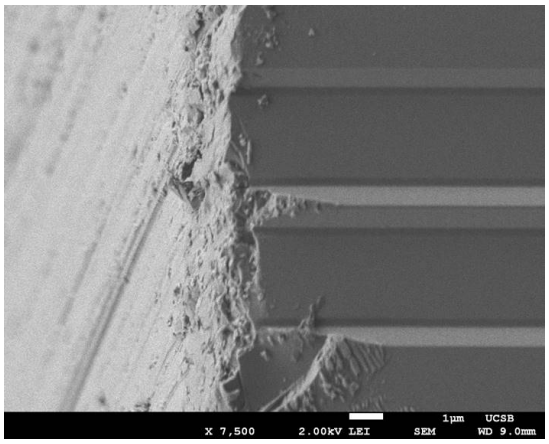

(a) After dicing, the roughness of the sample edges leads to high scattering loss.

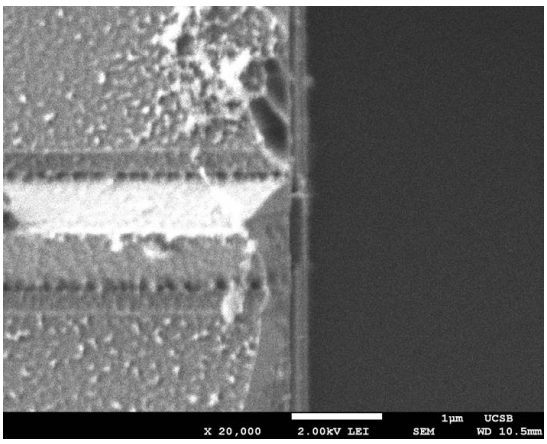

(b) Proper polishing yields a smooth waveguide facet for light insertion after vapor HF to release the SRNBs.

Figure 3.23: Facet polishing is critical in reducing insertion loss when coupling light into and out of the optical waveguides. The images here are for non-wafer bonded samples, to be used with the vacuum setup described in Section 5.4.2.

3.6 Dicing and Facet Polishing

Each full sample is diced into 6 functional device pieces and 2 test pieces (See Fig. 3.10) using a 100 µm wide dicing saw blade.[3] Following the dicing process, there is approximately $40 - 50$ µm thickness between the outer encapsulation layer and the start of the optical waveguides. This needs to be polished and smoothed to reduce insertion loss of the lensed fibers, yet not overly so such that the waveguides get exposed and the wafer bonding process will not be able to form a seal. Noting that our lensed fibers have a focal length of 14 µm in vacuum, the ideal width of the encapsulation layer is in the range of $10 - 20$ µm. To achieve this, polishing films of grade 6 µm, 1 µm, 0.3 µm, and 'final polish' are used in order from coarsest to finest. Only one sample bar is polished at a time to avoid complications that arise from variance in the diced widths of the bars.

[3]If the sample is not to be waferbonded, it is instead diced with a 200 µm wide to ensure the waveguide facets are exposed. All 6 samples can then be diced together, we a seventh piece of material to be used a shield in front of them.

Chapter 4

Anodic Wafer Bonding

To further improve our integrated design, we attempt to hermetically seal our system under transparent glass (Borofloat-33) at pressures on the order of 10^{-6} mbar. This serves two functions:

1. It allows for room temperature characterization of high-$\mathcal{Q}$ mechanical devices without the use of a vacuum chamber.

2. It protects our devices from foreign contaminants after they leave the cleanroom environment, without taking any special precautions. This is significant as the presence of a single particle near an optical ring is sufficient to render it unusable.

The fact that this can be done with transparent material is invaluable in preserving the simplicity of our alignment procedure.

This short chapter covers the basics of anodic bonding, its standard limitations, and how we get around them for our particular devices.

4.1 Bonding Chemistry and Procedure

Using specific borosillicate glasses, anodic bonding is already an effective technique for obtaining hermetically sealed regions for the fabrication of microsensors [48, 49, 50]. Borosilicate glass was developed in the late 1800s by melting together B_2O_3, Al_2O_3, SiO_2 (silica), and Na_2CO_3 (soda ash). The resulting glass contains approximately 4% Na_2O by weight, which is the 'active ingredient' in anodic bonding. Borosilicate glass is 90% transparent for wavelengths up to 2 µm, and has a coefficient of thermal expansion (CTE) very similar to silicon. This is important for both the wafer bonding process, which goes up 400 °C, as well as for later cryogenic cooling of the sample. Borofloat-33 is simply borosilicate glass manufactured using a 'floating' technique that produces very uniform and flat surfaces [51], necessary for wafer bonding.

Usually anodic bonding is done with direct contact between borosillicate glass and p-doped silicon. By pressing the glass into the Si wafer, heating them up to > 400 °C, and applying a negative voltage from the glass to the Si, O^{2-} ions in the glass and positively charged holes in the p-doped Si are dragged to the glass-Si interface. The strong electric field pulls the two materials together, where the O^{2-} ions are then able to form Si-O covalent bonds with the Si substrate. This bond is known to be strong and hermetic, and occur when the glass and Si are initially within 1 µm of each other [50].

When the borosilicate glass and Si wafer do not come directly into contact with each other, the bond can still occur, but larger electric fields across the boundary are necessary, requiring a larger voltage [52]. However, for SiO_2 layers greater than 600 nm the bond can no longer happen [53]. Since we necessarily need at least 2 µm of SiO_2 between the LPCVD Si_3N_4 and the Si substrate, we cannot directly wafer bond to the top of our layer stack. To solve this problem, we deposit a conductive layer around the insulating layer, with a liftoff layer protecting our devices. A thin layer of amorphous-Si (α-Si) is

sputtered on the topside of the conductive layer, which the borosilicate glass is able to bond to. The full bonding process then works as follows:

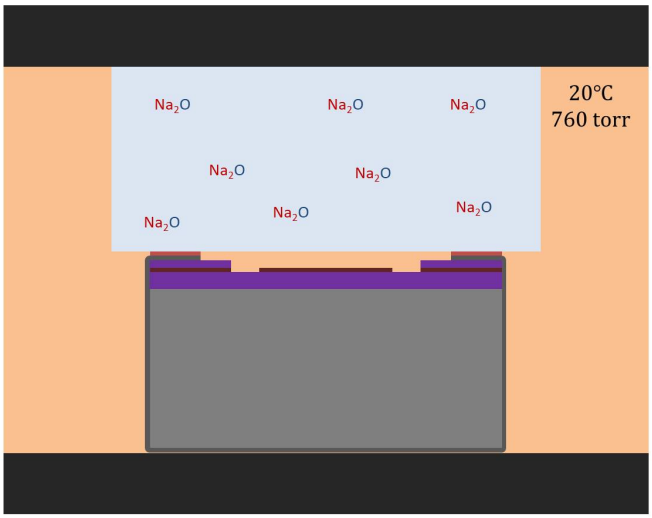

Figure 4.1: **(Step 1)** The borosilicate glass is placed on top of the sample, then loaded into the vacuum bonder.

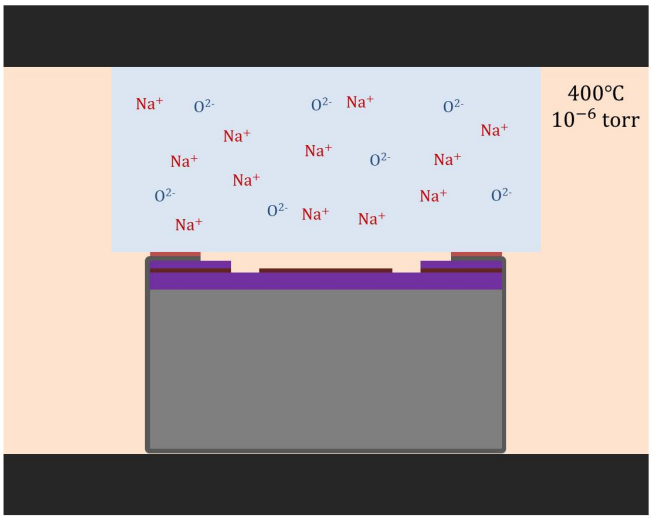

Figure 4.2: **(Step 2)** The system is pumped down to 2×10^{-6} mbar, and heated to 400 °C. At 400 °C, the Na_2O dissociates into Na^+ and O^{2-} ions.

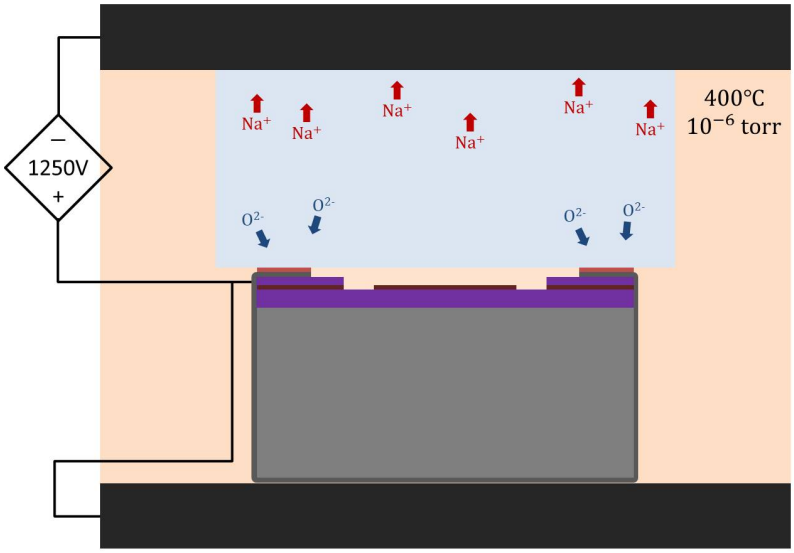

Figure 4.3: **(Step 3)** A negative voltage is placed across the device. This drives the Na^+ ions to the cathode and the O^{2-} toward the conductive material that is shorted to the anode.

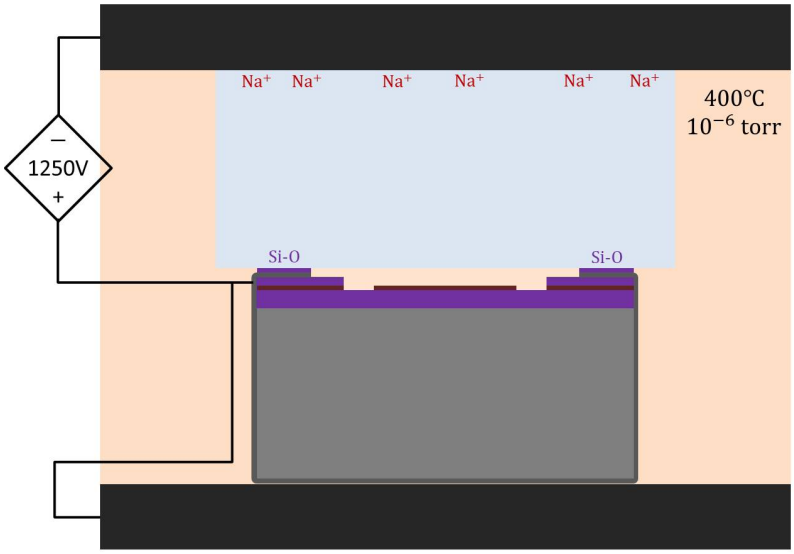

Figure 4.4: **(Step 4)** Covalent Si-O bonds form at the interface between the α-Si and the Borofloat glass.

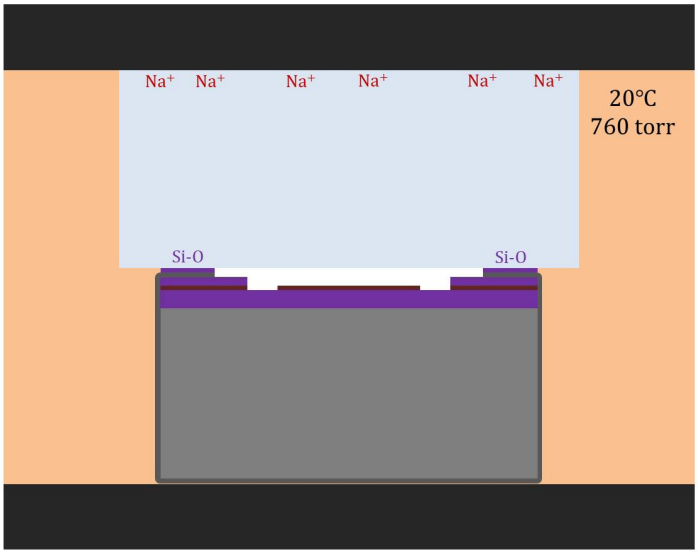

Figure 4.5: **(Step 5)** The sample is allowed to cool and return to atomspheric conditions, to be diced and polished. As the seal is known to be strong and hermetic, the device regions do not return to atmospheric pressure.

Although the UCSB NFF is equipped with a vacuum bonder, it need not be the case that original bonding actually be done in vacuum. Options exist which allow for non-vacuum bonding to yield a hermetically sealed vacuum pockets. A hole can be left in the glass that connects the device region to the outside environment. By depositing over that hole in a low pressure environment, one is able to obtain pressures in the sealed chamber approximately matching the deposition pressure. Such an idea could also be used to fix any small leaks on the edge of a sample. A getter can be placed inside the sealed region in addition to this process to obtain vacuum pressures [54].

A final option to consider is the addition of a cryopump region using a material such as activated charcoal. This could allow the sealed region to obtain ultra-high vacuum pressures inside the seal when the sample is later cooled to cryogenic temperatures [55].

4.2 Material Selection

The success of the anodic bonding process is dependent on the correct choice of materials for the layers which connect the α-Si bonding layer to the top of the SiO_2 cladding. These layers must include a relatively thick conductive material that is capable of distributing the electric potential across the entire sample. The primary criteria for deciding on a layer stack are:

- **Surface Roughness/Uniformity** Both long-scale and short-scale uniformity are important factors in determining whether the bond succeeds, and whether vacuum pressure will remain stable after the sample is diced and polished.

- **Adhesion Between Layers:** Every deposited material must strongly adhere to the material below it. The friction generated during the dicing and polishing steps is enough to pull weakly bonded layers apart from each other.

- **Coefficient of Thermal Expansion (CTE):** The sample will need to be heated to >400 °C during the bonding process, and potentially cryogenically cooled to mK temperatures. This necessitates that the layers have comparable CTEs to minimize the stress undergone during temperature changes. This primarily relates to the necessary conductive layer, as most metals have a CTE an order of magnitude greater than Si, SiO_2, and Si_3N_4.

- **Method of Deposition:** The conductive layer needs to be deposited in such a way that the insulating SiO_2 and Si_3N_4 are 'shorted' by the material. This necessitates deposition on at least one edge of the sample, in addition to the top layer. This is possible with multiple depositions or one single one that covers both the top and at least one edge. Strategies using both Sputtering (DC and RF) and electon beam physical vapor deposition (EBPVD) are explored in Sect. 4.3.

Taking these points into account, we use the strategy to restrict ourselves to silicon based compounds (Si, SiO_2, and Si_3N_4) with the exception of our conductive layer. The RF-sputtering of Si is the single most uniform process in the UCSB cleanroom (Brian Thibeault, personal communication), thus taking care of all 4 bullet points with respect to each other. The primary nuance thus becomes choosing an appropriate conductive layer that fits in the middle. The top candidates are the refractory metals: niobium, molybdenum, tantalum, tungsten, and rhenium. Refractory metals are know to have high melting points and low CTEs, on the same order of silicon. This leads to them being extremely resistant to heat, corrosion, and wear. They are also known to be good electrical conductors. The CTEs of the refractory metals, and some other possible candidates, are shown in Table 4.1.

Table 4.1: CTE for Relevant Materials

Material	CTE @ 300 K ($\frac{\mu m}{m}K^{-1}$)
Device Materials:	
Silicon (crystaline)	2.69 [32]
Silicon (amorphous)	4.4 [56]
SiO_2	0.5 – 1.0 [57, 58]
Si_3N_4	3.4 [31]
Borosilicate Glass	3.3 [59]
Refractory Metals:	
Tungsten	4.5 – 4.6
Molybdenum	4.8 – 5.1
Rhenium	6.2 – 6.7
Tantalum	6.5 – 6.6
Niobium	7.0 – 7.3
Other Metals of Interest:	
Chromium	4.9 – 8.2
Titantium	8.4 – 8.6
Platinum	8.8 – 9.1

Note: Data for the metals was obtained from Barron(1980)[60] and Cverna(2002)[61].

4.3 Method of Deposition

Two methods of deposition are used:

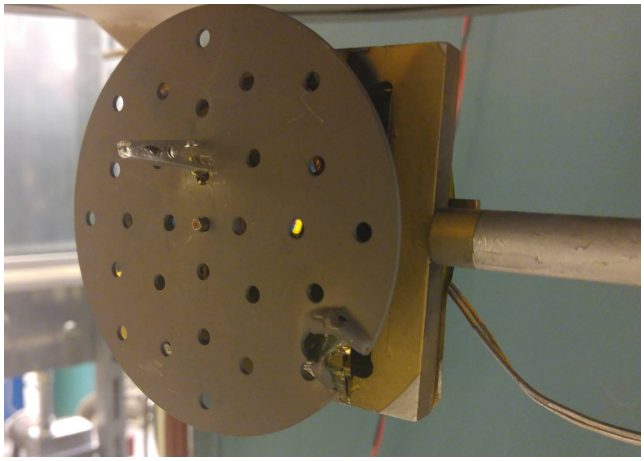

Figure 4.6: Electron Beam Chemical Vapor Deposition (EBCVD) is normally very unidirectional. However, by rotating the sample around one of its planar axes, we are able to coat the front, back, and multiples sides with a single deposition. The sample is clamped by an alligator clip attached to a chuck, which is rotated by a motor connected to electrodes inside the EBCVD vacuum chamber.

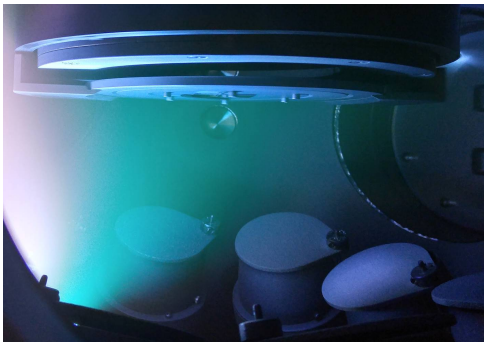

(a) Although the sputtering process is directional, deposition occurs at an angle by machine construction.

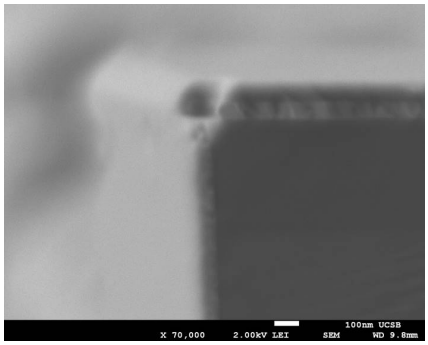

(b) DC-sputtering of tungsten deposits a sufficient amount of conductive material on the edge.

Figure 4.7: By design, the sputter machines deposit at an angle. For low angles of deposition, the sputtering process deposits enough material on its sides for the dielectric layers to be shorted.

4.4 Results

The standard metrics by which wafer bonding is evaluated are the 'eye' test and 'pull' test [62, 63, 53]. The initial bonding of the glass layer to the Si layer is very evident by visual inspection. Unbonded layers display a typical interference pattern that is sensitive to touch or pressure on the top surface. Bonded layers tend to have a very dull appearance. However, even if the two top layers successfully bond, the true test for anodic bonding is the ability for the whole layer stack to withstand a pulling force. Proper wafer bonding produces bond strengths equal to or greater than the fracture strengths of the glass itself. As such, the pull test will fail at the glass level rather than at the interface for a successful anodic bond.

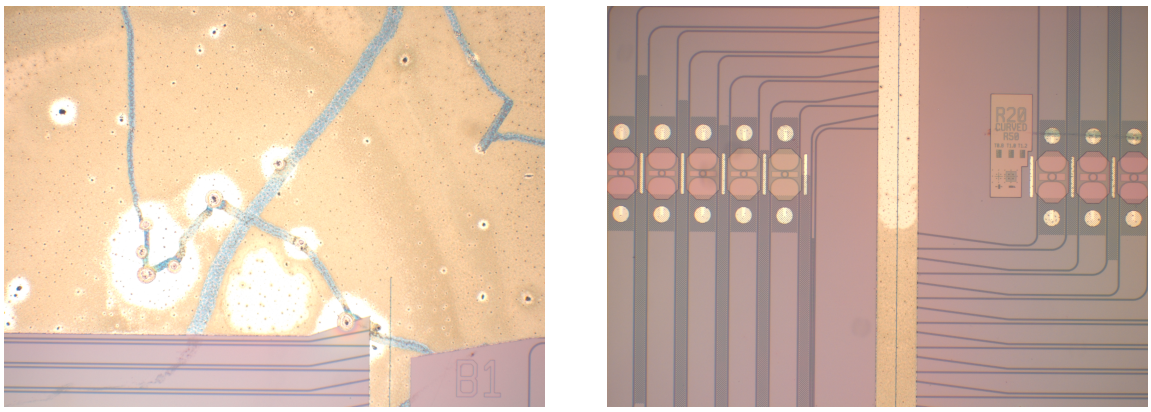

(a) Particles and residues will prevent successful bonding. The appearance around the particles is indicative of the lighter regions corresponding to unsuccessful bonding.

(b) Evidence of failed bonding in the critical region between the ring arrays. If this sample were diced, the unsuccessful bonding on the top would lead to penetration of the vacuum region by air and/or water.

Figure 4.8: Microscope images from a failed anodic bond attempt. Dark regions correspond to successful bonding.

4.4.1 Aluminum

Although aluminum was not on the list of materials with a compatible CTE, it was a good test choice for the EBCVD shown on the previous page. It is known to be sufficiently conductive and smooth, unlike many other metals deposited through EBCVD. As shown in Fig. 4.9a, aluminum was able to conduct sufficiently for the bonding process to work, though higher voltages were required than usual (1500 V instead of 400V). However, visual inspection of the sample afterwards clearly indicated that something had occurred near the top layers, as it had changed from the standard grey appearance of aluminum to a brownish color. Inspection under a microscope suggested that one of the layers had cracked, most likely either the aluminum or the α-Si. A repeat test of the thermal conditions without the Borofloat slide led to the brown appearance, with the top flaking off. From this we concluded that the Al had expanded significantly to shatter the α-Si layer on top of it, which has a coefficient of thermal expansion an order of magnitude below it.

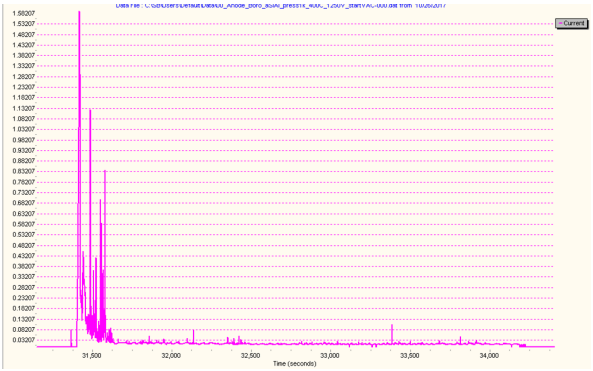

(a) Plot of current vs. time during the anodic bonding using an aluminum conductive layer. A particularly high voltage (1500 V) was necessary to complete the bond.

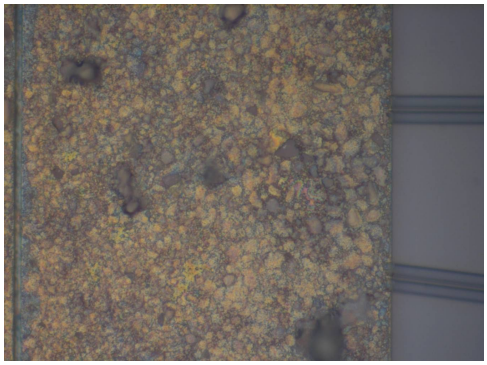

(b) Microscope image of the bonding region after the removal from the vacuum bonder, and successful pull test. The α-Si is shattered by the expansion of the aluminum underneath it.

Figure 4.9: Although aluminum passes the pull test, it very clearly fails the eye test. The difference in CTE between aluminum and the other materials ultimately resulting in the aluminum layer 'bursting' out from the α-Si material above it.

4.4.2 Tantalum

Tantalum seems like the strongest candidate to be successful conductive layer for our wafer bonding scheme. Buchwalter et al. (1995)[64] showed that the adhesion of tantalum to silicon nitride is superior to tantalum to silicon oxide or chromium to either material. It was also the only material combination that resulted in material failure from a pull test, rather than at the interface. This suggests that we should use RF-sputtered SiN inbetween our SiO_2 cladding and our Ta layer, as well as between the Ta layer and the α-Si layer. As an additional possible resource, tantalum nitride (TaN) can be used as a glue between conductive materials [65]. A third potential (long-term) benefit is that Ta is a Type-I superconductor with a relatively high critical temperature. The paves the way for the conductive layer to have other potential purposes, such as driving the nanomechanical oscillator after cryogenic cooling.

Based on the findings of Buchwalter[64], the following layer stack recipe was developed:

Table 4.2: Ta Layer Stack

Step #	Thickness	Layer Deposition
4	60 nm	RF–sputtered α-Si coating
3	10 nm	RF–sputtered SiN coating
2	50 nm	DC–sputtered Ta
1	10 nm	RF–sputtered SiN coating
0	-	SiO_2 cladding

where all 4 layers above the cladding are to be deposited in a single run without breaking vacuum.

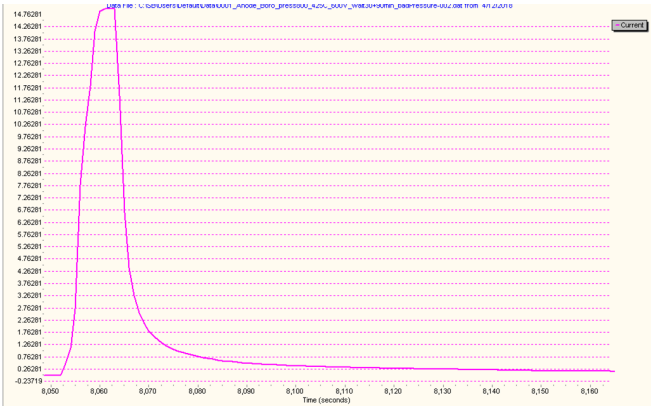

(a) A nearly ideal current profile for anodic bonding.

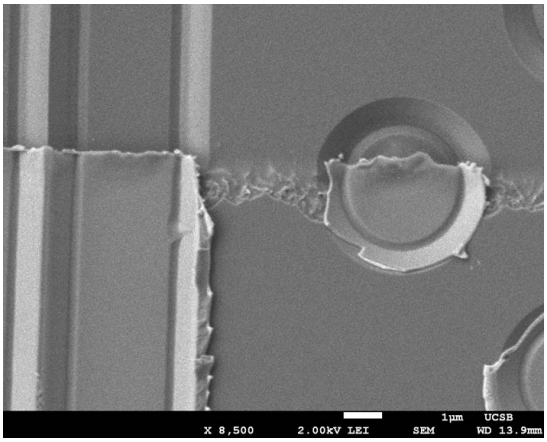

(b) Layer separation after completion of the bonding process.

Figure 4.10: Although the SiN/tantanlum/SiN/Si stack demonstrated a successful anodic bond, adhesion of the layers resulted in a failure of the process. Postmortem analysis revealed separation between the Ta layer and the bottom RF-sputtered SiN layer. However, the adhesion between the top SiN layer on the Ta was good.

The resulting stack proved to be very effective for the anodic bond process, as shown in Fig. 4.10a. The current ramps up to 15 mA, the maximum allowed by the bonder. After most of the sample is bonded, the current draw finally drops below 15 mA and begins to decay exponentially over time. Unfortunately, retrieval of the sample from the bonding machine resulted in separation between the Borofloat-33 glass and the Si wafer. The top wafer bonding pattern had transferred completely from the Si piece to the Borofloat. As shown in Fig. 4.10b, SEM imaging revealed separation had occurred between the Ta layer and the RF-sputtered SiN layer beneath it.

These initial results are counter to the findings of Buchwalter [64]. After discussion with cleanroom staff, we came to conclusion that it is most likely the case that the sputtered SiN is too smooth for the adhesion of Ta. As mentioned, the RF-sputtering of Si, SiO, and SiN are the single smoothest and most uniform depositions in the UCSB NFF. This minimizes the surface area over which the Ta can adhere to during the deposition

process. Buchwalter suggests that the adhesion of Ta to SiN is driven by:

$$Si_3N_4 + 4\,Ta \longrightarrow 4\,TaN + 3\,Si \tag{4.1}$$

which is thermodynamically feasible. That is to say, the reaction is not strongly favored, but will happen spontaneously given enough time [64].

Rather than wait for TaN to form on the surface between the interaction between SiN and Ta, it would seem advantageous to simply deposit the Ta in a nitrogen atmosphere, which on its own leads to the formation of TaN [66]. By modifying the layer stack to:

Table 4.3: Proposed tantalum stack for wafer bonding

Step #	Thickness	Layer Deposition
5	60 nm	RF–sputtered α-Si coating
4	10 nm	RF–sputtered SiN coating
3	50 nm	DC–sputtered Ta
2	5 nm	RF–sputtered TaN
1	10 nm	RF–sputtered SiN coating
0	-	SiO_2 cladding

we expect the adhesion issues to be fixed. This is to be explored upon the reception of a new set of Borofloat wafers.

4.4.3 Tungsten

After determining aluminum's non-viability and before experimenting with the tantalum layer stack, we attempted to use DC-sputtered tungsten between SiO_2 cladding and the α-Si. As can be seen in Fig. 4.11, W was successful as a conductive layer for the bond process. However, it failed the pull test afterwards, with the interface between the SiO_2 and the tantalum being the obvious point of failure. A testing of the dicing process through the center of the devices (unharmed by the pull test) resulting in delamination along the dicing line, resulting in water flooding the device region.

We originally concluded that W would not work as a conducting layer. However, after the results of the tantalum layer, there is reason to second-guess the original conclusion. Tungsten nitride is a known conductor, and could potentially be used instead of pure tungsten in future tests.

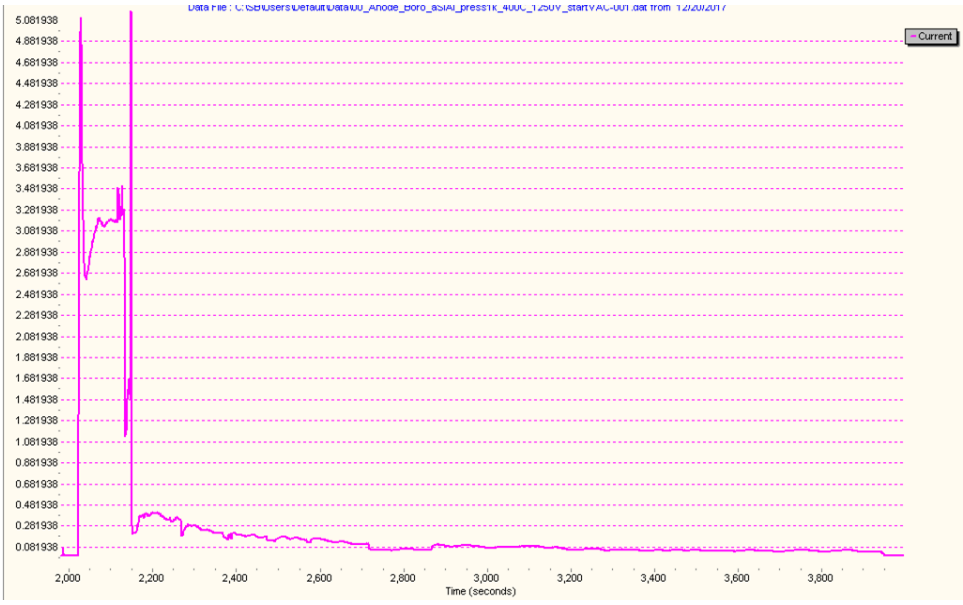

Figure 4.11: Plot of current vs. time during the anodic bonding process for a W conductive layer. Although it does not match the ideal form observed with tantalum in Fig. 4.10, the strong and continuous pull of current is indicative of a successful bond.

Chapter 5

Device Characterization and Preliminary Results

In this chapter, we characterize samples made using the fabrication techniques in Chapter 3 and compare them to predictions of Chapter 2. First, we discuss both general and specific features of the optical setup used to characterize our samples at room temperature and pressure. Results of optical and optomechanical characterization are then be analyzed. We then compare these results to those obtained from a vacuum setup constructed by Wolfgang Löffler at Leiden University. Finally, we compare the obtained results to theoretical predictions from Chapter 2. Equations and ideas are repeated and referenced when possible for the reader who jumped directly to this chapter.

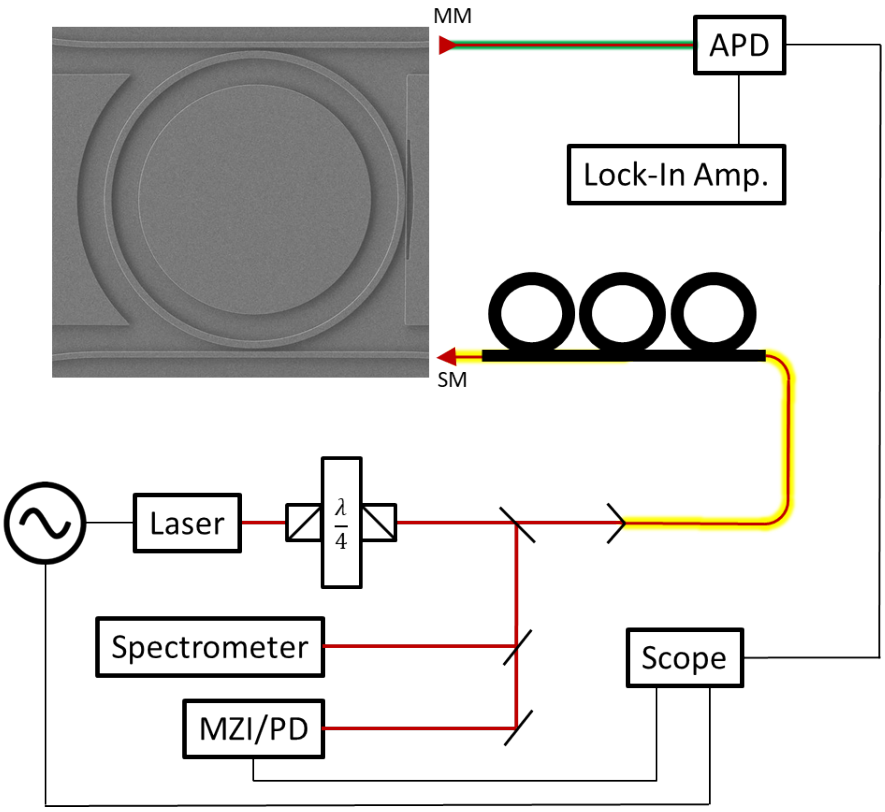

Figure 5.1: Diagram of the optical setup

5.1 Optical Setup

A layout of our basic optical setup is shown in Fig. 5.1.

1. Our laser source is a Sacher Lasertechnik Litmann class tunable diode laser, model TEC-500-1060-030, operated by an Sacher MLD-1000 modular laser driver. Installed in the MLD are the *Laser Controller*, *Piezo Amplifier & Current Coupling*, and *Ramp Generator* modules, which together allow for scanning the laser with 0–100 V, with a piezo tuning rate of 1.3 GHz/V. Mode-hop-free tuning ranges of ~ 10 GHz can be obtained around most resonances, sometimes with a fair amount of current adjustment needed. The full range of the laser is 990–1075 nm, but we generally aim to stay around the operational wavelength of 1060 nm. The laser is

usually operated with currents of 100–130 mA, outputting 10-15 mW of power.

2. Light from the laser aperture passes through a Thorlabs IO-D-1064-VLP optical isolator, which transmits approximately 60% of the power.

3. A 90/10 beamsplitter picks off 10% of the light for analysis. The transmitted 90% is coupled to a single-mode fiber using a coupler with 5 degrees of freedom. The reflected 10% is further separated by a 99/1 beamsplitter. The transmitted 99% is sent to a Mach-Zender Interferometer to look for modehops. The reflected 1% is sent to a spectrometer to keep track of the wavelength.

4. The single mode fiber is connected a 1 m long lensed fiber, which is threaded through a standard manual fiber polarization controller utilizing stress-induced birefringence.

5. The lensed fiber is aligned with the input waveguide using an overhead CCD camera to monitor light scattered in the waveguides, and from the throughput port.

6. After tuning the laser frequency until a the ring is on resonance, light is collected from the drop port with a multi-mode lensed fiber.

7. The multi-mode fiber is fed into a Thorlabs APD110C avalanche photodetector with a bandwidth of 50 MHz.

8. The APD is connected to an oscilloscope and a Zurich HF2LI lock-in amplifier for spectral analysis.

5.2 Ring Resonators

The first step in the development of our process was obtaining high-finesse optical ring resonators, and understanding how their coupling, optical $\mathcal{Q}$s, and finesse vary as a function of their geometry. Since our FSRs are much greater than the mode-hope free range of our laser, we are restricted to measuring the $\mathcal{Q}$-factors and estimating the finesse from the predicted FSRs. This essentially reduces our goal to optimizing the ratio of $\mathcal{Q}$ to R.

5.2.1 Optical Quality Factors

Optical quality factors are characterized by scanning the laser over the resonance of the ring, and fitting the resulting photodiode voltage to a Cauchy Distribution. A quicker method is simply determining the full-width half maximum of the resonance by tuning the laser voltage directly, then dividing the laser frequency by it. This latter method is good for spot-checking if there is something wrong with a ring, without having to fully characterize it.

The development of the chromium etch mask process, detailed in Section 3.3, was primarily driven through optical $\mathcal{Q}$ measurements. Despite being on the low side, the initial $\mathcal{Q}$s were very promising when taking the apparent sidewall roughness into context. For visibly rough sidewalls, $\mathcal{Q}$s were obtained in excess of 3×10^5, indicating ~ 1 db/cm propagation loss (Fig. 1.6). Images of similar sidewalls and the resulting $\mathcal{Q}$s are shown on the next page.

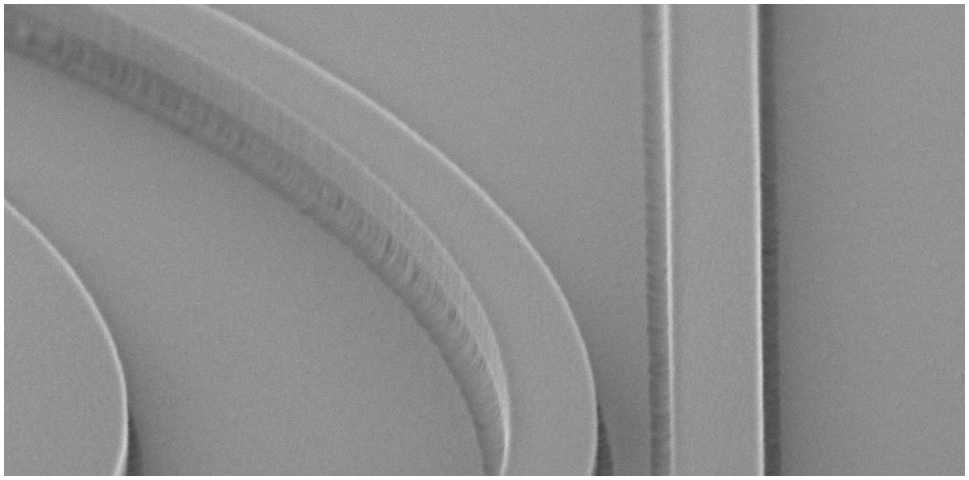

Figure 5.2: Images of sidewall roughness taken around the time of sample Loss Test 4A (LT4A), whose measured optical quality factors are given in the tables below.

Table 5.1: Loss Test 4A R16

Ring Width	Coupling Split 300 nm	500 nm	700 nm
0.8 µm	35	60	145
1.0 µm	40	-	152
1.2 µm	45	100	153

Table 5.2: Loss Test 4A R25

Ring Width	Coupling Split 300 nm	500 nm	700 nm
0.6 µm	-	50	-
0.8 µm	45	76	-
1.0 µm	67	161	179
1.2 µm	-	200	333

Table 5.3: Loss Test 4A R50

Ring Width	Coupling Split 300 nm	400 nm	500 nm	600 nm
0.8 µm	43	86	143	-
1.0 µm	57	125	157	250
1.2 µm	100	150	231	273

With the optimization of the thermal reflow of the UV6 photoresist (Section 3.3.1), the quality factors increased towards being limited by coupling for the lower coupling distance values.

Table 5.4: Loss Test 10A R16

$R = 16\,\mu m$ $w = 800\,nm$	Coupling Split		
	300 nm	500 nm	700 nm
L10A Fabricated	70	340	600 ± 100
OMNISIM (Fig. 2.9)	76	865	$\sim 10^7$

which is consistent with internal $\mathcal{Q}s$ on the order of 6×10^5.

Following these results, full attention was put toward the detection of an optomechanical signal. Loaded optical $\mathcal{Q}s > 10^5$ were considered sufficient enough for the start of optomechanics. This meant all samples were processed with vapor HF, which generally roughened up the surface. Additionally, the APD was a necessary replacement for the low-speed InGaAs amplified photodetector that we were using, which cut our signal by a factor of 5. As such, obtaining measurements for the 500 nm coupling splits became essentially impossible, as well as a second priority. This led to us being generally coupling limited:

Table 5.5: Outside Bridge 15, width = 800 nm

Ring Radius	Coupling Split	
	300 nm	400 nm
16 nm	72	136
20 µm	80	192
24 µm	82	208
32 µm	77	178
40 µm	90	257

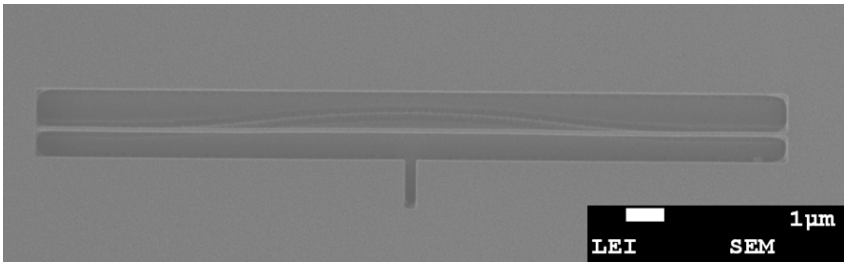

(a) Successful 20 µm SRNB with $\delta x = 500\,\text{nm}$ and $R_{curv} = 50\,\mu\text{m}$

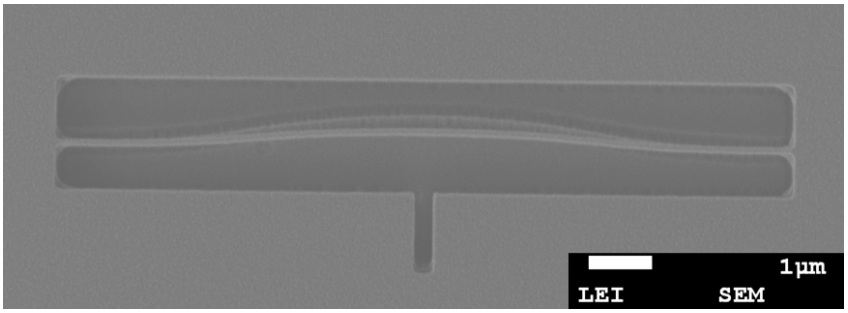

(b) Failed 12 µm SRNB with $\delta x = 500\,\text{nm}$ and $R_{curv} = 16\,\mu\text{m}$.

Figure 5.3: Subset of the original SRNB tests, comparing successful (a) and failed (b) releases. Patterns were entirely defined by E-beam lithography

5.3 Snap-Release Nanobeams

The snap-release mechanism was experimentally tested before the "theory" of Section 2.2.1.4 was penned out. It was simply an idea written with E-Beam Lithography, at the edge of a sample to be undercut with vapor HF. The initial results are shown in Fig. 5.3. It was only later that Eq. 2.49:

$$\Delta\sigma = E\frac{\delta L}{L} = -\frac{1}{6}\frac{\delta x}{R_{curv}}E \tag{2.49}$$

was derived, which explains the results. Both nanobeams shown have $\delta x = 500\,\text{nm}$, which is around the minimum distance required for the fabrication of the nanobeam to be independent from its surroundings. However, the failed bridge had $R_{curv} = 16\,\mu\text{m}$ in order to yield a 12 µm long bridge. Eq. 2.49 predicts this releases 1460 MPa of tensile stress, more than the assumed 1140 MPa available. With an $R_{curv} = 16\,\mu\text{m}$, the

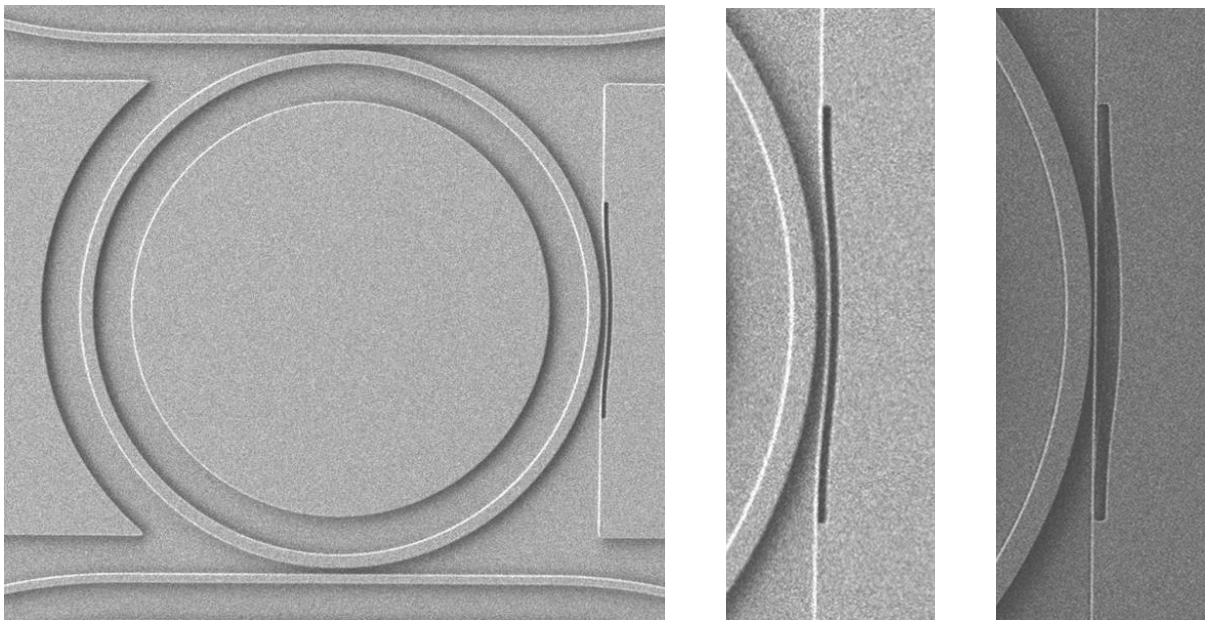

(a) Optical ring resonator geometry after E-beam Lithography to define the SRNB on the right side.

(b) pre-vHF

(c) post-vHF

Figure 5.4: Demonstration of the release of a 'snap-release' nanobeam to yield a nanomechanical resonator in close proximity to an optical ring resonator.

other bridge only releases 467 MPa of stress, leaving more than enough to remain in the high-stress regime after being pulled straight. Longer SRNBs were also tested (with $\delta x = 500\,\text{nm}$), and all of them pulled straight as one would expect given the model.

The SRNB design was implemented into our mask design to create the *ThickRings_v2* Mask, detailed in App. A. As shown in Fig. 5.4, the 'template' ring geometries have the inner bending of SRNBs patterned into the Cr mask, with δx and R_{curv} set for each device. E-beam lithography is then used to modify the chromium hard mask, defining the width and length dimensions of the SRNB. Using this technique, we can fabricate SRNB with length only limited by the fabrication geometry (slightly less than $2\times$ the ring radius with the present mask design), and with optomechanical splits $\sim 50\,\text{nm}$. Smaller optomechanical splits should be obtainable by tweaking the exposure/reflow parameters of the initial 'template' to enlarge the geometry. The width of the SRNBs appears to be

limited to approximately 50 nm (Fig. 5.6). Thinner nanobeams likely fail due to forces exerted upon them by the fabrication process (e.g. resist spinning).

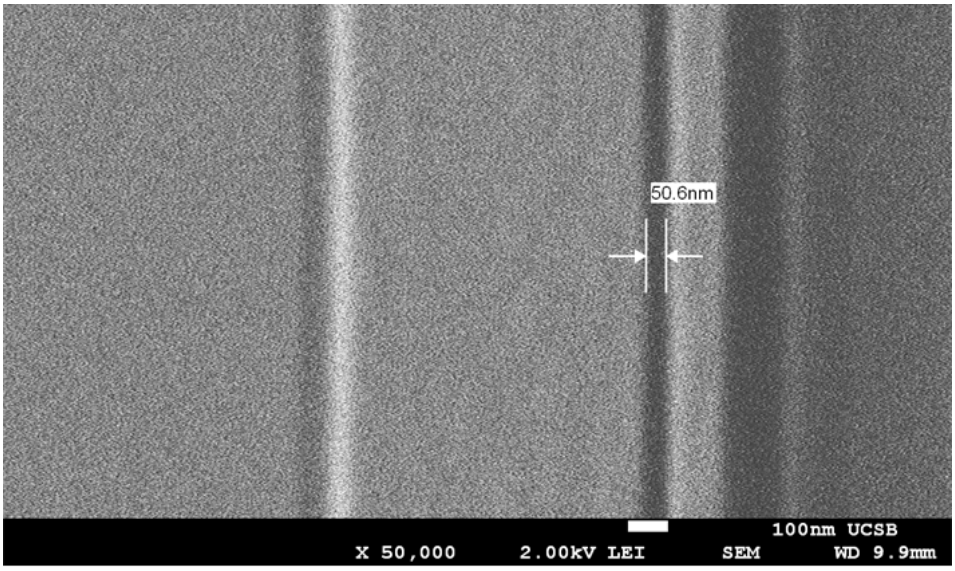

Figure 5.5: Optomechanical coupling splits on the order of 50 nm were obtained using our SRNB fabrication process.

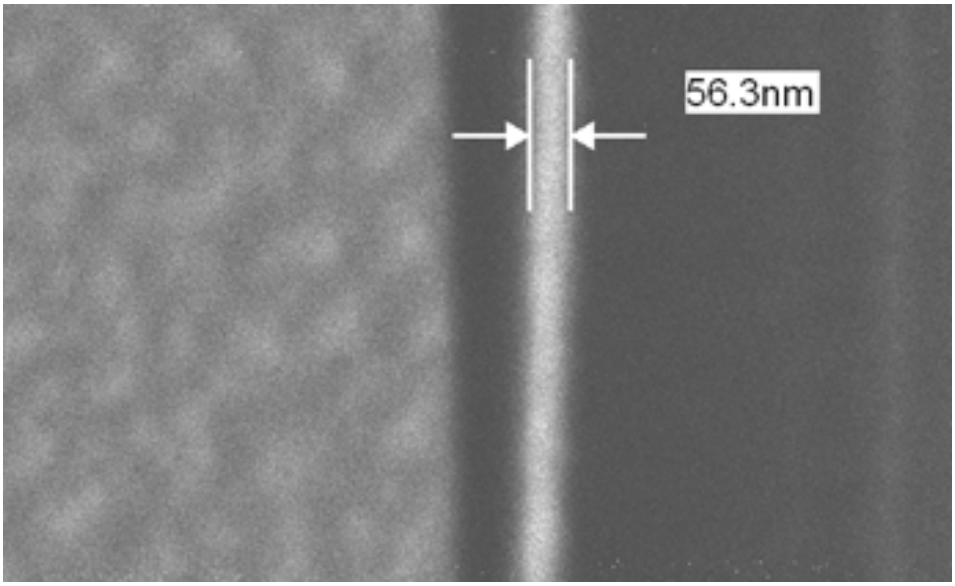

Figure 5.6: The thinnest SRNBs obtained were on the order of 60 nm wide.

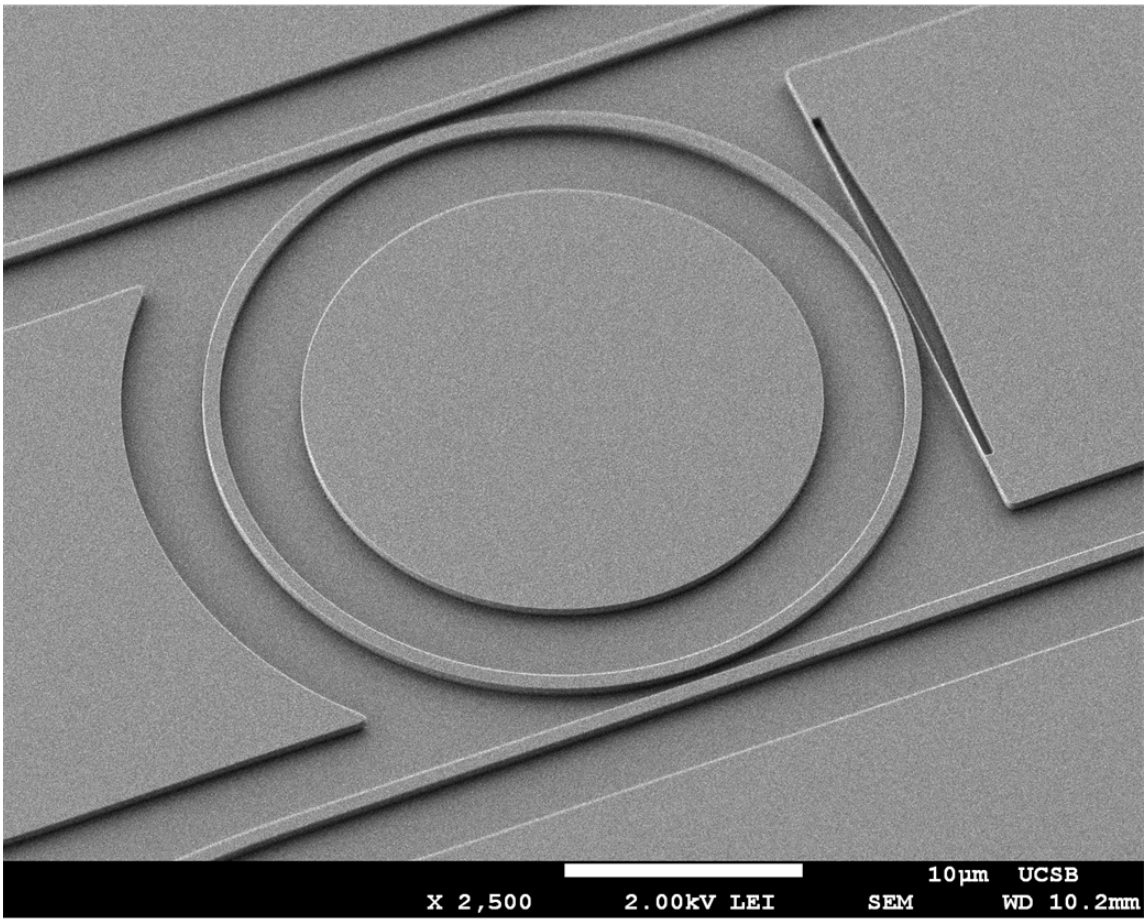

Figure 5.7: SEM image of a 16 µm radius optical ring resonator with a 20 µm long SRNB.

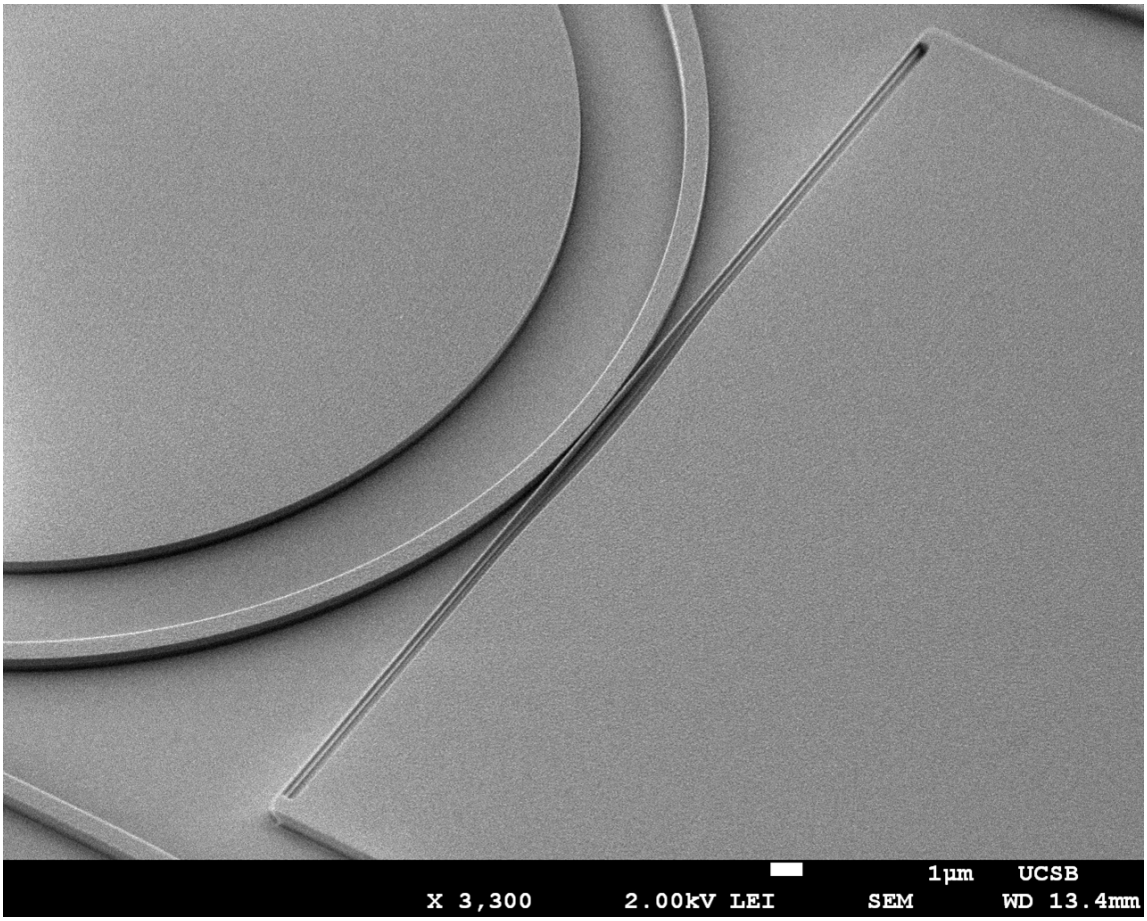

Figure 5.8: SEM image of a 24 µm radius optical ring resonator with a 40 µm long SRNB.

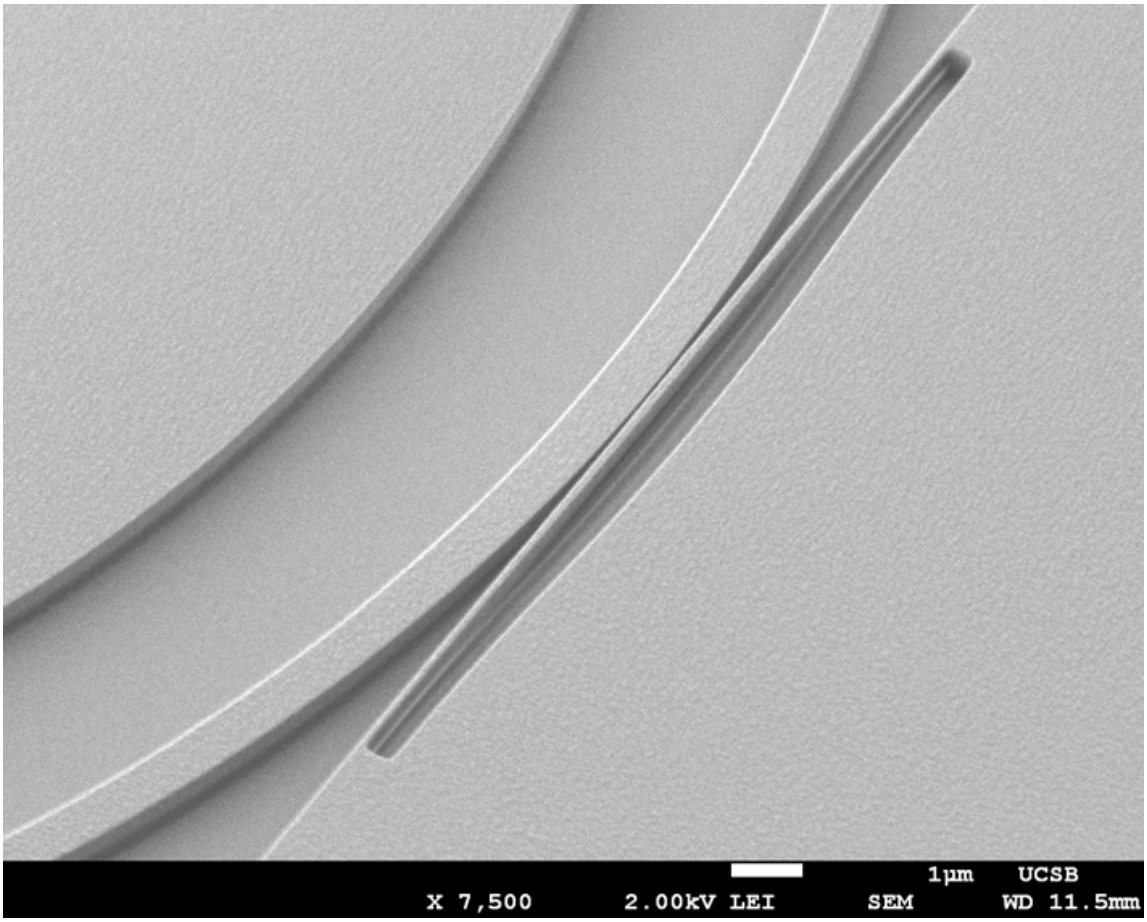

Figure 5.9: SEM image of one of the shorter SRNBs coupled to a relatively large optical ring resonator ($R = 40\,\mu\text{m}$).

5.4 Detection of Optomechanical Coupling

Optomechanical coupling is detected by analyzing the noise spectrum of the drop-port signal using a Zurich HF2LI lock-in amplifier. Due to the presence of the nanomechanical resonator, the resonant frequency of the optical ring resonator is modulated by f_m as the effective index is changes with the position of the oscillating nanomechanical resonator. This shifts the detuning of the laser with respect to cavity, resulting in the power transmission (and thus photodetector voltage) also being modulated by f_m. By mixing the photodetector voltage with a reference frequency f_r, we obtain new signals at $f_s \pm f_r$. By applying a low-pass filter after the mixing, only when $f_s \sim f_r$ do we get signal above noise.

5.4.1 Atmospheric Measurements

Using the optical setup in Section 5.1, optomechanical coupling between optical ring resonators and SRNBs was detected at room temperature and pressure. The HF2LI picked up broad noise peaks in the MHz range on the blue detuned side of 2 optical resonances, shown in Fig. 5.10. Each optical resonance corresponded to a distinct SRNB geometry. The ~ 9 MHz and ~ 13 MHz resonances were found on devices D6i and D5i, respectively. From fitting the noise spectra of Fig. 5.10 to Cauchy distributions (Fig.

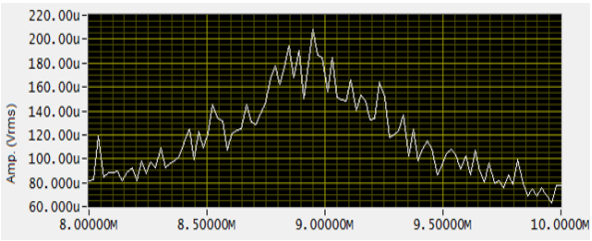

(a) $L = 20\,\mu\text{m}$, $\delta x = 500\,\text{nm}$, $R_{curv} = 50\,\mu\text{m}$

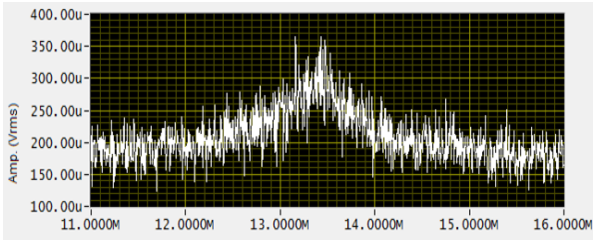

(b) $L = 16\,\mu\text{m}$, $\delta x = 300\,\text{nm}$, $R_{curv} = 32\,\mu\text{m}$

Figure 5.10: Raw optomechanical signals from the Zurich HF2LI for OB5-D5i and OB5-D6i, respectively

5.11), we get:

Table 5.6: SRNB Parameters, and Measured

Device	L	δx	R_{curv}	f_m (MHz)	$\mathcal{Q}_{atm}$
OB5-D5i	16 µm	300 nm	32 µm	13.39 ± 0.03	20.5 ± 5.5
OB5-D6i	20 µm	500 nm	50 µm	8.93 ± 0.02	15.9 ± 2.6

The low $\mathcal{Q}$s are expected. In Section 2.2.2.2, we obtain:

$$\mathcal{Q}_m \approx 1.85 \cdot \left[\frac{f}{1\,\text{MHz}}\right] \cdot \left[\frac{1.01 \times 10^5\,\text{Pa}}{P}\right] \left[\frac{t}{100\,\text{nm}}\right] \tag{2.104}$$

for room temperature. From SEM images taken of the OB5 sample, the approximate post-release width of the SRNBs was ~ 75 nm. From Eq. 2.104, this leads to estimated atmospheric $\mathcal{Q}$s of 18.5 and 12.4 for D5i and D6i respectively. The measured $\mathcal{Q}$s agreed quite reasonably with these predictions.

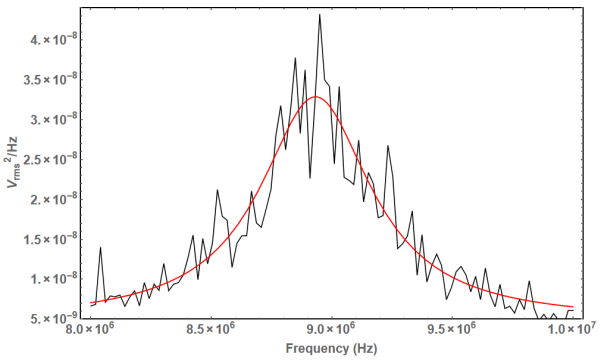

Figure 5.11: OB5-D6i optomechanical signal taken at atmospheric pressure. Fit to a Cauchy Distribution gives $\mathcal{Q}_m = 15.9 \pm 2.6$

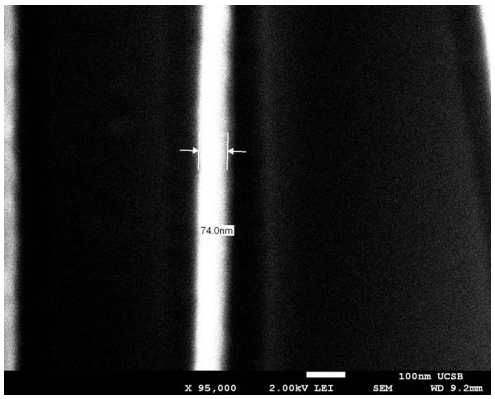

Figure 5.12: SEM image of an SRNB from OB5-D5 array, giving an approximate width of 75 nm.

As discussed in App. A, the D5 ring array is special in that it the only set with $\delta x = 300\,\text{nm}$ instead of 500 nm. This means its the length of its snap-release section is 12.7 µm long instead of 16.0 µm. As such, we use the generalized stress-release equation:

$$\Delta\sigma = \frac{1}{6} E \frac{\delta x}{R_{curv}} \frac{L_{SR}}{L} \tag{2.51}$$

where L_{SR} is the length of the snap release region, and L is the total length. Along with our derived equation for the fundamental frequency (from Section 2.2.1.3):

$$f_1 = \frac{1}{2L}\left(\frac{\sigma - \Delta\sigma}{\rho}\right)^{1/2}\left[1 - \left(\frac{w}{L}\right)\sqrt{\frac{E}{3\left(\sigma - \Delta\sigma\right)}}\right]^{-1} \tag{2.55}$$

we are able to compare our measured frequencies with predictions:

Table 5.7: Comparison of measured frequencies to model values

	OB5-D5i	OB5-D6i
$\sigma_0 = 1140$ MPa	16.65 MHz	11.95 MHz
$\sigma_0 = 830$ MPa	13.27 MHz	8.91 MHz
Measured	13.39 MHz	8.93 MHz

We see immediately that our estimated frequencies are over 25% higher than measured when assuming an initial stress of 1140 MPa. However, our values agree very well if we assume an initial stress of 830 MPa. This value is more consistent literature values of stress in LPCVD Si_3N_4 [67, 24, 20]. It is most likely the case that the quoted value of 1140 MPa corresponds to a thin film stress measurement, and our thicker Si_3N_4 layer has less stress.

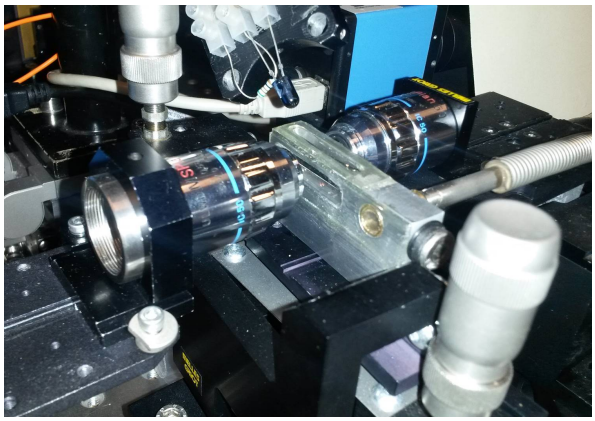

(a) Each sample is encapsulated in the metal structure, with transparent glass windows on each side.

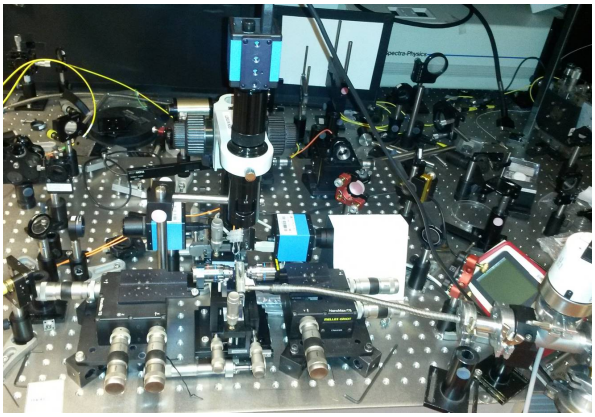

(b) The metal chamber is connected to a vacuum pump for controlling the pressure.

Figure 5.13: Image of the optical setup at Leiden University. It is functionally equivalent to Fig. 5.1, but high magnification lens are used to focus the laser source light onto the input facet, as well as collimate light from the drop port onto the photodiode.

5.4.2 Vacuum Measurements

Following measurement of the low $\mathcal{Q}_m$ values in the previous section, two strategies were taken to measure $\mathcal{Q}_m$ at low pressures. The first was the vacuum wafer bonding process discussed in Chapter 4, which at this time has not successfully led to low-pressure $\mathcal{Q}_m$ measurements. The second method involves the more conventional strategy of aligning the sample in a vacuum system. Images of the design, built at Leiden University by Wolfgang Löffler, are shown above in Fig. 5.13. The vacuum apparatus consists of a machined metal chamber with hermetically sealed glass windows (Fig. 5.13a), and a vacuum pump connected to the chamber. Besides these differences, the setup is functionally equivalent to the setup shown in Fig. 5.1, but with the lensed fibers replaced by actual lens (microscope objectives).

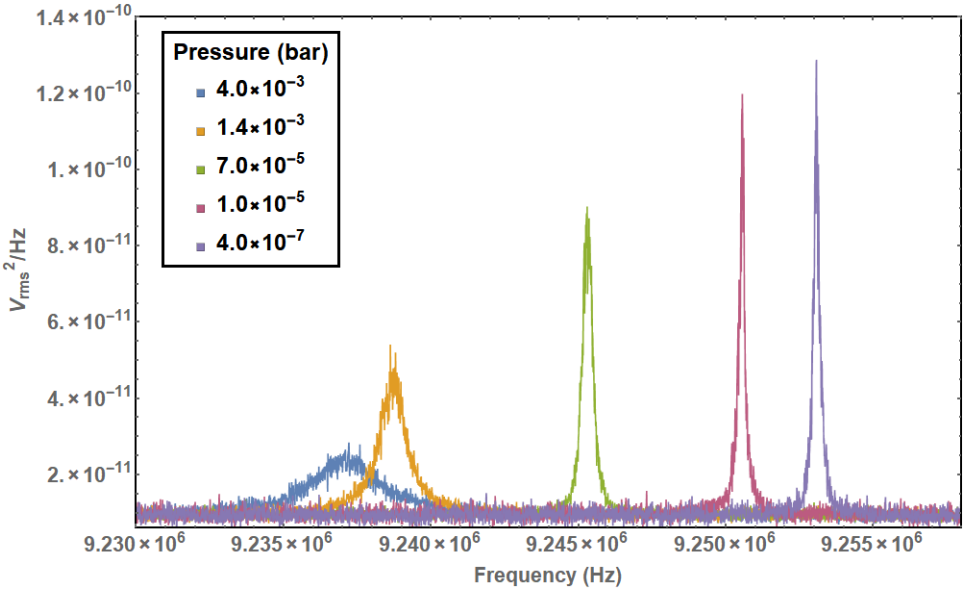

Figure 5.14: Measurement of the optomechanical interaction as a function of pressure, obtained using the vacuum setup shown on the previous page. This data is collected on device OB19B-D6e (fabricated April 26, 2018).

Measurements of optomechanical coupling for varying environmental pressure are shown in Fig. 5.14. As expected, $\mathcal{Q}_m$ shows a strong dependence on pressure. The change in resonance frequency as a function of pressure does not correspond to the damped frequency $\omega^2 = \omega_0^2(1 - \frac{1}{4Q^2})$, though it is in the right direction. Although the cause is unknown, this is a commonly observed dependency with Si_3N_4 nanomechanical resonators.

The data in Fig. 5.14 is collected from sample Outside Bridge 19B, device D6e (fabricated April 26, 2018). SEM images of the exact device suggest the width of the SRNB is approximately 100 nm. Using the estimated stress of 830 MPa, the frequency predicted by Eq. 2.55 would match the measured values for an SRNB width of 110 nm, which would certainly fall within the resolution error of the SEM.

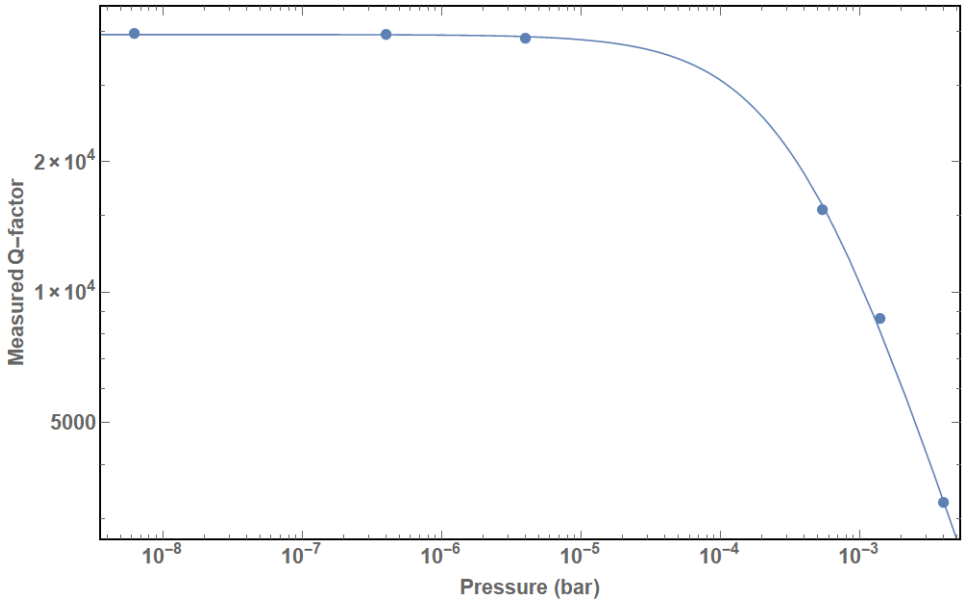

Figure 5.15: Measured $\mathcal{Q}$ values as a function of gauge pressure. Fitting the data to Eq. 5.1 estimates the mechancal quality factor to be $\mathcal{Q}_{mech} = 39300 \pm 500$, with the predicted $\mathcal{Q}_m$ at atmosphere to be $\mathcal{Q}_{atm} = 14.4 \pm 0.9$.

As discussed at the end of in Section 2.2.2.2, we expect the measured qualtiy factor $\mathcal{Q}_m$ as a function of pressure to behave as:

$$\mathcal{Q}_m = \left(\frac{1}{\mathcal{Q}_{mech}} + \frac{1}{\mathcal{Q}_{atm}} \left[\frac{P}{1 \text{ bar}} \right] \right)^{-1} \tag{5.1}$$

where $\mathcal{Q}_{mech}$ is the intrinsic quality factor of the SRNB and $\mathcal{Q}_{atm}$ is the measured quality factor at atmospheric temperature and pressure. Fitting the OB19B data (Fig. 5.1) yields $\mathcal{Q}_{mech} = 39300 \pm 500$ and $\mathcal{Q}_{atm} = 14.4 \pm 0.9$. The $\mathcal{Q}_{atm}$ is consistent with the predictions of Section 2.102, as well as the atmospheric results from the previous section.

In Section 2.2.2.1, our model eventually predicted the intrinsic quality factor $\mathcal{Q}_{mech}$ would be given by:

$$\mathcal{Q}_{mech} = \left[(j\pi)^2 \left(\frac{L_s}{L - 2L_s} \right)^2 + 2 \frac{L_s}{L - 2L_s} \right]^{-1} \mathcal{Q}'_{\text{Si}_3\text{N}_4} \tag{2.100}$$

where $\mathcal{Q}'_{\mathrm{Si_3N_4}} \approx 8500$. Assuming a final stress of $\sigma = 830$ MPa - 470 MPa = 360 MPa, and a width of 100 nm, Eq. 2.100 predicts $\mathcal{Q}_{mech} \approx 9.5 \cdot \mathcal{Q}'_{\mathrm{Si_3N_4}} \approx 80000$. This is approximately a factor of 2 larger than our measured $\mathcal{Q}_{mech}$. The most likely cause of the deviation is surface roughness on the sides of our SRNBs, though more data is necessary before being able to make any definitive conclusions.

This page intentionally left blank.

Conclusion

The groundwork has been laid for a fully-integrated optomechanical system, combining the established platform of optical ring resonators with our novel 'snap-release' nanobeams. The framework for predicting the behavior of each component of the system is established in Chapter 2. This includes FEM simulations and an analytic model for predicting mechanical parameters, as well as photonic simulations for the optical and optomechanical parameters. The characterization of a complete fabrication process is presented in Chapter 3. Finally, in Chapter 5, we present preliminary results demonstrating the viability of both the fabrication process and the predictive models.

With the exception of the intrinsic quality factor from the vacuum sample, which was off by a factor of 2, the measured physical properties of the SRNBs were in strong agreement with the stress-release model presented in Section 2.2.1.4, assuming an initial stress in the material of $\sigma_0 = 830$ MPa. The agreement with the model is significant in that it suggests the SRNBs are well-behaved with respect to the 'snap-release' mechanism. That is to say, there do not to be any catastrophic consequences for releasing the stress in this manner.

With a working model to understand the system to high-precision, it is already possible to imagine applications for such an integrated design. To start, parametric modification of the nanobeams can give you important information about the material itself, such as the tensile stress, film density, and Young's Modulus. Standard methods for

obtaining these values include the fabrication of released microsctructures and fitting to models. However, here we are probing the effect of Young's modulus in the most direct way possible - by modifying the length of the material itself. And since we are using an integrated photonic design, we can fabricate 100s of SRNBs on a single sample, and move waveguide to waveguide collecting the frequency of each SRNB (with an average alignment time on the order of a minute when moving between adjacent waveguides).

Beyond measuring its own properties, released SRNBs can potentially be utilized as sensors. For example, one can imagine 2 ring/SRNB systems coupled to the same waveguide in such a way that the SRNBs oscillate perpendicular to each other. In this configuration each SRNB can act as an accelerometer, with the position of each SRNB shifting the resonance frequency of its respective ring as accelerating forces displace each beam. Thus, from a single optical waveguide one can sense acceleration along 2 orthogonal directions through simple monitoring of near-resonant signals.

In any case, it is clear that this project is still in its infancy. There are still many things to understand about the system, and many avenues towards improving the fabrication process. Nevertheless, the preliminary results give cause for optimism of this new design. With further optimization, this integrated system could join the list of cavity optomechanical devices capable of probing the quantum mechanics of macroscopic objects.

Appendix A

Organization of ThickRings_v2 Mask

The mask consists of 36 sets of 12 resonators, organized in a 6×6 array. Each set is identified by a letter (column) and number (row), with A1 corresponding to the upper left set. Individual resonators within a set are designated by a lowercase letter, 'a'–'l', with 'a' being the first ring from the left. As such E4 would correspond to the device set in the 4th row of the 5th column of the mask, and E4d would be the fourth resonator within that set.

A.1 Primary Devices: Columns A,B,C,D,E

The first 4 columns, A–D, follow a strict structure. Column E varies slightly:

- Each column corresponds to ring resonators of a specific radius. The radii are 16 µm(A), 20 µm(B), 24 µm(C), 32 µm(D), and 40 µm(E).
- Row 1 consists of rings with no optomechanical coupling region. They represent the base case for us to compare to the effects of each implemented optomechanical coupling region.

- Rows 2–4 correspond to different splits between each ring resonator and a flat mechanical structure. The coupling splits (and row numbers) are 300 nm(2), 400 nm(3), and 500 nm(4).

- Rows 5 and 6 have 'curved coupling regions,' designed so that release of the mechanical structure allows the tensile stress to bring the mechanical structure closer to the ring resonator. Row 5 corresponds to a radius of curvature of 32 µm , which has a minimum bridge length of 16 µm ($\approx$ 13 MHz). Row 6 corresponds to a radius of curvature of 50 µm, which has a minimum bridge length of 20 µm ($\approx$ 9MHz).

- Within every set of rings, the only varying parameters are the optical coupling splits and the thickness of the ring waveguides.

- Within each 12 ring set, only the ring waveguide thickness and coupling split vary. The ring radius and mechanical structure and coupling remain the same. This table shows the coupling split and ring thickness pattern within each set of rings:

	Ring Waveguide Thickness		
Coupling Split	800 nm	1000 nm	1200 nm
300 nm	a	e	i
400 nm	b	f	j
500 nm	c	g	k
600 nm	d	h	l

A.2 Extra Devices: Columns 6

The 6th column, F, does not follow the previous rules. Column F is meant to allow for comparison between variations in the electron beam lithography. As such, it primarily consists of rings with identical parameters. The general rules for column F are as follows:

- F1–F3 have rings with radii of 16 µm. F4–F6 have rings with radii of 24 µm.
- F1 is identical to A2. F4 is identical to C2. (For these two rows, each ring is actually distinct.)
- F2 and F5 are similar to rows A6 and C6, but the thickness of every ring waveguide is 800 nm. Hence, the following triplets are of identical rings: (a, e, i), (b, f, j), (c, g, k), and (d, h, l), with their respective coupling splits being 300 nm, 400 nm, 500 nm, and 600 nm.
- Every resonator in F3 is identical to A6b, and every resonator in F6 is identical to C6b. That is, each has a thickness of 800 nm and a coupling split of 400 nm.

This page intentionally left blank.

Bibliography

[1] R. Penrose, *On Gravity's role in Quantum State Reduction*, *General Relativity and Gravitation* **28** (may, 1996) 581–600.

[2] R. Penrose, *On the Gravitization of Quantum Mechanics 1: Quantum State Reduction*, *Foundations of Physics* **44** (may, 2014) 557–575.

[3] J. D. Jackson, *Classical Eletrodynamics*. Wiley, 1999.

[4] R. Penrose, *Gravitational Collapse of the Wavefunction: An Experimentally Testable Proposal*, in *The Ninth Marcel Grossmann Meeting*, pp. 3–6. World Scientific Publishing Company, dec, 2002.

[5] M. Aspelmeyer, T. J. Kippenberg, and F. Marquardt, *Cavity optomechanics*, *Reviews of Modern Physics* **86** (dec, 2014) 1391–1452.

[6] W. Marshall, C. Simon, R. Penrose, and D. Bouwmeester, *Towards Quantum Superpositions of a Mirror*, *Physical Review Letters* **91** (sep, 2003) 130401.

[7] J. Kepler, *De cometis libelli tres*, .

[8] E. F. Nichols and G. F. Hull, *A Preliminary Communication on the Pressure of Heat and Light Radiation*, *Physical Review (Series I)* **13** (nov, 1901) 307–320.

[9] R. A. Beth, *Mechanical Detection and Measurement of the Angular Momentum of Light*, *Physical Review* **50** (jul, 1936) 115–125.

[10] A. Ashkin, *Optical trapping and manipulation of neutral particles using lasers*, *Proceedings of the National Academy of Sciences* **94** (may, 1997) 4853–4860.

[11] B. P. Abbott et al., *Observation of Gravitational Waves from a Binary Black Hole Merger*, *Physical Review Letters* **116** (feb, 2016) 061102.

[12] B. P. Abbott et al., *GW170817: Observation of Gravitational Waves from a Binary Neutron Star Inspiral*, *Physical Review Letters* **119** (oct, 2017) 161101.

[13] R. A. Norte, J. P. Moura, and S. Gröblacher, *Mechanical Resonators for Quantum Optomechanics Experiments at Room Temperature*, *Physical Review Letters* **116** (apr, 2016) 147202.

[14] K. E. Khosla, G. A. Brawley, M. R. Vanner, and W. P. Bowen, *Quantum optomechanics beyond the quantum coherent oscillation regime*, *Optica* **4** (nov, 2017) 1382.

[15] M. J. Weaver, F. Buters, F. Luna, H. Eerkens, K. Heeck, S. de Man, and D. Bouwmeester, *Coherent optomechanical state transfer between disparate mechanical resonators*, *Nature Communications* **8** (dec, 2017) 824.

[16] L. F. Buchmann and D. M. Stamper-Kurn, *Nondegenerate multimode optomechanics*, *Physical Review A* **92** (jul, 2015) 013851.

[17] C. Galland, N. Sangouard, N. Piro, N. Gisin, and T. J. Kippenberg, *Heralded Single-Phonon Preparation, Storage, and Readout in Cavity Optomechanics*, *Physical Review Letters* **112** (apr, 2014) 143602.

[18] D. Kleckner and D. Bouwmeester, *Sub-kelvin optical cooling of a micromechanical resonator*, *Nature* **444** (nov, 2006) 75–78.

[19] D. Kleckner, B. Pepper, E. Jeffrey, P. Sonin, S. M. Thon, and D. Bouwmeester, *Optomechanical trampoline resonators*, *Optics Express* **19** (sep, 2011) 19708.

[20] M. J. Weaver, B. Pepper, F. Luna, F. M. Buters, H. J. Eerkens, G. Welker, B. Perock, K. Heeck, S. de Man, and D. Bouwmeester, *Nested trampoline resonators for optomechanics*, *Applied Physics Letters* **108** (jan, 2016) 033501.

[21] D. T. Spencer, J. F. Bauters, M. J. R. Heck, and J. E. Bowers, *Integrated waveguide coupled Si_3N_4 resonators in the ultrahigh-Q regime*, *Optica* **1** (sep, 2014) 153.

[22] K. Luke, A. Dutt, C. B. Poitras, and M. Lipson, *Overcoming Si_3N_4 film stress limitations for high quality factor ring resonators*, *Optics Express* **21** (sep, 2013) 22829.

[23] S. S. Verbridge, J. M. Parpia, R. B. Reichenbach, L. M. Bellan, and H. G. Craighead, *High quality factor resonance at room temperature with nanostrings under high tensile stress*, *Journal of Applied Physics* **99** (jun, 2006) 124304.

[24] Q. P. Unterreithmeier, T. Faust, and J. P. Kotthaus, *Damping of Nanomechanical Resonators*, *Physical Review Letters* **105** (jul, 2010) 027205.

[25] H. O. Pierson, *The CVD of Ceramic Materials*, in *Handbook of Chemical Vapor Deposition (CVD)*, pp. 265–294. Elsevier, 1999.

[26] W.-H. Chuang, T. Luger, R. Fettig, and R. Ghodssi, *Mechanical Property Characterization of LPCVD Silicon Nitride Thin Films at Cryogenic Temperatures*, *Journal of Microelectromechanical Systems* **13** (oct, 2004) 870–879.

[27] O. Tabata, K. Kawahata, S. Sugiyama, and I. Igarashi, *Mechanical property measurements of thin films using load-deflection of composite rectangular membranes*, *Sensors and Actuators* **20** (nov, 1989) 135–141.

[28] B. Halg, *On a nonvolatile memory cell based on micro-electro-mechanics*, in *IEEE Proceedings on Micro Electro Mechanical Systems, An Investigation of Micro Structures, Sensors, Actuators, Machines and Robots.*, pp. 172–176, IEEE.

[29] B. Hauer, C. Doolin, K. Beach, and J. Davis, *A general procedure for thermomechanical calibration of nano/micro-mechanical resonators*, *Annals of Physics* **339** (dec, 2013) 181–207.

[30] S. Schmid, K. D. Jensen, K. H. Nielsen, and A. Boisen, *Damping mechanisms in high-Q micro and nanomechanical string resonators*, *Physical Review B* **84** (oct, 2011) 165307.

[31] Y. Okada and Y. Tokumaru, *Precise determination of lattice parameter and thermal expansion coefficient of silicon between 300 and 1500 K*, *Journal of Applied Physics* **56** (jul, 1984) 314–320.

[32] N. Bouras, M. Madjoubi, M. Kolli, S. Benterki, and M. Hamidouche, *Thermal and mechanical characterization of borosilicate glass*, *Physics Procedia* **2** (nov, 2009) 1135–1140.

[33] S. Schmid and C. Hierold, *Damping mechanisms of single-clamped and prestressed double-clamped resonant polymer microbeams*, *Journal of Applied Physics* **104** (nov, 2008) 093516.

[34] K. Yasumura, T. Stowe, E. Chow, T. Pfafman, T. Kenny, B. Stipe, and D. Rugar, *Quality factors in micron- and submicron-thick cantilevers*, *Journal of Microelectromechanical Systems* **9** (mar, 2000) 117–125.

[35] W. E. Newell, *Miniaturization of Tuning Forks*, *Science* **161** (sep, 1968) 1320–1326.

[36] G. X. Li and H. G. Hughes, *Review of viscous damping in micromachined structures*, pp. 30–46, aug, 2000.

[37] S. Jennings, *The mean free path in air*, *Journal of Aerosol Science* **19** (apr, 1988) 159–166.

[38] S. S. Verbridge, R. Ilic, H. G. Craighead, and J. M. Parpia, *Size and frequency dependent gas damping of nanomechanical resonators*, *Applied Physics Letters* **93** (jul, 2008) 013101.

[39] M. Andrews and P. Harris, *Damping and gas viscosity measurements using a microstructure*, *Sensors and Actuators A: Physical* **49** (jun, 1995) 103–108.

[40] R. Christian, *The theory of oscillating-vane vacuum gauges*, *Vacuum* **16** (apr, 1966) 175–178.

[41] P. Li and R. Hu, *On the air damping of flexible microbeam in free space at the free-molecule regime*, *Microfluidics and Nanofluidics* **3** (oct, 2007) 715–721.

[42] B. E. E. Kastenmeier, P. J. Matsuo, J. J. Beulens, and G. S. Oehrlein, *Chemical dry etching of silicon nitride and silicon dioxide using CF 4 /O 2 /N 2 gas mixtures*, *Journal of Vacuum Science & Technology A: Vacuum, Surfaces, and Films* **14** (sep, 1996) 2802–2813.

[43] A. Nuottajärvi and T. Suppula, *Plasma Etching and Integration with Nanoprocessing*, pp. 251–263. 2009.

[44] M. Maeda and H. Nakamura, *Hydrogen bonding configurations in silicon nitride films prepared by plasmaenhanced deposition*, *Journal of Applied Physics* **58** (jul, 1985) 484–489.

[45] W. M. A. Bik, R. N. H. Linssen, F. H. P. M. Habraken, W. F. van der Weg, and A. E. T. Kuiper, *Diffusion of hydrogen in lowpressure chemical vapor deposited silicon nitride films*, *Applied Physics Letters* **56** (jun, 1990) 2530–2532.

[46] F. de Brito Mota, J. F. Justo, and A. Fazzio, *Hydrogen role on the properties of amorphous silicon nitride*, *Journal of Applied Physics* **86** (aug, 1999) 1843–1847.

[47] H. Jin, K. J. Weber, P. N. K. Deenapanray, and A. W. Blakers, *Hydrogen Reintroduction by Forming Gas Annealing to LPCVD Silicon Nitride Coated Structures*, *Journal of The Electrochemical Society* **153** (2006), no. 8 G750.

[48] G. H. Ko, W and T. Suminto, J and J. Yeh, *Bonding techniques for microsensors*, *Studies in Electrical and Electronic Engineering* **20** (1985).

[49] M. Esashi, N. Ura, and Y. Matsumoto, *Anodic bonding for integrated capacitive sensors*, in *[1992] Proceedings IEEE Micro Electro Mechanical Systems*, pp. 43–48, IEEE, 1992.

[50] S. A. Campbell, *Fabrication Engineering at the Micro- and Nanoscale*. Oxford University Press, 4th ed., 2013.

[51] Schott, "BOROFLOAT® 33 - Borosilicate glass."

[52] T. M. Lee, D. H. Lee, C. Y. Liaw, A. I. Lao, and I.-M. Hsing, *Detailed characterization of anodic bonding process between glass and thin-film coated silicon substrates*, *Sensors and Actuators A: Physical* **86** (oct, 2000) 103–107.

[53] J. Plaza, J. Esteve, and E. Lora-Tamayo, *Effect of silicon oxide, silicon nitride and polysilicon layers on the electrostatic pressure during anodic bonding*, *Sensors and Actuators A: Physical* **67** (may, 1998) 181–184.

[54] H. Henmi, S. Shoji, Y. Shoji, K. Yoshimi, and M. Esashi, *Vacuum packaging for microsensors by glass-silicon anodic bonding*, *Sensors and Actuators A: Physical* **43** (may, 1994) 243–248.

[55] D. M. Weld, J. Xia, B. Cabrera, and A. Kapitulnik, *New apparatus for detecting micron-scale deviations from Newtonian gravity*, *Physical Review D* **77** (mar, 2008) 062006.

[56] F. Jansen, M. A. Machonkin, N. Palmieri, and D. Kuhman, *Thermomechanical properties of amorphous silicon and nonstoichiometric silicon oxide films*, *Journal of Applied Physics* **62** (dec, 1987) 4732–4736.

[57] H. O. Pierson, *The CVD of Ceramic Materials*, in *Handbook of Chemical Vapor Deposition (CVD)*, pp. 295–322. Elsevier, 1999.

[58] J.-H. Zhao, T. Ryan, P. S. Ho, A. J. McKerrow, and W.-Y. Shih, *Measurement of elastic modulus, Poisson ratio, and coefficient of thermal expansion of on-wafer submicron films*, *Journal of Applied Physics* **85** (may, 1999) 6421–6424.

[59] P. J. Burkhardt and R. F. Marvel, *Thermal Expansion of Sputtered Silicon Nitride Films*, *Journal of The Electrochemical Society* **116** (1969), no. 6 864.

[60] T. Barron, J. Collins, and G. White, *Thermal expansion of solids at low temperatures*, *Advances in Physics* **29** (aug, 1980) 609–730.

[61] F. Cverna, *ASM Ready Reference - Thermal Properties of Metals. ASM International*. 2002.

[62] A. Hanneborg, M. Nese, and P. Ohlckers, *Silicon-to-silicon anodic bonding with a borosilicate glass layer*, *Journal of Micromechanics and Microengineering* **1** (sep, 1991) 139–144.

[63] M. Nese and A. Hanneborg, *Anodic bonding of silicon to silicon wafers coated with aluminium, silicon oxide, polysilicon or silicon nitride*, *Sensors and Actuators A: Physical* **37-38** (jun, 1993) 61–67.

[64] L. Buchwalter, *Chromium and tantalum adhesion to plasma-deposited silicon dioxide and silicon nitride*, *Journal of Adhesion Science and Technology* **9** (jan, 1995) 97–116.

[65] T. Akashi, *Fabrication of a Tantalum-Nitride Thin-Film Resistor with a Low-Variability Resistance*, *IEEJ Transactions on Sensors and Micromachines* **125** (2005), no. 4 182–187.

[66] T. Hashizume, A. Saiki, and K. Terayama, *Fabrication of Tantalum nitride thin film using the low vacuum magnetron sputtering system*, *IOP Conference Series: Materials Science and Engineering* **18** (oct, 2011) 092032.

[67] A. Kaushik, H. Kahn, and A. Heuer, *Wafer-level mechanical characterization of silicon nitride MEMS*, *Journal of Microelectromechanical Systems* **14** (apr, 2005) 359–367.